

Multiplicity Systems as Metrics for Stellar Evolution Theory: Spectroscopic Eclipsing, Eclipsing  
and Unresolved Binaries

By

Joni Marie Clark Cunningham

Dissertation

Submitted to the Faculty of the  
Graduate School of Vanderbilt University  
in partial fulfillment of the requirements

for the degree of

DOCTOR OF PHILOSOPHY

m

Astrophysics

May 13, 2022

Nashville, Tennessee

Approved:

David Weintraub, PhD

Kelly Holley-Bockelmann, PhD

Stephen Taylor, PhD

Joshua Pepper, PhD

Eric Agol, PhD

## DEDICATION

I dedicate my dissertation work first to my family, with special feelings of gratitude to my loving parents Sherrie Clark and Burl Clark (in memorandum). After my father passed away suddenly in a car accident, leaving my mother with four young children, she honored his memory and exemplified work ethic and dedication through raising us. While we may not have had affluence, we were always wealthy in love, encouragement, and support. Partially due in part to my own stubbornness, but entirely due to her constant belief in me (no matter where my efforts were being applied) I don't remember a time when I didn't believe I could do anything with enough hard work.

Second, I dedicate my dissertation work to my primary adviser and committee chair, David Weintraub who has provided me the utmost in guidance and fundamentally helped refine me into the researcher I am today. David always would advise me with directness, he pushed me when I needed it, and encouraged me when I needed it. David held me to high standards in my work, which in turn built my own confidence and immensely reduced my imposter syndrome. In expecting my best, having high standards, while also having a clear belief and confidence in my abilities, he allowed me to strive forward, onward and upward along with my personal pride, and scientific confidence. I did not truly know what to expect when I transitioned to his student, but he took me under his wing without question and never faltered in our shared mutual goal of refining my scientific prowess and capacity.

Finally, I dedicate my dissertation work to the Fisk-Vanderbilt Bridge Program. When I joined the Bridge, we discussed the word grit quite often. That more and more graduate programs are no longer using standardized tests in fields to determine student potential. That a student succeeding in graduate school is not as dependent on academic record, as it is their resilience. I am profoundly grateful to the Bridge program for leading the way in the application of these ideas, and empowering me to accomplish my dreams because of that same grit that my mom showed raising us. Never giving up, always getting up, and always showing up. Thank you to my wonderful mom, David, and to the bridge program, for that vindicating (and sometimes sustaining) recognition of the true power of hard work.



# TABLE OF CONTENTS

DEDICATION . . . . .	i
LIST OF FIGURES . . . . .	v
LIST OF TABLES . . . . .	xi
CHAPTER	
<b>1 Background . . . . .</b>	<b>2</b>
1.1 Introduction . . . . .	2
1.2 Stellar Formation and Evolution . . . . .	3
1.2.1 Pre-Main Sequence (PMS) . . . . .	4
1.2.2 Zero-Age Main Sequence (ZAMS) . . . . .	6
1.2.3 The Main Sequence (MS) . . . . .	6
1.2.4 Stellar Demise . . . . .	6
1.3 Multiple Star System Formation and Evolution . . . . .	7
1.3.1 Tertiary and Higher Order Systems . . . . .	9
1.4 Binary Systems: Spectroscopic & Eclipsing . . . . .	10
1.4.1 Radial Velocity Extraction from <i>APOGEE</i> Spectroscopy . . . . .	11
1.5 Stellar Chronometers . . . . .	13
1.5.1 Lithium Emission . . . . .	13
1.5.2 Ca IIR&K Absorption . . . . .	14
1.6 Age Estimates . . . . .	14
1.6.1 The Coevality Hypothesis . . . . .	14
1.6.2 Isochrones . . . . .	15
1.6.3 Galactic Motion . . . . .	15
1.6.4 Stellar Associations . . . . .	16
<b>2 Method . . . . .</b>	<b>18</b>
2.1 Photometric Observations and Analysis . . . . .	18
2.1.1 Kepler Photometry . . . . .	18
2.1.2 The Kilodegree Extremely Little Telescope South ( <i>KELT</i> South ) . . . . .	19
2.1.3 The Perth Exoplanet Survey Telescope ( <i>PEST</i> ) . . . . .	19
2.1.4 The Transiting Exoplanet Survey Satellite ( <i>TESS</i> Photometry . . . . .	20
2.2 Spectroscopic Observations and Analysis . . . . .	22
2.3 <i>APOGEE</i> Spectroscopy . . . . .	23

2.3.1	Radial Velocity Extraction: The Broadening Function and Cross Correlation Function . . . . .	25
2.4	ANU 2.3-m Spectroscopy: The Wide Field Spectrograph (WiFeS) . . . . .	26
2.5	SOuthern Astrophysical Research Telescope (SOAR): Goodman High Throughput Spectrograph . . . . .	27
<b>3</b>	<b><i>APOGEE/Kepler</i> Overlap Yields Orbital Solutions for a Variety of Eclipsing Binaries . . . . .</b>	<b>28</b>
3.1	Introduction . . . . .	29
3.2	Data and Methods . . . . .	30
3.2.1	Sample Selection . . . . .	30
3.2.2	RVs from <i>APOGEE</i> Spectra . . . . .	32
3.2.3	<i>Kepler</i> Light Curve Processing . . . . .	33
3.2.4	Orbital and Mass Solutions with <i>KEBLAT</i> . . . . .	33
3.2.5	Radius ratio - flux ratio - inclination Degeneracy . . . . .	36
3.2.6	Temperatures from Flux Ratios and Radii . . . . .	36
3.3	Results . . . . .	37
3.3.1	KIC 5285607 . . . . .	39
3.3.2	KIC 6864859 . . . . .	39
3.3.3	KIC 6778289 . . . . .	39
3.3.4	KIC 6449358 . . . . .	40
3.3.5	KIC 4285087 . . . . .	42
3.3.6	KIC 6131659 . . . . .	43
3.3.7	KIC 6781535 . . . . .	44
3.3.8	Supplemental Physical Parameters . . . . .	45
3.4	Discussion . . . . .	50
3.4.1	Evolutionary Histories . . . . .	50
3.4.2	Mass-Luminosity Relationships . . . . .	50
3.4.3	Tertiary Companions . . . . .	51
3.5	Summary . . . . .	53
3.6	Acknowledgements . . . . .	55
3.7	Clark-Cunningham et al. 2019 Appendix . . . . .	55
3.7.1	TIC 021980925 . . . . .	55
3.7.2	TIC 283889669 . . . . .	55
<b>4</b>	<b>A <i>KELT/TESS</i> Eclipsing Binary in a Young Triple System Associated with the Local "Stellar String" Theia 301 . . . . .</b>	<b>63</b>
4.1	Introduction . . . . .	63
4.1.1	The HD 54236 System . . . . .	65
4.2	Data . . . . .	66
4.2.1	Photometric Observations . . . . .	66
4.2.2	Spectroscopic Observations . . . . .	72
4.2.3	ANU 2.3m Spectroscopy . . . . .	72
4.2.4	High-resolution Spectroscopy: Radial Velocities . . . . .	73
4.3	Results . . . . .	76

4.3.1	System Ephemeris . . . . .	77
4.3.2	Orbit Solution . . . . .	77
4.3.3	PHOEBE Light Curve Model . . . . .	78
4.3.4	SED Analysis . . . . .	79
4.3.5	System Age . . . . .	81
4.4	Discussion: Membership, Stellar Strings, and AB Dor . . . . .	88
4.5	Summary and Conclusions . . . . .	90
<b>5</b>	<b>Evaluation of APOGEE-identified Spectroscopic Binaries Using TESS Photometry . . . . .</b>	<b>93</b>
5.1	Introduction . . . . .	94
5.2	Data and Methods . . . . .	95
5.3	Sample Selection . . . . .	96
5.4	TESS Photometry . . . . .	97
5.5	<i>APOGEE</i> Spectroscopy . . . . .	98
5.5.1	Radial Velocities from <i>APOGEE</i> Spectroscopy . . . . .	100
5.6	Results . . . . .	101
5.6.1	TIC 053478754 . . . . .	102
5.6.2	TIC 171517465 . . . . .	103
5.6.3	TIC 099763308 . . . . .	104
5.6.4	TIC 416593638 . . . . .	105
5.6.5	TIC 284597233 . . . . .	106
<b>6</b>	<b>Discussion . . . . .</b>	<b>110</b>
	<b>BIBLIOGRAPHY . . . . .</b>	<b>115</b>

## LIST OF FIGURES

### FIGURE

2.1	Histogram modeling the distribution of $n_{ApVisit}$ observations for the <i>APOGEE Gold sample</i> ( <i>AuPOGEE</i> ). The majority of <i>AuPOGEE</i> binaries have under ten $n_{ApVisit}$ spectra: in both cases of criteria (in the <i>APOGEE/Kepler</i> overlap and the <i>Au-POGEE/TESS</i> overlap) $n_{ApVisits}$ was the most often disqualifying factor. . . . .	24
3.1	The BF (orange) is significantly better at resolving multiple velocity components from <i>APOGEE</i> visit spectra than the CCF (blue). This example shows visits for KIC 6864859. The y-axis amplitude is arbitrarily scaled for clarity. While it is clear from most of the CCFs that KIC 6864859 is a double-lined SEB, the BF more clearly separates the contribution from each star. . . . .	34
3.2	A second example, as in Figure 3.1, showing that the BF (orange) does a better job of resolving multiple velocity components than the CCF (blue). The y-axis amplitude is arbitrarily scaled for clarity. While it is clear from some of the CCFs that KIC 6131659 has more than one component, the three-component nature is immediately obvious in the BF. . . . .	35
3.3	Simultaneous light curve (top panels) and RV (bottom panel) fits to <i>Kepler</i> and <i>APOGEE</i> observations for KIC 5285607. The light curve data and residuals are shown in dark gray, with the model overlaid in blue. Note the shallow and V-shaped primary and secondary eclipses, which indicate a grazing system. The phased RV panel shows the BF-derived values (points) and corresponding model (lines), where the primary RV is red and secondary RV is orange. The RV semi-amplitude is $\sim 100 km s^{-1}$ while the residual scatter is $\sim 1 km s^{-1}$ . . . . .	40
3.4	Simultaneous light curve (top panels) and RV (bottom panel) fits to <i>Kepler</i> and <i>APOGEE</i> observations of KIC 6864859. The primary and secondary eclipses are similar in shape and depth with $\sim 25\%$ loss of light; the phase of the secondary eclipse and shapes of the RVs indicate an extremely eccentric system. The light curve residuals are small but have a coherent shape, likely due to tidal and rotational distortion of the stars. . . . .	41
3.5	Heartbeat signatures of the eccentric eclipsing system KIC 6864659. The light curve surrounding the primary and secondary eclipses is folded in phase and offset vertically between each observed orbit, using different colors for visual clarity. The brightening between the primary and secondary eclipse is readily apparent around phase 0.065. . . . .	42

3.6	Simultaneous light curve (top panels) and RV (bottom panel) fits to <i>Kepler</i> and <i>APOGEE</i> data for KIC 6778289. Different eclipse depths along with a flat-bottomed secondary eclipse indicate a smaller and dimmer secondary. Additionally, the unequal amplitudes and shape of the RV indicates an unequal mass binary with significant orbital eccentricity. . . . .	43
3.7	Simultaneous RV+LC fit for KIC 6449358, a single-lined spectroscopic binary suspected in a hierarchical triple system. We utilize mass function here rather than individual component masses to obtain the RV fit.) . . . . .	44
3.8	<i>O - C</i> diagram for KIC 6449358, showing primary eclipse timing variations; the ETVs exhibit a half-sinusoid trend, giving a rough estimate for the minimum period of the tertiary perturber to be $P \sim 1450$ days. . . . .	45
3.9	Simultaneous light curve (top panels) and RV (bottom panel) fits to the <i>Kepler</i> and <i>APOGEE</i> observations. The phase of secondary eclipse and shape of RVs indicate EBs in a $\sim$ circular orbit. The light curve residuals during eclipse suggest the presence of a variable third light contribution, or non-Keplerian photometric effects given its short period. ( $\sim 4$ days). . . . .	46
3.10	Simultaneous light curve (top panels) and RV (bottom panel) fits to the <i>Kepler</i> and <i>APOGEE</i> observations for KIC 6131659. The primary and secondary eclipses are relatively deep, with 35% and 10% losses of total system light, respectively. . . . .	47
3.11	Top panels show the light curve model (blue) for KIC 6781535 overlaid against data (gray) as a function of phase. Bottom panel shows the RV model (lines) for primary (red) and secondary (orange) components overlaid on top of the <i>APOGEE</i> -extracted data (points). The models correspond to the best-fit joint LC+RV solution. . . . .	48
3.12	Spectroscopic <i>H-R</i> diagram for the systems with <i>Gaia</i> distances. Primaries are depicted with the solid circles while secondaries are open circles. A variety of Dartmouth isochrones are plotted with a range of ages 0.8–3 Gyr and metallicities (sub-solar to solar). . . . .	51
3.13	Same as Figure 3.12, showing each SEB system individually. The filled circles model the primary star of the SEB, and the hollow circles the secondaries. . . . .	52
3.14	Radius versus mass diagram for all seven systems. Primaries are shown as solid circles and secondaries as open circles. Dartmouth isochrones for a variety of ages and metallicities are also plotted. All seven systems are consistent with coevality, ranging in age from about 1 to about 3 Gyr, assuming a normal Milky Way metallicity of $[M/H] = -0.5$ . . . . .	53
3.15	Mass-luminosity relationship for the four targets with accurate <i>Gaia</i> distances and RV-derived masses. The primaries are shown in solid circles and secondaries in open circles. Dartmouth isochrones (Dotter et al., 2008) are overplotted as gray lines, corresponding to a variety of ages and metallicities. . . . .	54
3.16	TIC 099763308 Spectroscopic and Photometric analysis: <b>Top-Left:</b> Unfolded <i>TESS-SPOC</i> LC. <b>Top-Right:</b> Unfolded <i>APOGEE</i> RV curve. <b>Middle-Left:</b> <i>TESS-SPOC</i> LC folded onto the <i>APOGEE Gold Sample</i> period solution. <b>Middle-Right:</b> <i>APOGEE</i> RV curve folded onto the <i>APOGEE Gold Sample</i> period solution. <b>Bottom-Left:</b> <i>TESS-SPOC</i> LC folded onto our <i>TESS</i> BLS periodicity estimate. <b>Bottom-Right:</b> <i>APOGEE</i> RV curve folded onto our <i>TESS</i> BLS periodicity estimate. . . . .	56

3.17	TIC 416593638 Spectroscopic and Photometric analysis: <b>Top-Left:</b> Unfolded <i>TESS-SPOC</i> LC. <b>Top-Right:</b> Unfolded <i>APOGEE</i> RV curve. <b>Middle-Left:</b> <i>TESS-SPOC</i> LC folded onto the <i>APOGEE Gold Sample</i> period solution. <b>Middle-Right:</b> <i>APOGEE</i> RV curve folded onto the <i>APOGEE Gold Sample</i> period solution. <b>Bottom-Left:</b> <i>TESS-SPOC</i> LC folded onto our <i>TESS</i> BLS periodicity estimate. <b>Bottom-Right:</b> <i>APOGEE</i> RV curve folded onto our <i>TESS</i> BLS periodicity estimate. . . . .	57
3.18	TIC 416593638 Primary and Secondary eclipsing events. These eclipsing events are derived through folding the <i>TESS-SPOC</i> photometry onto the results of its BLS periodicity analysis. . . . .	58
3.19	TIC 284597233 Primary and Secondary eclipsing events. These eclipsing events are derived through folding the <i>TESS-SPOC</i> photometry onto the results of its BLS periodicity analysis and subsequent iterative fit of diminishing step sizes. This target inherited noise in it's photometry even after normalization and smoothing were completed by the <i>Astropy</i> and <i>wotan</i> packages. . . . .	59
3.20	TIC 021980925 Spectroscopic and Photometric analysis: <b>Top-Left:</b> Unfolded <i>TESS-SPOC</i> LC. <b>Top-Right:</b> Unfolded <i>APOGEE</i> RV curve. <b>Middle-Left:</b> <i>TESS-SPOC</i> LC folded onto the <i>APOGEE Gold Sample</i> period solution. <b>Middle-Right:</b> <i>APOGEE</i> RV curve folded onto the <i>APOGEE Gold Sample</i> period solution. <b>Bottom-Left:</b> <i>TESS-SPOC</i> LC folded onto our <i>TESS</i> BLS periodicity estimate. <b>Bottom-Right:</b> <i>APOGEE</i> RV curve folded onto our <i>TESS</i> BLS periodicity estimate. . . . .	60
3.21	TIC 283889669 Spectroscopic and Photometric analysis: <b>Top-Left:</b> Unfolded <i>TESS-SPOC</i> LC. <b>Top-Right:</b> Unfolded <i>APOGEE</i> RV curve. <b>Middle-Left:</b> <i>TESS-SPOC</i> LC folded onto the <i>APOGEE Gold Sample</i> period solution. <b>Middle-Right:</b> <i>APOGEE</i> RV curve folded onto the <i>APOGEE Gold Sample</i> period solution. <b>Bottom-Left:</b> <i>TESS-SPOC</i> LC folded onto our <i>TESS</i> BLS periodicity estimate. <b>Bottom-Right:</b> <i>APOGEE</i> RV curve folded onto our <i>TESS</i> BLS periodicity estimate. . . . .	61
3.22	TIC 283889667 Primary and Secondary eclipsing events. These eclipsing events are derived through folding the <i>TESS-SPOC</i> photometry onto the results of its BLS periodicity analysis. From the shape of the eclipsing events in this system it is likely that this system is a total eclipsing binary, close to being directly in our line of sight. . . .	62
4.1	DSS image of the HD 54236 tertiary system and its common-proper-motion is highlighted in fuchsia. The tertiary system includes HD 54236A (the eclipsing binary), and HD 54236B, the CPM tertiary member $\sim 6.5''$ south of HD 54236A. Surrounding, unrelated stars (like TIC 767642478, the distant faint star to the north) are shown in green. HD 54262, an unrelated high proper motion star to the east is highlighted in yellow. . . . .	66
4.2	Phase-folded lightcurve of HD 54236A from KELT. Small symbols represent individual measurements, red lines represent the binned light curve. . . . .	67
4.3	Phase-folded lightcurve of HD 54236A from KELT ( <i>black points</i> ) with the follow-up data from PEST over-plotted ( <i>red points</i> ). Since the KELT data includes the flux from the unrelated high proper motion star HD 54262, the KELT data are multiplied by a factor of 3 to match the egress slope from the PEST data. . . . .	69

4.4	<i>TESS</i> Target Pixel File cutouts of HD 54236 for Sectors 6, 7, and 8. The red aperture mask is the optimal aperture from the SPOC pipeline, chosen to avoid the distant faint star to the north, TIC 767642477, from blending the photometry. . . . .	69
4.5	<i>TESS</i> Photometry <b>Left:</b> <i>TESS</i> light curve of HD 54236 in Sectors 6, 7, and 8. <b>Right:</b> Phase-folded <i>TESS</i> light curve. . . . .	70
4.6	BLS periodogram, showing the most prominent periodic features, corresponding to the eclipse period but also showing a similar but different period of 2.3782 d which we attribute to the stellar rotation period (see the text). . . . .	70
4.7	The first 10 days of the <i>TESS</i> light curve spanning Sectors 6 to 8, shown in <i>TESS</i> Julian Days (TJD). The black points are the <i>TESS</i> data and the red line is the Biweighted Midcorrelation filter applied to the flux baseline. We used a window size of 6 hours which equals to 3 times the transit duration reported by BLS. . . . .	71
4.8	The phase folded <i>TESS</i> light curve that was smoothed using a Biweighted Midcorrelation filter as described in §4.2.1.3. The out-of-transit variations seen in Figure 4.6 are removed in these data. . . . .	71
4.9	<b>Top:</b> Spectral analysis of the stellar parameters of HD 54236A, the eclipsing binary. <b>Bottom:</b> Spectral analysis of the stellar parameters of the tertiary member, HD 54236B. The observed spectra for both HD 54236A and HD 54236B are shown in blue, while their respective templates modeled in green. Discrepancies between the target spectra and its template are largely due to differences in flux calibration, however, spectral matching is done based on spectral features rather than overall shape. . . . .	73
4.10	Cross-correlation function for the spectrum taken on HJD 2456057.93945226, with the ANU 2.3 m echelle at $R = 23000$ . The CCF shown is the average CCF of the cross correlations from all echelle orders, excluding those with very low cross-correlation heights. The cross-correlations are performed against RV standard star exposures taken on the same night. For clarity, the highest peak (presumed to correspond to higher mass, primary component in the eclipsing binary, has been shifted in this figure to be at $0 \text{ km s}^{-1}$ . . . . .	74
4.11	Region of the Li line from the SOAR spectrum of HD54236, taken June 7, 2012. . . .	76
4.12	RV solution for HD 54236A: The primary is modeled with the solid line, and the secondary with the dashed line. . . . .	77
4.13	Corner plot of fitted parameters for cleaned sample of 2500 model light curves. Values atop distribution are the median values and the 0.16 & 0.84 quantiles. . . . .	79
4.14	Light curve fitting for HD 54236A using GA converged model solution. There remain some small systematics in the residuals in eclipse, the amplitude of which are of order 1% of the eclipse depths. The final stellar parameters from this solution are listed in Table 4.1. . . . .	80
4.15	<i>Top:</i> SED fit of HD 54236A <i>Bottom:</i> HD 54236B SED fit. Red symbols are observed broadband fluxes, curves are the best-fit model atmospheres, and blue symbols are the model fluxes for comparison to the observed fluxes. . . . .	81

4.16	<i>Top:</i> $T_{\text{eff}}$ -Radius diagram for the primary star of the HD 54236A system. <i>Middle:</i> $T_{\text{eff}}$ -Radius diagram for the secondary star of the HD 54236A system. Both are in the $T_{\text{eff}}$ vs Radius plane and show the Yonsei-Yale stellar evolutionary tracks (Yi et al., 2001), which suggest an age for HD 54236A near the ZAMS (which occurs at an age of 300 Myr in these models) and roughly consistent with an age of $225 \pm 50$ Myr as determined from other age diagnostics. . . . .	82
4.17	H-R diagram showing all three components of the HD 54236 system (black symbols) compared to the PMS evolutionary models of Baraffe et al. (1998); shown are isochrones at ages of 1, 3, 10, 30, 100, and 300 Myr (red dashed lines) and tracks for masses of $0.6\text{--}1.2 M_{\odot}$ in increments of $0.1 M_{\odot}$ (blue curves) . . . . .	83
4.18	Lithium abundance analysis for a range of ages of clusters: Comparison of EW of lithium abundances from the HD 54236 system to several different clusters ranging in age from 35 Myr to 1.2 Gyr (sample clusters and their parameters are from Sestito & Randich, 2005). From these comparisons we can see that the stellar components in the HD 54236 system (shown with red and blue squares for the primary and secondary stars in the eclipsing binary primary HD 54236A) are indicative of a relatively young age: between PMS clusters and older main sequence clusters. . . . .	85
4.19	Ca I/H&K analysis of the WiFeS spectrum for HD 54236B against stars with similar $T_{\text{eff}}$ from three different open clusters spanning the range of ages estimated from the Li abundances in §4.3.5.1. Against the Ca I/H&K analysis for HD 54236B (black line). <i>Top:</i> comparison with IC 2391 (age $\sim 50$ Myr). <i>Middle:</i> comparison with Pleiades (age $\sim 130$ Myr with a range of $T_{\text{eff}}$ from 4200 K - 5420 K). <i>Bottom:</i> Comparison with M7 (age $\sim 300$ Myr). The open cluster spectra were taken from Keck HIRES and VLT UVES public archives and convolved to match the resolution of the WiFeS observation of HD 54236B. Taken together, these comparisons strongly imply an age of HD 54236B older than the Pleiades ( $\sim 130$ Myr) and clearly younger than M7 ( $\sim 300$ Myr). . . . .	87
4.20	Phase space of HD 54236A relative to the phase space of Theia 301. . . . .	89
5.1	TIC 053478754 Spectroscopic and Photometric analysis: <b>Top-Left:</b> Unfolded <i>TESS-SPOC</i> LC. <b>Top-Right:</b> Unfolded <i>APOGEE</i> RV curve. <b>Middle-Left:</b> <i>TESS-SPOC</i> LC folded onto the <i>APOGEE Gold Sample</i> period solution. <b>Middle-Right:</b> <i>APOGEE</i> RV curve folded onto the <i>APOGEE Gold Sample</i> period solution. <b>Bottom-Left:</b> <i>TESS-SPOC</i> LC folded onto our <i>TESS</i> BLS periodicity estimate. <b>Bottom-Right:</b> <i>APOGEE</i> RV curve folded onto our <i>TESS</i> BLS periodicity estimate. . . . .	102
5.2	TIC 053478754 Primary and Secondary eclipsing events. These eclipsing events are derived through folding the <i>TESS-SPOC</i> photometry onto the results of its BLS periodicity analysis. From the depths of the eclipses, we know that the system has a mass ratio around $q \sim 0.85$ . Unfortunately in this target, the entirety of the secondary eclipsing event was not captured by the <i>TESS</i> observations, however, assuming a symmetric eclipse, we are still able to solve for stellar parameters from these eclipses. . . . .	103
5.3	Broadening function extraction of radial velocities for TIC 053478754. The primary stellar component is modeled in yellow, and the secondary in red. The extraction of the Radial Velocities occurs at the peak amplitude's radial velocity component. Orbital phase and the dates of the observations are provided on each subplot. . . . .	104



5.4 TIC 171517465 Spectroscopic and Photometric analysis: **Top-Left:** Unfolded *TESS-SPOC* LC. **Top-Right:** Unfolded *APOGEE* RV curve. **Middle-Left:** *TESS-SPOC* LC folded onto the *APOGEE Gold Sample* period solution. **Middle-Right:** *APOGEE* RV curve folded onto the *APOGEE Gold Sample* period solution. **Bottom-Left:** *TESS-SPOC* LC folded onto our *TESS* BLS periodicity estimate. **Bottom-Right:** *APOGEE* RV curve folded onto our *TESS* BLS periodicity estimate. . . . . 105

5.5 TIC 171517465 Primary and Secondary eclipsing events. These eclipsing events are derived through folding the *TESS-SPOC* photometry onto the results of its BLS periodicity analysis. From the depths of the eclipses, we know that the system has a mass ratio around  $q \sim 0.85$ . Unfortunately in this target, the entirety of the secondary eclipsing event was not captured by the *TESS* observations, however, assuming a symmetric eclipse, we are still able to solve for stellar parameters from these eclipses. . . . . 106

5.6 Broadening function extraction of radial velocities for TIC 171517465. The primary stellar component is modeled in yellow, and the secondary in red. The extraction of the Radial Velocities occurs at the peak amplitude's radial velocity component. Orbital phase and the dates of the observations are provided on each subplot. . . . . 107

5.7 TIC 099763308 Primary and Secondary eclipsing events. These eclipsing events are derived through folding the *TESS-SPOC* photometry onto the results of its BLS periodicity analysis. From the depths of the eclipses, we know that the system has a mass ratio around  $q \sim 0.85$ . Unfortunately in this target, the entirety of the secondary eclipsing event was not captured by the *TESS* observations, however, assuming a symmetric eclipse, we are still able to solve for stellar parameters from these eclipses. . . . . 107

5.8 TIC 180627564 Spectroscopic and Photometric analysis: **Top-Left:** Unfolded *TESS-SPOC* LC. **Top-Right:** Unfolded *APOGEE* RV curve. **Middle-Left:** *TESS-SPOC* LC folded onto the *APOGEE Gold Sample* period solution. **Middle-Right:** *APOGEE* RV curve folded onto the *APOGEE Gold Sample* period solution. **Bottom-Left:** *TESS-SPOC* LC folded onto our *TESS* BLS periodicity estimate. **Bottom-Right:** *APOGEE* RV curve folded onto our *TESS* BLS periodicity estimate. . . . . 108

5.9 TIC 284597233 Spectroscopic and Photometric analysis: **Top-Left:** Unfolded *TESS-SPOC* LC. **Top-Right:** Unfolded *APOGEE* RV curve. **Middle-Left:** *TESS-SPOC* LC folded onto the *APOGEE Gold Sample* period solution. **Middle-Right:** *APOGEE* RV curve folded onto the *APOGEE Gold Sample* period solution. **Bottom-Left:** *TESS-SPOC* LC folded onto our *TESS* BLS periodicity estimate. **Bottom-Right:** *APOGEE* RV curve folded onto our *TESS* BLS periodicity estimate. . . . . 109

## LIST OF TABLES

### TABLE


3.1	Promising SEBs Observed by <i>APOGEE</i> and <i>Kepler</i> , Sorted by <i>Kepler</i> Magnitude ( $K_p$ ).	31
3.2	Binary Orbital and Stellar Parameters . . . . .	38
3.3	Parameters Related to RV Extraction and Temperature Estimates . . . . .	49
4.1	RV Observations of HD 54236 A . . . . .	75
4.2	Orbital Solution of HD 54236 A . . . . .	77
4.3	PHOEBE Fit Parameters and Solutions of HD 54236A . . . . .	80
4.4	Galactic Motions of HD 54236A . . . . .	88
4.5	HD 54236 System Solutions . . . . .	91

Multiplicity Systems as Metrics for Stellar Evolution Theory: Spectroscopic Eclipsing, Eclipsing and Unresolved Binaries

Joni Marie Clark Cunningham

Dissertation under the direction of Professor David Weintraub

Binary stars serve as the astrophysical laboratory in the extraction of stellar and orbital parameters and as calibration sites for stellar evolution theory. These systems come in three flavors, spectroscopic eclipsing, eclipsing and unresolved. In this dissertation, I combined photometric and spectroscopic observations of binary targets within the observational overlaps to determine stellar and orbital properties, spanning a wide range of mass, temperature and radius ratios. These solutions are then utilized to arrive at age estimates and test stellar evolution theory. The *APOGEE* field includes 19,635 binary candidates with multiple high resolution spectroscopic observations. Spectroscopic eclipsing binaries with complete orbital and stellar solutions from *APOGEE/Kepler* overlap (J.M.C. Cunningham et al. 2019) and *TESS* (J.M.C. Cunningham et al. in prep, 2022) are presented. Depending on the binary system, different methodologies are equipped, including both the cross correlation (CCF) and broadening function (BF) methods of Radial Velocity extraction. In the *TESS/APOGEE* overlap targets, I used the BF method of radial velocity extraction to disentangle radial velocity elements for two systems. While in the *Kepler/APOGEE* overlap, I used the BF to extract primary and secondary solutions for a total of seven spectroscopic eclipsing binaries. With these solutions I compute age estimates for each subset, which I use to determine the degree of coevality for each system (that is, the assumption that binary stars form at the same time). A unique, young eclipsing binary with a tertiary component is presented (J.M.C. Cunningham et al. 2020). Photometric observations from *TESS* and *KELT*, and spectroscopic observations from a number of missions were used to solve for stellar and orbital solutions. These solutions and stellar chronometers were then used to determine a most likely age for the system. Gaia proper motion and age estimates established it having likely membership in a newly discovered stellar stream association, Theia-301. Additionally, when I apply the age I derived for this system to AB Dor (by virtue of six shared members between the two associations) the luminosity discrepancy for the star AB Dor disappears. Binary (and higher order multiplicity) systems have such far reaching effects on stellar formation in terms of intermolecular cloud fragmentation and the initial mass function, that incomplete binary fraction estimates prevent true modeling of these foundational processes. Every identification of a multiplicity system, with stellar and orbital solutions, age estimates and galactic motion vectors results in a more complete understanding of stellar evolution and a more complete binary fraction.

Approved  \_\_\_\_\_

David Weintraub, Ph.D

March 14, 2022  
Date \_\_\_\_\_

# CHAPTER 1

## Background

### 1.1 Introduction

The existence of binary star systems was recognized during the advent of modern astronomy in the 17th century, but the astrophysical novelty and utility of these systems became evident only less than a century ago. Kuiper (1935) was the first to argue the empirical determination of the binary fraction, and these system's orbital parameters would be invaluable to Astrophysical theory. Such a significant fraction of stars reside in multiplicity systems that they are considered ubiquitous with stellar formation (Duchêne & Kraus, 2013), however, the effects of stellar multiplicity on a system's formation, and dynamical evolution are not completely understood.

Since the 17th century, ample progress has been made to comprehend the effects of multiplicity on stellar formation and evolution (discussed in §1.2). The utility of fundamental stellar parameters in Astrophysics is the constraint of theoretical stellar evolutionary models, which infer the determinations of stellar mass systems, and exoplanet properties. Eclipsing binaries (EBs) are key fundamental laboratories for determining these stellar and orbital parameters (Stassun, 2011).

First postulated by Kuiper (1935), we now know that stellar multiplicity, and the binary fraction effect fundamental concepts in astrophysics, including the initial mass function (IMF). The IMF can be defined formally as the complete ensemble of stars with their initial masses that form together. The IMF is not normally corrected for the effect that many, if not most stars reside in (unresolved) binary systems (Malkov & Zinnecker, 2001). Further, Kroupa & Jerabkova (2018) found that the effect on the IMF is not uniform across stellar masses; at the high mass end of binary mass ratios, the shape of the IMF is not much effected by unresolved binary companions. The high multiplicity found amongst higher mass stars may lead to a substantial fraction of companions being ejected from their birth clusters and the merging of high mass stars (Kroupa & Jerabkova, 2018).

This chapter is structured as followed, immediately in §1.2, I outline stellar formation and evolution is outlined, and discuss the suspected effects of stellar multiplicity. In §1.4 I discuss Eclipsing Binary (EBs) and Spectroscopic Eclipsing Binaries (SEBs) along with stellar chronome-

ters, age estimates, coevality tests and isochrones. §1.6.3 cover galactic motions, and how these motions, when combined with age estimates, stellar parameters can be used to determine stellar heritage and stellar association membership. Chapter 2 of this dissertation covers the methodology of the analysis in three projects: Clark Cunningham et al. (2019) (§3), (Clark Cunningham et al., 2020) (§4), (Clark Cunningham et al., 2022) (§5). Chapter 6 offers a discussion on the general theme of the projects described herein.

## 1.2 Stellar Formation and Evolution

Most star formation in galaxies occurs in the spiral arms of and can be identified by concentrations of luminous young stars surrounded by ethereal clouds of gas and dust. Stars can also form toward galactic centers, like in our Milky Way, but these processes are often obscured by interstellar dust and their presence can only be inferred through infrared radiation emitted by the dust. Surveys of the molecular clouds in galaxies indicate that they reside in structures that span sizes up to a kiloparsec and contain up to  $10^7 M_{\odot}$  of stellar material (Larson, 2003).

Stars form in molecular clouds whose density has become large enough to prevent infrared radiation from escaping (Larson, 1969) and begin to collapse. Provided the cloud allows for the escape of infrared-radiation and does not expand to accommodate that increase in energy. The initial over-density of a molecular cloud begins the gravitational collapse and as material falls inward, the density of the cloud increases, while density at its boundaries decreases. This causes a pressure gradient to form in the outer regions of the cloud, which slows the speed of the collapse in the molecular cloud's periphery. The density distribution of the cloud becomes peaks at the center, where the collapse proceeds approximately at free fall velocities (Larson, 1969). The intermolecular cloud at this point becomes opaque at UV and visible wavelength regimes, but infra-red radiation escapes and allows for their detection. This causes the collapse to be non-homologous in nature and can lead to fragmentation, as the densest regions or centers of condensation may separate out and collapse on their own (Larson, 1973). Provided these regions have the mass, density and temperature to satisfy the Jeans criterion and ensure dispersive force of internal pressure is not stronger than gravitational contraction (Jeans, 1929) a collapse of the molecular cloud is imminent.

The idea that fragmentation can occur in collapsing interstellar clouds was first proposed by Larson (1973), and this process is now generally agreed to be the mechanism that forms binary and higher order multiplicity systems. Larson (2003) remarked that the interactions among stars in a forming multiple system or cluster may themselves play an important role in the stellar formation process. The gravitational interactions between stellar components in the binary (or higher order multiplicity) systems may trigger the redistribution of angular momentum that is necessary for stars to form (Larson, 1973).

Currently, stellar multiplicity systems are widely agreed to result from the collapse and fragmentation of molecular cloud cores, despite what interference occurs from the influence of magnetic fields (Reipurth et al., 2014). Simultaneously, other groups had studied high resolution core scale simulation of HD collapse at much lower masses (Federrath et al., 2011). These lower masses were essentially at the Bonnor-Ebert limit, which is the largest mass an isothermal gas in a pressurized medium can have before collapsing. In essence the Bonner-Ebert limit describes the largest mass an isothermal cloud can have whilst maintaining hydrostatic equilibrium. Studies of these Bonner-Ebert clouds allow for the delineation of factors such as initial rotation rate, metallicity, turbulence, and density effects if a cloud forms a singular, binary, or higher order multiplicity system. Studies of multiplicity systems in the pre-main sequence (PMS) are critical to insight into fragmentation, as it is during this early time in a systems life that fragmentation occurs (see §1.2.1). Studies of the zero age main sequence (ZAMS), main sequence (MS) and stellar demise stages of stellar evolution are also important in refining our understanding of stellar evolution. The suspected effects of multiplicity as well as its affects on star formation and evolution are described in §1.3.

### **1.2.1 Pre-Main Sequence (PMS)**

Accurate measurements of the basic physical properties of Pre-Main-Sequence (PMS) stars, (like masses, radii, temperatures, and metallicities) are essential to our understanding of the physics of star formation (Reipurth et al., 2014). Due to their long lifetimes, the evolution of low mass pre-main sequence stars dominate the Galactic stellar population, yet the evolutionary tracks of low mass stars remain largely uncalibrated by empirical mass determinations Cargile et al. (2006).

PMS stars however, are still deeply embedded in their thick envelopes and suffer from extinctions, making their detection especially difficult and observations being limited to the infrared, sub-millimeter, or radio continuum. PMS stars can be differentiated observationally through the determination of their surface gravity as a PMS object will have a larger radius than a MS object of the same mass, and thus have a lower surface gravity. The surface gravity of a star can be measured through photometric, spectroscopic or asteroseismic analysis. In this dissertation, the spectroscopy is utilized, as it normally produces more precise estimates. In this method, narrow bands in the spectra are examined for broadening, which indicates a lower surface gravity. Stars with high surface gravity have less broadening found in these spectral lines.

The energy source of PMS stars comes from gravitational contraction, which lasts only  $\approx 1\%$  of the time it spends on the MS. Recent theoretical work has shown that the PMS stage in stellar evolution is more complex than once thought. Traditionally (e.g., Hayashi (1961); Mengel et al. (1979)), PMS stars were generally believed to form steadily with a large radius that contracts

isotropically: this gravitational potential energy heats the interior until thermonuclear reactions can begin, which acts opposite of the force of contraction and finally, the star's radiative zone begins to form. The formation of the radiative zone is the longest portion of the PMS phase; in this time a star can be fully convective, or have a very deep convection zone before the radiative zone forms. Fast mixing in these deep convection zones would likely lead to a homogeneous composition in the stellar interior (Stahler et al., 1980). This would have strong consequences for stellar evolutionary tracks, the related inferred properties of the star system, and would control the level to which planet formation affect stellar surface composition both observationally (Ramírez et al., 2009, 2011) and theoretically (Chambers, 2010; Guillot et al., 2014).

A number of studies have shown that the above descriptor represents only an ideal picture of the PMS phase in stellar evolution; the PMS can be strongly affected by the way material is accreted onto the star during the accretion phase (Kunitomo et al., 2017). In this accretion phase of material in the disk onto the protostar, entropy in the form of temperature differentials is radiated into space due to optical thickness being much thicker towards the stellar interior is much greater than that of the disk. If accreting material loses entropy before or during accretion onto the star, the star can grow from a smaller radius and avoid the large quasi-static contraction phase (e.g., Mercer-Smith et al. (1984); Palla & Stahler (1992); Hartmann et al. (1997); Dunham & Vorobyov (2012). The quasi-static contraction phase begins as accretion is progressively suppressed by the star tending to hydrostatic equilibrium. This is due to the outward growing outward pressure (from the growing energy within the stellar interior) and the inward force of gravity. During the quasi-static contraction phase (which effectively leads to the formation of the stellar radiative zone) the progression of the evolution is very slow compared to the rapid dynamical evolution that occurred just previously in the PMS phase.

The accretion onto the PMS star is primarily determined by the angular momentum of the collapsing gas and formation of the circumstellar disk and can be highly variable as seen in FU Ori stars. The effects of accretion on stellar structure were studied in detail by Siess et al. (1997). The accretion of material results in an increase of stellar mass and modifies the stellar environment, delivers energy and fresh deuterium to the protostar, and alters its radiation. Completely modeling the accretion complexity should also consider the angular momentum in the molecular cloud along with its core, magnetic field and geometry (Kunitomo et al., 2017).

The scarcity of PMS stars concurrent with their determinant relationship to stellar evolution makes empirical tests of PMS stellar evolution paramount. Eclipsing binary systems (EBs) allow for the empirical measurement of the stellar component properties to a high degree of certainty (Stassun et al., 2014). Another element of complexity arises in multiplicity systems, however. Using a benchmark sample of 13 PMS EBs ranging in mass from 0.4 - 4.0  $M_{\odot}$  and nominal ages spanning  $\sim 1 - 20$  Myr Stassun et al. (2019) found that PMS stars can be influenced by their

companions. Effects of binarity and higher order multiplicity are discussed further in §1.4.

### **1.2.2 Zero-Age Main Sequence (ZAMS)**

Once a PMS star begins hydrogen burning within its core and reaches hydrostatic equilibrium it begins its life on the Main Sequence (MS) as a Zero-age Main Sequence (ZAMS) star. As stars evolve from purely hydrogen burning PMS stars, their core's helium to hydrogen ratio increases and the star moves away from the ZAMS. The ZAMS phase is modeled homogeneously and transformed with the onset of nuclear fusion into the non-homogeneous model with a helium core surrounded with a hydrogen burning shell (i.e.. non-processed composition) that is the Main Sequence (MS).

### **1.2.3 The Main Sequence (MS)**

The MS is where a star will spend the majority of its lifetime, generally marked by helium burning occurring in the stellar core which causes a large energy flux and the production of a convective core. The nuclear burning region of a star will encompass a larger percentage of the stellar interior from high to low mass stars. Higher mass stars have interior structures dominated by an outermost radiative zone, an intermediary convective zone, and an innermost nuclear burning region at their core. Solar mass stars have an outermost convective zone, an intermediate radiative zone, and an innermost nuclear burning core. Low mass stars are entirely convective in their interior, aside from their comparatively large nuclear burning core. In all cases energy is generated solely in the nuclear burning core in the form of gamma rays, and is transferred toward the surface through radiation or convection depending on which is more efficient at the star's temperature, opacity, and mass.

As the star continues its time on the MS, energy generation through nuclear fusion continues, converting hydrogen into helium, gradually altering the chemical composition of stellar interiors. Once hydrogen fuel stores have decreased within the star, energy generation slows to a stop in its core and the fusion process moves outward from the core to a helium shell surrounding it. If the mass of the star (and thus its temperature) are high enough, helium fusion can occur, but for small stars, this threshold is never met, and their helium core remains inert. These events mark the beginning of stellar death.

### **1.2.4 Stellar Demise**

As the rate of fusion decreases as the last of the star's fuel reserves are exhausted, the amount of energy generated within the star drops. To retain thermal equilibrium, the stellar temperature



and pressure in the core will decrease, which (to accommodate hydrostatic equilibrium) causes the core to contract, causing the the temperature to increase. The sharp rise in temperature causes a hydrogen burning shell to form around the core. This collapse converts the potential energy (from gravitation) into thermal (kinetic) energy directed into the hydrogen burning shell surrounding the helium core. The hydrogen burning shell expands, consuming more fuel in the stellar interior and generating more energy than the nuclear burning core had (by virtue of its access to a larger volume of stellar material). It is at this point that the star makes a slight jump from the MS track on the Hertzsprung-Russel (HR) diagram, and stellar demise begins. The star increases sharply in luminosity and size, becoming a red giant. While the red giant star is more luminous, and produces more energy, its surface has expanded and its surface area become quite large, causing the surface temperature to drop into the K and M spectral type regimes.

MS stars have two inevitable fates after leaving the MS: become a red giant, or a red supergiant. The lifetime of stars, what fusion takes place during their lives and how quickly they evolve off the MS are all decided by the star's initial mass. Hotter, bluer, more massive stars dissipate their fuel reserves rapidly and thus have short lifetimes, upon leaving the MS they will become supergiants. Cooler stars like our sun that are less massive can expect to live for as long as 10 billion years before they evolve into the red giant branch. Stars with masses less than  $0.8 M_{\odot}$  have not yet had time to evolve into red giants, as their hydrogen fuel stores have yet to be exhausted in the age of the Universe.

### **1.3 Multiple Star System Formation and Evolution**

In the previous section (§1.2) I have provided an outline of stellar formation and evolution; this section outlines how they may be affected by stellar binarity and multiplicity. The generally accepted synopsis of stellar evolution and formation remains the same in binary or higher order stars, with a few important distinctions. While at the same time, studies continue to show that stellar multiplicity may be more intimately related to all stellar formation. Additionally, observations at a variety of wavelengths continue to detect multiplicity (binary systems and higher order) at all stages of stellar evolution. As more discoveries of multiple systems are made amongst the youngest of these systems (Pre Main Sequence, PMS) there is increased focus on the idea that all stars may be born in multiple systems, that the binary fraction at different stellar ages may be a consequence of dynamical evolution driven internally or externally by the population of multiple systems in their primordial environment (Larson, 1972). If dynamical evolution is indeed an essential part of early stellar formation, binarity and multiplicity can be seen as a principle channel of star formation (Reipurth et al., 2014). As mentioned in §1.2 star formation begins in dense molecular clouds that lose hydrostatic equilibrium once they pass the Bonnor-Ebert limit of mass

and begin to collapse. Collapse and rotation of the cloud causes it to fragment, which is widely considered to be the catalyst in forming binary and higher order star systems. Fragmentation and multiplicity formation processes were studied by Machida et al. (2008) through the utilization of 3-D resistive magnetohydrodynamical (MHD) nested grid simulations starting with an isothermal cloud rotating in a uniform magnetic field near the Bonner-Ebert limit. A total of 147 models with varying initial conditions of magnetic, rotational, and thermal energies along with the amplitudes of the non-axis symmetric perturbation were calculated (Machida et al., 2008). An earlier study, Machida et al. (2007) documented the early evolution of the magnetic field and angular momentum of newly formed protostars, also using the 3-D MHD nested grid simulations, also beginning in an isothermal cloud rotating in a uniform magnetic field. There, it was found that the evolution of the angular momentum depends strongly on the evolution of the magnetic field, as angular momentum in the cloud being removed by magnetic effects, like magnetic braking, outflow, and jets. These magnetic effects result from tangled magnetic fields within the collapsing cloud (Tomisaka, 1998). These studies of the dynamic kinematics of these molecular clouds is used to inform the models of Machida et al. (2008), they found that the magnetic field and rotation are critical, as these forces cause the anisotropic patterns that in turn cause fragmentation. Machida et al. (2008) also found that the initial ratio of thermal to gravitational energy in the initial cloud (which is related to the cloud's stability) could also affect the cloud's fragmentation. Bate (2009) explored multiplicity frequency in an unstable collapsing cloud with an initial mass of  $500M_{\odot}$ , a Jean's mass of  $1 M_{\odot}$ , and a turbulent, high Mach number (13.7) velocity field. This resulted in a multiplicity fraction that included a high population of brown dwarfs. While the simulation omits important physical information like the magnetic and radiative feedback, the results match to a wide range of binary parameters (Reipurth et al., 2014). It is important to note that Machida et al. (2008) show convincingly that cloud rotation promotes fragmentation at all stages of the cloud's evolution, while the magnetic field delays, or in some cases even suppresses fragmentation. They had found that fragmentation, (and presumably, star formation) depends heavily on the magnetic field and rotation of the cloud, but is also slightly dependant on its thermal energy and amplitude of its non-axis symmetric perturbation. Additionally, Machida et al. (2008) found that the distributions of the distances between the fragments exist in two distinct classes: fragments formed during the adiabatic phase have wide separations (3–300 AU), while fragments formed in the second collapse of the cloud, during protostellar phases, have much narrower separations (0.007–0.3 AU). These findings indicate a bimodal distribution for the radial separation of the protostar. In terms specific to multiple star formation Machida et al. (2004) concluded certain conditions being met at the isothermal phase in the cloud's evolution causes resultant fragments to form binary or higher order multiple stars. In order for fragments to form in this phase and lead to multiples, the adiabatic core of the cloud must fragment, which requires the central gas within the molecular cloud to form a thin disk

or bar in the isothermal phase. The second condition restricts the oblateness ( $\varepsilon_{ob}$ ) or shape of the central region of the cloud into two ranges that are likely to survive mergers that can obliterate multiplicity systems.  $0 < \varepsilon_{ob} < 2$ , or,  $\varepsilon_{ob} > 2$ . Machida et al. (2004) defines these ranges as survival conditions against mergers. Outside of these domains, a few fragments do survive without completing mergers by the end of the simulation, but the separation between the cores shrinks with time and merger is ultimately inevitable. These out of domain fragments do not result in the formation of binary or higher order systems in their simulations.

### 1.3.1 Tertiary and Higher Order Systems

Nearly half of the known tertiary and quadruple systems (star systems with three or four stellar components orbiting a common center of mass) were identified in the last twenty years through radial velocity (RV) extraction and high resolution imaging. Tokovinin (1997) studied the statistics of quadruple star systems using the updated Multiple Star Catalog, or MSC (Tokovinin, 1997). In that work quadruple star systems are defined as two close binary pairs orbiting a common center of mass.

The frequency of binaries with and without tertiary companions is necessary in fully understanding stellar formation and evolution. Tertiary systems may be responsible for perturbing the orbit of the stars in its binary companion pair closer together, into a compact, shorter period binary. While the presence of a third star in an orbit around a binary system can significantly alter the evolution of all three stars through their rich dynamical behavior (Kozai, 1962), the long term evolution of stellar triples is poorly understood (Toonen et al., 2016). Recent studies have found that nearly 10% of low mass stars exist in triple systems (Tokovinin, 2008, 2014; Moe & Di Stefano, 2017). For higher mass stars of spectral type B, nearly 50% reside in triple systems (Evans, 2011).

Generally, theoretical studies of triple systems has two focuses: three body dynamics (governed by gravitational orbital evolution), and stellar evolution (governed by the internal nuclear burning processes of the stellar members and their mutual influence). Toonen et al. (2016) notes that the dynamical interaction between the three stars can give rise to Lidov-Kozai cycles, which cause the eccentricity of the inner orbit and the inclination of the outer orbit to vary with time. In turn, this periodicity can lead to the enhancement of tidal friction, gravitational wave emission, and interactions between the constituent stars like mass transfer.

The expansion of knowledge in the field of binary and higher order multiplicity systems, their formation, and evolution is profound. Still, how this relates to the fragmentation of collapsing molecular clouds and fundamentally, if all stars are indeed formed in multiples as has been postulated is far from known with any degree of certainty. As observational and analytical methods

are refined, it is likely that more young multiple systems will be observed continuing the trend seen in the last two decades. While the dynamical processes of tertiary systems formation and evolution remains an open and exciting topic, in this work (§3.4.3 binary systems with a potential tertiary member are identified for further study. Additionally, a Pre-Main Sequence (PMS) Eclipsing Binary (EB) tertiary system is explored in the following Chapter 4.

## 1.4 Binary Systems: Spectroscopic & Eclipsing

Binary systems come in a wide range of mass and temperature ratios, ages, and spectral classes. Generally, they are organized into two types: long period, wide separation and short period, short separation systems. Long period systems are excluded from these projects as cadence windows and observational periods are usually much shorter than hundreds of days. Capturing more than one eclipsing event or inferring the presence of a secondary (beyond spectroscopic radial velocities studies) is not suited for the analysis outlined here for close, shortest period systems. Neither the *APOGEE/Kepler* binaries (see §5) or the *AuPOGEE/TESS* binaries (see §3) have instrumental windows conducive to the observation of long period binary systems.

Eclipsing Binary (EB) systems have an orbital plane close to the line of sight of its observer, which allows eclipsing events to be seen as one stellar component passes in front of its binary companion. The result is a variable star whose light curves are characterized by drops in intensity when the eclipses take place. The magnitude of the drops in brightness depends on the relative surface brightness of the stars in the binary.

Eclipsing Binary Systems serve as an Astrophysicist’s laboratory, but when these EBs are also observed spectroscopically, the coveted stellar and orbital parameters that we measure there are more constrained and precise. Spectroscopic Eclipsing Binaries (SEBs) come in two flavors: SEB I and SEB II. SEB I systems have only the contribution from the primary star in their spectra, while SEB II systems have spectra with contributions from both the primary and secondary binary component. A complete spectroscopic and photometric analysis of eclipsing binary systems yields highly accurate properties of the system and of its stellar components, in such a manner that they are determined independently of their distance and other theoretical assumptions (e.g., Gómez Maqueo Chew et al. (2006); Stassun et al. (2014)).

Recent work from Prša et al. (2022) catalogs 4584 eclipsing binaries observed during the first two years (or, 26 sectors) of the *TESS* mission. It should be noted that the sample of EBs in that work, and all observations by *TESS* are selected to maximize exoplanet detection yields. Guest investigator targets are selected through submitted proposals which encompass a diverse collection of science goals. Prša et al. (2022) notes that these data are therefore impossible to use toward a statistical representative distribution of parameters, but defines catalog completeness as the overall

EB detection success in the short (2-minute) cadence target observations. Prša et al. (2022) also noted that the EB TESS catalog can be used for bulk analysis along with providing critical information on individual EB systems. Additionally, two interesting observations were made in this work: the galactic distribution of southern hemisphere EBs ( $-90 < b < -10$ ) is nearly constant. This observation is at odds with *Kepler* observations (Prša et al., 2011) in which no such constant distribution was seen. The second is a lopsidedness between the southern and northern hemisphere observations. These effects are likely due to the non-uniform target selection of *TESS* who’s main prerogative is exoplanet detection, and, the relatively bright magnitude breakdown limit of *TESS* (Prša et al., 2022) which reduces the dependence of eclipse probability on stellar populations. The last cause of these effects was attributed to the fraction of time the Galactic plane was in or near the continuous viewing zone (CVZ). Prša et al. (2022) explains that they expect that EBs observed in *TESS* FFIs will create a more uniform sample that will be more representative of true galactic distributions (see Prša et al. (2022) Fig.21), conclusive that the lopsidedness between hemispheres is due largely to the change in bore-sight (optical axis) between them.

### 1.4.1 Radial Velocity Extraction from *APOGEE* Spectroscopy

Radial velocity estimates from a double lined spectroscopic binary (SEB II) are effective in extracting the masses of the components of the binary system. Periodic changes in the Doppler shifts of the spectral lines from the components in a SEB II (providing the system is along the line of sight) are used to determine the radial velocity of the components based on this observed wavelength shift. For each stellar component in the binary, radial velocity curves have sinusoidal behavior (most pronounced in binaries with a circular orbit), where the maximum velocity amplitude indicates the velocity of the star with respect to the system’s center of mass.

Radial velocity extraction from spectroscopic observations is usually undertaken using the Cross-Correlation Function (CCF) as done in the *APOGEE* data reduction pipeline (Nidever et al., 2015). In this methodology, the observed spectrum  $s(n)$  of a target is cross correlated against a template spectrum,  $t(n)$ .

$$c(x) = \int_{-\infty}^{\infty} s(n)t(n-x)dn \quad (1.1)$$

Due to Doppler Shifting as the binary components orbit around their common center of mass, the template spectrum must be shifted in order to coincide with the observed spectrum. This shift ( $x$ ) behaves following Equation 1.2 below:

$$x = \left[1 + \frac{V}{c}\right] \quad (1.2)$$

where ( $c$ ) is the speed of light and ( $V$ ) is the relative velocity between them. The functions  $s(n)$

and  $t(n)$  are composed of  $N$  discrete bins sampled at equal intervals along  $\ln(\lambda)$  where  $\lambda$  is wavelength. Each interval contains a measure of fractional flux density relative to the continuum being set to unity. If the continuum is subtracted, Root Mean Squares (RMS) uncertainties of that spectrum can be described by:

$$\sigma_s^2 = \left[ \frac{\sum_{n=1}^N s(n)^2}{N} \right]; \sigma_t^2 = \left[ \frac{\sum_{n=1}^N t(n)^2}{N} \right] \quad (1.3)$$

The normalized spectrum can then be defined as:

$$c(x) = \frac{1}{N\sigma_s\sigma_t} \sum_{n=1}^N s(n)t(n-x) \quad (1.4)$$

Equation 1.4 is most efficiently modeled via a Fourier Transform (FT), this is due to the convolution in the  $x$  domain which then becomes simple multiplication. In general, in SEB II spectroscopic observations, the (combined) spectrum generally produces a double lined CCF, whether or not the peaks will be separated on the  $\lambda(\ln(\lambda))$  axis depends on three factors. The first being the spectral resolutions of the observations, second being the projected rotational velocities and orbital velocities at the time of observation for the two stars in the binary, and the third being a proper choice of spectral template.

The CCF methodology works spectroscopic observations consist of an observed spectrum (convolved with a spectroscopic instrumental profile, a radial component of the microturbulence in the stellar atmosphere, or with rotational broadening) and a second function called the Broadening Function (BF) which contains important RV information. The CCF methodology yields results very close to the actual convolution that occurs in an *APOGEE* spectroscopic observations. However, cross-correlating a template spectrum with a spectrum yields a function that inherits the natural broadening components in both the template and observed spectra. In terms of modeling RV peaks, CCF extraction methodology presents peak-pulling and peak-pulling effects while the BF consistently exhibits more clearly defined and separated RV peaks.

The spectral line broadening functions for contact binaries was first studied by Anderson & Shu (1979) and later re-investigated in a series of papers: Rucinski (1992); Rucinski et al. (1993); Lu et al. (2001). A further description can be found in Rucinski (1999), while a description of the software used in extracting the BF can be found in Rawls et al. (2016); Clark Cunningham et al. (2019).

## 1.5 Stellar Chronometers

Accurately measuring the ages of the stars is fundamental to our understanding on all scales of cosmic evolution; from galactic evolution to stellar evolution to that of planetary systems. A number of methodologies exist for measuring the ages of stars, referred to as Stellar Chronometers. A *chemical clock* stellar chronometer utilizes a star's chemical abundance ratios which are produced at different time scales and in different stages in star's evolution (see §1.2). Recent work has shown that these *chemical clocks* may not be universal, and may only be valid in the scope of our local galactic neighborhood (Casali et al., 2020).

Stars can also be aged through the use of theoretical stellar evolutionary sequences or isochrones. Isochrones are stellar evolutionary tracks that objects of a certain age follow on the HR diagram. Like *chemical clock* chronometers, isochrone interpolation has its weaknesses in aging stars. Many of these issues arise because of the non-linear mapping from stellar parameters (like age) to observable data. This can manifest in the over or underestimation in error limits. Techniques outlined by Jørgensen & Lindegren (2005) offer an alternative approach that attempts to avoid these shortcomings through the systematic study of relevant regions of parameter space. The calculation of the G function summarizes the posterior knowledge of an star's individual age which allows the derivation of age estimates and confidence levels.

### 1.5.1 Lithium Emission

Lithium emission is a *chemical clock* because lithium depletion in stars occurs above 2.25 MK making lithium depletion especially useful in tracing stellar age though relations to convection processes (Soderblom et al., 1999) in solar like stars. During the PMS phase (§1.2.1) low mass stars (with masses equal or less to the Sun) should experience a significant Lithium and deuterium depletion. Essentially, deuterium and lithium burning are precursors to the hydrogen burning that will take place once the star joins the MS. Timescales for lithium and deuterium burning are dependant on the mass of the star. The smallest stars will deplete their lithium reserves perpetually, while brown dwarfs will only be able to burn deuterium but never lithium (Dantona & Mazzitelli, 1984; Nelson et al., 1993). For any stellar object, the depletion of lithium is monotonically related to stellar age: as stars do not create lithium through nuclear reactions, but only destroy it (Hillenbrand, 2009).

Lithium depletion trends in sub-solar populations of PMS, ZAMS, and MS stars have been used to estimate stellar age. At constant ages (i.e., clusters who's stellar population form at approximately the same time) there is considerable scatter in both the observed equivalent widths and the derived abundances at constant mass. This scatter in surface abundances is most likely related

to the dispersion in stellar rotation speeds amongst the coetaneous sample.

## 1.5.2 Ca II H&K Absorption

There exists an empirical relationship between stellar rotation and activity of FGK dwarfs, and Ca II H&K absorption is a commonly used tracer of stellar chromospheric activity. This empowers emission cores in the H & K lines of Ca II near 3950 Å to serve as a chemical clock stellar chronometer.

This chronometer was employed by Clark Cunningham et al. (2020) in aging PMS stars in a tertiary system, HD-542368 (see also, §4.3.5.2). The EB component of HD-542368 (HD-542368A) is likely tidally synchronized, considering the short orbital period of the eclipsing pair. This tidal interaction likely has effected the EB's stellar components rotation speed. Indeed, the light curve of the HD542368 contains a sinusoidal variation, having a period of very near the orbital period of the binary. This confirms that the stars have been tidally effected from their close separation. In the specific case of the HD-542368 system, the single K dwarf tertiary star, being unaffected by tidal interaction in the EB, served as a proper site for Ca II H&K absorption age estimates.

The Ca II H&K analysis of the WiFeS spectrum for HD 54236B was compared to the spectra of three different open clusters spanning a range of ages. When these comparisons are taken together, an age for HD 54236B (and therefore of the HD 54236 system) that is older than the Pleiades (~130 Myr) and younger than M7 (~300 Myr) is strongly applied (Clark Cunningham et al., 2020). Chapter 4 of this dissertation presents the complete analysis and results of the HD-542368 system.

## 1.6 Age Estimates

The chronometers described above and the planes of the HR-diagram are used to arrive at age estimates for all of the SEBs within the *Kepler/APOGEE* overlap discussed in Chapter 3 and for the young EB tertiary system discussed in Chapter 4. In both studies the age estimates proved coevality, which in turn calibrates stellar evolution theory, these are described in the following section, §1.6.1.

### 1.6.1 The Coevality Hypothesis

The fundamentals of stellar evolution theory rely on an assumption that stars in multiplicity system (binary and higher order systems, clusters) have stellar components that form at approximately the same time. This is commonly referred the Coevality Hypothesis. Generally, EBs with components ( $M_{1,2} > 1.2M_{\odot}$ ) perform generally well on the prediction of evolutionary models



(Stassun et al., 2014) Low mass MS stars ( $\sim M_{1,2} < 0.8M_{\odot}$ ) were seen to have large discrepancy in model predicted ages, perhaps due to magnetic activity interfering with convection. The inhibition of convection in the star would likely cause its radius to be larger than predicted by 10-20 % (Stassun et al., 2014). When effects from stellar activity are removed, low mass PMS stars with ages  $\sim 1$  Myr can show non-coevality of  $\sim 30$  %, attributed to formation effects. This same magnetic inhibition of convection was theorized by MacDonald & Mullan (2017) to be the cause of failed coevality tests between members of USco. The age estimates for the four low mass stars were found to be best fit with previous independent age estimates for high mass stars in the same association MacDonald & Mullan (2017) once stellar magnetic activity was considered. This resulted in all of the stellar members of USco being regarded as coeval. Prior to this the association had had a lasting age discrepancy between its high and low mass members.

### 1.6.2 Isochrones

Observational data, such as photometric and spectroscopic solutions to stellar parameters and theoretical isochrones form another stellar chronometer of considerable practical importance. Stellar ages are often estimated using this technique, however uncertainties in isochrone ages are often underestimated in the literature (Lachaume et al., 1999). Recent progress has implemented Bayesian probability theory (e.g., Jørgensen & Lindegren (2005), Valls-Gabaud (2014), Hills et al. (2015) in an attempt to investigate isochrone consistency and access possible statistical biases within the isochrone fitting procedure. For these reasons, isochrone fitting is usually a chronometer used in validation with other more empirical aging methods as outlined above.

### 1.6.3 Galactic Motion

Galactic motion can be used in a number of analysis including to verify that stellar components are indeed members of the same gravitationally bound multiplicity system, as was done in Clark Cunningham et al. (2020) with the PMS tertiary system HD 54236. Additionally, the galactic velocity vector can be used to aid in the determination of stellar associations. Both applications can serve as a follow-up confirmation of the coevality of a multiplicity of a system. Gaia DR2 parallax estimates (Bailer-Jones et al., 2018) allow a distance estimate, this, combined with proper motion, and RV estimates can be used to solve for the galactic motion vector. In applicable cases (see Chapter 4, 4) this vector is used to determine stellar association and limit age estimates.

## 1.6.4 Stellar Associations

The galactic motion of a system can be cross-matched against candidate populations to find its stellar association membership. A system’s present-day position and velocity can be used to numerically integrate the star’s orbit around the galactic center backward in time to find its initial position and velocity. As was completed with the tertiary HD 54236A, in which its galactic motion vector was cross matched against a number of recently discovered co-moving groups (Clark Cunningham et al., 2020). In that study it was concluded that HD 54236A likely had the stellar stream Thea-301 as its progenitor, which has six mutual members in the AB Doradus association (Messina et al., 2010). These two populations, AB Doradus and Theia 301 are also estimated to have similar ages; the age of Their-301 obtained via isochrone fitting is  $8.29 \text{ /pm}0.16\text{dex}$ , while AB Dor is estimated at 130-200 Myr (Bell et al., 2015). These are both consistent with the age of HD 54236 derived in (Clark Cunningham et al., 2020) through lithium abundances and Ca II H&K.

The establishment of stellar association membership or stellar ancestry can also help to alleviate long standing contention within the field, for example what has been dubbed the ‘Luminosity problem of AB Dor’ whose been a subject of debate since the work of Close et al. (2005) estimated the age of the system to be only  $\sim 50$  Myr. Close et al. (2005) had directly imaged the lowest mass component within the system, AB Dor C, and used astrometric observations to find its orbital solutions and a dynamic mass estimate of  $\sim 90 \pm 10 M_{jup}$ . Subsequent comparisons of near IR magnitudes and effective temperatures from theoretical models to these observations created tension between them, prompting Close et al. (2005) to conclude that stellar models overestimate the luminosities of low-mass objects. It should not be ignored, however, that this contention between theory and observation is based on the assumption that AB Dor C is a single object. AB Dor C could be instead, an unresolved Binary Drown Dwarf (BBD). Described by Marois et al. (2005) the BBD hypothesis is constructed assuming two brown dwarfs with a total mass roughly equal to the dynamical mass of AB Dor C ( $90 \pm 10 M_{jup}$ ) reported by Close et al. (2005). Using the most recent scale of spectral type to effective temperature, with the derived spectral type of  $M8 \pm 1$  (also from Close et al. (2005)), AB Dor C is projected to have an effective temperature of  $2710 \pm_{310}^{170}$  K. Marois et al. (2005) successfully showed that a BBD with a mass ratio  $q \geq 0.3$  can fit all observational data within accepted error. Marois et al. (2005) also showed, the less massive member of the BBD is predicted to be 2–4 magnitudes fainter in the  $H$  band, and thus undetectable in the observations of Close et al. (2005).

An alternative interpretation by Luhman et al. (2005) used color-magnitude diagrams to find that the AB Dor moving group to be roughly the same age (or coeval) with the Pleiades ( $\tau = 100$ – $125$  Myr) and clearly older than IC 2391 whose age estimate is  $\tau = 35$ – $50$  Myr. When the more

youthful age estimate of  $\tau = 50$  Myr from Close et al. (2005) is used, the luminosity of AB Dor C becomes highly discrepant with the predictions of stellar evolutionary models. However, an older age estimate like those suggested by Luhman et al. (2005) of  $\tau = 100\text{--}125$  Myr or  $\tau \sim 225$  Myr found in Clark Cunningham et al. (2020) is used, the luminosity discrepancy disappears and stellar evolutionary models do not appear to underestimate the luminosity of low mass stars. An older age estimate for the AB Dor system mitigates its luminosity degeneracy without requiring its binary brown dwarf complexity of Marois et al. (2005), but also without excluding it.

The next chapter, §2 provides an outline of the methodologies used in the projects contained in this dissertation. Followed by Chapters 3, 4, and 5, which include the project's associated publication. Lastly, in Chapter 6, is a discussion surrounding the results of the projects discussed, potential further implications, and later work.

# CHAPTER 2

## Method

In each project included here, I utilized a combination of photometric and spectroscopic observations from a variety of ground and space based missions. The methodologies are described in the following order: Photometric observations and analysis, spectroscopic observations and analysis.

### 2.1 Photometric Observations and Analysis

Photometry is used to measure the flux from an object over time. In this work I have used photometric data from the *Kepler* (§3), *KELT* (§4), *PEST* (§4), and *TESS* (§4, §5) missions.

#### 2.1.1 Kepler Photometry

Kepler photometry was employed by Clark Cunningham et al. (2019) in the study of 33 SEBs present within the *APOGEE/Kepler* overlap (see §3) to compute full orbital solutions, with a suite of stellar parameters, for 7 of the 33 systems. The sample selection with that work began in the *Kepler* Eclipsing Binary Catalogue, compiled by Kirk et al. (2016). We filtered targets in the *Kepler* Eclipsing Binary Catalogue to identify those with multiple eclipsing events visible in their photometry. By requiring these systems to have both primary and secondary eclipsing events, we effectively established an inclination limit of around 90 degrees. Systems were also required to have a semi- or well-detached morphology, determined through the shape of the eclipsing events, and a luminosity  $H \leq 14$  magnitude. Targets were also required to have multiple  $\text{ApVisit}$  spectra, and therefore multiple CCF RV estimates from the *APOGEE* pipeline. Lastly, targets must have at least three visits from *APOGEE* resulting in  $\text{ApVisit}$  spectra, free of quality flags. From the *Kepler* Eclipsing Binary Catalogue, these criteria yielded 33 candidates, and of these, Clark Cunningham et al. (2019) (see §3) performed a detailed analysis of seven systems.

In Clark Cunningham et al. (2019) (§3) *Kepler* simple aperture photometry (SAP)) is utilized to create light curves for each of the 33 candidate systems. Each target’s LC was normalized by the median flux value from all available observations. Poor quality data was de-weighted by

identifying time indices with *Kepler* quality flags and inflating the normalized flux uncertainties at the identified times by a factor of 10. Of the 33 candidate *APOGEE/Kepler* binary systems, 11 were identified as Spectroscopic Eclipsing Binaries, with both primary and secondary contributions in their  $A_{p\text{Visit}}$  spectra (SEB II systems). Their *Kepler* photometry is also utilized in the simultaneous LC-Radial Velocity (RV) modeling, completed by *KEBLAT* (see §3.2.4) in Clark Cunningham et al. (2019).

### 2.1.2 The Kilodegree Extremely Little Telescope South (*KELT* South )

The Kilodegree Extremely Little Telescope South is located at the South African Astronomical Observatory (SAAO) Sutherland observing station. *KELT* South photometry was utilized in the study of the young EB tertiary system analyzes in Clark Cunningham et al. (2020) (§4). The *KELT* observing setup employs a wide field and large pixel scale (23 arcseconds per pixel). Because of this, the *KELT* South photometric observations of the system HD 54236A are blended with light from neighboring stars (see §4.2.1.1). The largest contribution of blended flux comes from, HD 54262, found 54 arcseconds east of the EB HD 54236A, with  $V=9.31$ . Based on the reported proper motion of HD 54262 compared to the reported proper motion of HD 54236 indicates that the systems are not physically associated beyond this Line of Sight (LOS) contamination. The *KELT*-South spectroscopic observations were used to complete an initial periodicity analysis, which yielded a most likely orbital period of  $\sim 2.4$  d and also found an out-of-eclipse light curve that varies nearly as a sinusoid, with a best fit period of 2.39055 d for HD 54236A, (the primary eclipsing binary component of the HD 54236 system).

### 2.1.3 The Perth Exoplanet Survey Telescope (*PEST*)

The Perth Exoplanet Survey Telescope (*PEST*) is a partner of the *KELT* South survey; it consists of a 12" Meade LX200 SCT  $f/10$  telescope, an SBIG ST-8XME 1.2 arcsec/pixel camera, and a focal reducer yielding  $f/5$ . Operated by T.G. Tan, *PEST* observed the EB HD 54236A (4) on April 25, 2012 for an estimated 119 minutes surrounding the predicted time of primary eclipse in the Cousins  $R$  band (Clark Cunningham et al., 2020). The ephemeris solution derived from the *PEST* photometry was poor due to over two years having elapsed between the original observations and the *PEST* observations. The *KELT* South photometry did capture the last hour of the primary eclipsing event in addition to the following hour after. While the *PEST* LC is less contaminated than that of the *KELT* South photometry, it does still include the light contamination of HD 54236 B, the faint tertiary companion to the EB.

*PEST* photometric data is combined with the *KELT* South photometry data scaled by a factor of 3 in flux to account for the additional dilution of the *KELT* South data from the high proper motion

bright star HD 54262 (the main contaminant flux contributor in the LOS of the *KELT* South LC) (Clark Cunningham et al., 2020). The addition of the *PEST* photometry allowed the expansion of the time baseline, which allowed the refining of the orbital period. *PEST* photometry was also used to solve for the ephemeris of the system, likely due to the elapsed time between the original observations and the subsequent *PEST* observations. *PEST* had observed the EB HD 54236A on April 12, 2015 for a total of 119 minutes around the time of the predicted primary eclipsing event in the Cousins *R* band. Although the ephemeris of the system was a poor solution, the *PEST* observations did capture the last four of the primary eclipsing event egress, and an additional hour after the eclipsing event. An advantage to the *PEST* photometry is its exclusion of the light contamination of HD 54262, the bright contaminant neighbor to the west of the EB. However, the *PEST* LC does include the contamination from the faint visual companion, HD 54236B.

The raw photometry of the combined HD 54236A/B system was extracted using the `C-Munipack` software package<sup>1</sup> (written by David Motl) to perform aperture photometry (Clark Cunningham et al., 2020). Relative photometry was derived using a set of three nearby comparison stars via a custom-written program. The *PEST* LC is shown in 4.2.1.2, when combined with the *KELT* South photometric data scaled by a factor of 3 in flux to account of the dilution of *KELT* data contributed by the high proper motion star to the west (HD 54262). The addition of the *PEST* photometry empowered the refinement of the orbital period acquired from the *KELT* periodicity analysis due to the expanded time baseline. The *PEST* LC for the HD 54236 EB tertiary is shown in 4.2.

#### 2.1.4 The Transiting Exoplanet Survey Satellite (*TESS* Photometry)

NASA’s Transiting Exoplanet Survey Satellite collects photometric data of stars from the entire sky, divided into 26 sectors. Like its predecessor *Kepler*, *TESS* collects photometric data which can be analyzed for periodic changes in flux. Periodic changes in brightness can indicate that the system is an eclipsing binary pair. *TESS* catalogs thousands of exoplanet candidates using this same ‘transit method’. Recent work from the *TESS* Eclipsing Binary Working Group (EBWG) by Prša et al. (2022) identifies 4,584 eclipsing binaries in *TESS* sectors 1-26, the majority of which have been vetted and validated with short (2-minute) *TESS* cadences. The *TESS* mission observes sectors spanning  $24^\circ \times 96^\circ$  each being observed for two *TESS* orbits, or roughly 27 days, which effectively restricts period extraction to an upper limit of 27 d. However, this limit has been harmonious in all projects covered in this work, as all involve close, short period, binary systems.

*TESS* photometry is used in Clark Cunningham et al. (2020) (4), and in §5. In Clark Cunningham et al. (2020), *TESS* 2-min cadence photometric observations of the HD 54236 system for

---

<sup>1</sup><http://c-munipack.sourceforge.net/>

Sectors 6, 7, and 8 were first optimized using the aperture selected by the *SPOC* pipeline (Jenkins et al., 2016) and processed with the `Lightkurve` python module. The aperture mask was then chosen to eliminate the western high proper motion star, HD 54262 (TIC 767642477) so as to avoid the blending of their photometry. In order to estimate the background, a brightness threshold was instituted to ensure the pixels in the Target Pixel File (TPS) are 0.1% times the standard deviation below the overall median flux of pixels in the assigned aperture. The background was then subtracted from the photometric source signal and normalized by the median flux.

To assist with the normalization of flux baselines, a biweighted midcorrelation (from the `wotan` package) filter was used. To ensure that three eclipsing events were included in each window and not over-fitted by the smoothing function, a window length of three times the  $\sim 2.4$  d period estimated for the system. The *TESS* long-term de-trended LC is shown in 4.2.1.3. Then, using `Astropy` box least squares (BLS) methodology (also used in 5 for periodicity analysis) to estimate the period of the evident out-of-transit variations found in the LC of HD 54236A.

In §5, *TESS* photometry is used to evaluate *APOGEE* identified binary systems, dubbed the *Gold Sample* (Price-Whelan et al., 2020). After being cross-matched via right ascension and declination to *TESS* targets, matches had their photometric observations downloaded from the *MAST* archive. Some binaries within the established *Gold Sample/TESS* overlap had processed light curves from the MIT Quick Look Pipeline (Huang et al., 2020a; Kunimoto et al., 2021) which are similarly acquired through the *MAST* archive.

Most targets within the *Gold Sample/TESS* overlap had photometric observations from a number of *TESS* sectors. Depending on the target, 2 min cadence LCs or 30 min cadence LC are utilized. The LCs for each target are normalized using a Biweighted MidCorrelation filter, from the `wotan` package. To ensure no eclipsing events are lost during photometric processing, windows are chosen to be three times the *APOGEE Gold Sample* period estimate. The long-term de-trended light curves for the *Gold Sample/TESS* overlap were studied by eye to identify singular or multiple eclipsing events. In the case of 5, both SAP and Pre-Data Conditioned Simple Aperture Photometry (PDCSAP) are utilized depending on the target binary. In certain cases (like TIC 021980925) both SAP and PDCSAP must be modeled as to include both primary and secondary eclipsing events.

Again, `Astropy` (Hartman & Bakos, 2016) BLS periodicity analysis is completed on the targets in the *Gold Sample/TESS* overlap, with iteration centered about the *APOGEE Gold Sample* period result. Once period estimates were extracted for the systems in our subset their de-trended normalized LCs were folded onto their respective *TESS* period estimate. The *TESS* photometry for each target was also folded onto its reported *APOGEE Gold Sample* orbital period, and the two scrutinized for clarity in eclipses. In almost every case of the ten eclipsing binaries with the overlap, the *TESS* photometry period estimate increased the orbital period accuracy by at least one order of magnitude. Three of the targets within the *Gold Sample/TESS* overlap were found to be

Spectroscopic Eclipsing Binaries with both star’s spectral signature present. In these cases, through simultaneous spectroscopic and photometric modeling, *TESS* period estimates are also shown to have phase agreement with Radial Velocity (RV) curves.

## 2.2 Spectroscopic Observations and Analysis

Spectroscopic observations, (primarily from Sloan Digital Sky Survey’s Apache Point Observatory Galactic Evolution Experiment, *APOGEE*) that are used throughout each work are described below.

In the *APOGEE/Kepler* project of Clark Cunningham et al. (2019) outlined in 3, spectroscopic observations from *APOGEE* were used to determine RV estimates for each `ApVisit` spectrum available. In those cases the disentanglement of primary and secondary RV components was successful via the BF method of RV extraction. In Clark Cunningham et al. (2020) RVs extracted with CCF methodology are utilized from the `ApStar` averaged and individual `ApVisit` spectral observations. Both the CCF and BF RV extraction methods are used, depending on which system is being analyzed. In the study of the *APOGEE Gold Sample/TESS* overlap, three out of the 11 total EBs were conducive to the BF RV extraction, as SEB IIs. The remainder of the subset were limited to the CCF RV extraction results (which, by nature of *APOGEE* assumes a single star only) from the pipeline (Nidever et al., 2015).

*APOGEE* was not designed with binary star characterisation as the highest priority; its main goal collecting as many spectroscopic observations from a variety of objects in order to probe the elemental abundances and kinematics of our galaxy. The high resolution spectra that *APOGEE* collects provide detailed information about individual stars, but does so under the assumption that all observations taken are composed by singular stellar components. Price-Whelan & Goodman (2018) introduced modification to the `ApVisit` radial velocity uncertainties to attempt to account for the *APOGEE* data reduction pipeline generally underestimating RV uncertainties. Work from El-Badry et al. (2017) quantified the effect of this assumption on a system’s extracted effective temperature which scales proportionally to the systems mass ratio,  $q$ . Still, *APOGEE* arguably has the best coverage of both spatial reach around the Milky Way and on the color-magnitude diagram, and offers multi-epoch data. Additionally, a small number (5) of *APOGEE* fields were designed specifically for companion studies; targets in these fields have more than ten `ApVisit` spectra spaced to enable binary and multiplicity system characterization.



## 2.3 APOGEE Spectroscopy

*SDSS-APOGEE* operates with the main science goal of gathering spectroscopic observations of hundreds of thousands of stars to better understand the former, current, and future chemical evolution of the Milky Way galaxy. The *APOGEE* mission’s standard observing mode has a total exposure time of about three hours that is often gradually collected over a number of  $\text{ApVisit}$  spectra usually gathered over different days. These  $\text{ApVisit}$  spectra are combined to form a singular spectrum per target, called an  $\text{ApStar}$  spectrum. Both  $\text{ApVisit}$  and  $\text{ApStar}$  spectroscopic observations for each target are available on the SDSS Science Archive Server (SDSS-SAS).

In §3, spectroscopic observations from *APOGEE* are combined with *Kepler* photometric analysis to model the binary orbit and directly measure stellar parameters like mass and radius. These stellar parameters are then used to constrain stellar evolution and explore stellar populations and orbital kinematics. In that work (Clark Cunningham et al. (2019) §3), we identified a total of 33 total promising candidates within the *APOGEE/Kepler* observational overlap and extract stellar parameters and orbital solutions from seven of this subset. The selection criteria for the 33 systems included targets having both primary and secondary eclipses visible by *Kepler*, a magnitude limit of  $H < 14$ , sufficiently high  $S/N$  ratio, and multiple  $\text{ApVisit}$  spectra with no quality flags present. 3.1 lists all candidates meeting this criteria.

*APOGEE* spectroscopy was used again in my latest work (§5 to study the overlap between the *APOGEE Gold Sample* (Price-Whelan et al., 2020) (hereafter, *AuPOGEE*) and *TESS* photometric observations. *AuPOGEE* identified several promising spectroscopic binary systems within the *APOGEE* field (see §5). These systems had met a number of criteria, listed as follows:

- Gold Sample Sources must have a match to a *Gaia* source within two arc seconds of the source’s reported 2MASS position,
- Each source has a stellar mass estimate in the STARHORSE (Queiroz et al., 2020) catalog,
- No *Gaia* targets can be within 2 arcsec of the source with  $G$  band magnitude differences  $\Delta G > -5$ , this removes stellar neighbors that would lie within the same *APOGEE* fiber as the source, and could therefore contaminate its spectrum,
- There must be no additional *Gaia* sources within 10 arcsec that have a  $G$  band magnitude difference  $\Delta G > 2.5$ , this excludes sources with bright neighboring stars,
- To reflect reasonable stellar parameters,  $-0.5 < \log g < 5.5$ ,
- An effective temperature range of  $3500 < T_{eff} < 8000$ ,
- $-2.5 < [M/H] < 0.5$  metallicity range,

- $SMAP < 0.5 km s^{-1}$  which excludes sources with large inferred excess variances,
- Each source must have more than 5 visit spectra,  $n_{ApVisit} > 5$ .

Once these criteria are applied, the Gold Sample has a census of 1,032 binary systems with unimodal samplings, with 492 systems that have bimodal samplings.

The criteria for the *AuPOGEE/TESS* (§5) and that of the *APOGEE/Kepler* (§3) both include a minimum number of  $ApVisit$  spectra  $n_{ApVisit} > 5$ . As previously noted, the majority of *APOGEE* targets have the observation window of three hours covered in more than one  $ApVisit$ . Additionally, *APOGEE* will collect the required number of observations as to allow a  $ApStar$  spectrum to reach a desired signal to noise ratio (S/N). The distribution of  $ApVisit$  spectra within the *AuPOGEE/TESS* overlap is presented in the following figure:

**Figure: 2.1** *APOGEE*  $ApVisit$  Distribution Across *AuPOGEE*

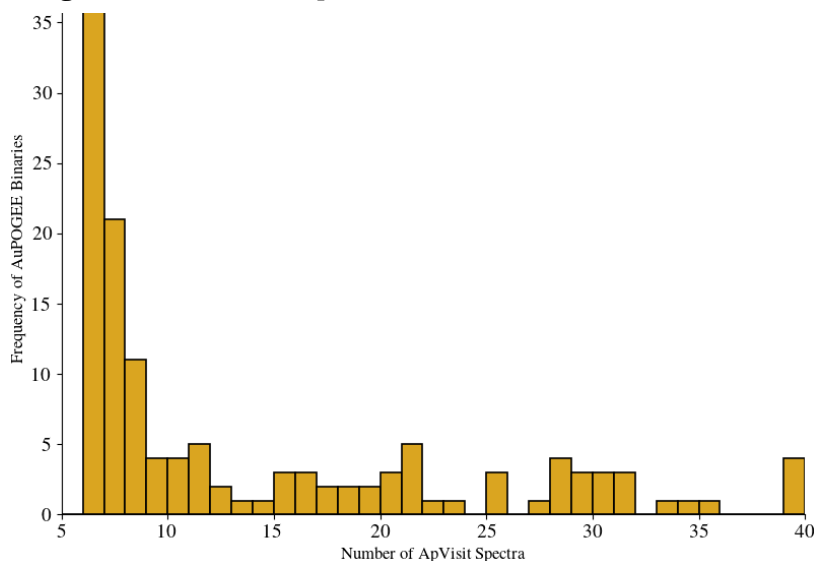


Figure 2.1: Histogram modeling the distribution of  $ApVisit$  observations for the *APOGEE* Gold sample (*AuPOGEE*). The majority of *AuPOGEE* binaries have under ten  $ApVisit$  spectra: in both cases of criteria (in the *APOGEE/Kepler* overlap and the *AuPOGEE/TESS* overlap)  $n_{ApVisits}$  was the most often disqualifying factor.

For all projects utilizing *APOGEE* spectroscopy, each  $ApVisit$  spectrum is continuum normalized and de-spiked to remove erroneous spectral features caused by telluric interference. This is done by identifying outliers in each spectrum above or below the continuum by 0.7 or 3 times the standard deviation of the normalized flux. The lower continuum factor is higher to avoid the unintentional removal of absorption lines from the spectrum. Additionally, around each identified outlier, a  $\pm 6 \text{ \AA}$  window is also flagged and removed. The python scripts used to retrieve, continuum normalize, and de-spike  $apVisit$  spectra in the *APOGEE/Kepler* overlap are publicly

available on GitHub<sup>2</sup>. They rely heavily on the apogee python package on GitHub described in Bovy (2016).

### 2.3.1 Radial Velocity Extraction: The Broadening Function and Cross Correlation Function

The Cross Correlation Function (CCF) is commonly used in the practice of extracting stellar radial velocities: in this approach a template spectrum and a series of `ApVisit` spectra are cross correlated, yielding the Radial Velocity (RV) of the target star relative to the template spectrum. CCF methodology works because of the convolution between two functions: that of the astrophysical target (including natural broadening effects) and the Broadening Function (BF) which is where important RV information is contained. While the CCF method is indeed very close to the convolution that occurs in an *APOGEE* spectrum the cross correlation between the template spectrum and an observed spectrum inherits natural broadening effects. These effects translate into peak-pulling and peak-pushing of the RV peaks which can cause the cancellation of important RV information.

Broadening Function methodology is formally presented in Rucinski (1992, 1999, 2002, 2004) and was used to extract primary and secondary RV components from all *APOGEE/Kepler* SEBs and some of the systems presented in §5. While the BF is inherently immune to natural broadening effects, it is sensitive to the presence of emission lines that are not found in the template spectra. Intuitively, BFRV extraction is only possible in SEB II systems, as the primary and secondary stellar components have their spectral signatures present in the observation. The main *APOGEE* data reduction pipeline lists RVs that are measured using the CCF methodology, and CCF RV estimates from *APOGEE* are used in §5 for systems not conducive to the BF RV extraction methodology.

Extracting BF from `ApVisit` spectra is completed using a modified version of the BF software suite from Rawls et al. (2016) which is based on the BF methodology of Rucinski (1992). To begin, a template stellar spectrum is selected from (Husser et al., 2013) to match the approximate spectrum parameters reported by *APOGEE*. As mentioned - *APOGEE* reports spectral parameters operating under the assumption that it is observing single stars. Therefore, these templates could not be a true match to the multiplicity system model; the match cannot be exact as the two stars in a binary may very well not have identical spectral type. Further, the model grid has a finite sampling of stellar parameters. Following Lu et al. (2001), we find that a mismatch in spectral type between the template and target translates to a change in the BF intensity, scale and quality. However, the RV estimates are derived from the amplitude of the primary and secondary RV components, which remain unchanged. BF peaks are first identified by eye and their appropriate locations on the RV axis are identified to fit Gaussians to each peak in the BF using a least-squares fitting procedure.

---

<sup>2</sup><https://github.com/mrawls/apVisitproc>

The location of each Gaussian’s mean is the RV estimate for that peak, which is then corrected with the barycentric velocity from it’s `ApVisit` spectrum. Errors in the extracted RV value are attributed to error in fitting a Gaussian to each BF peak using least-squares. Similar to what occurs in the *APOGEE* CCF pipeline, it is ultimately uncertainty in the measurement of the BF peak (which depends partially on the peak’s semi-arbitrary width) that determines the uncertainty in the RV extraction, causing a systematic underestimate.

Comparison between CCF RV extraction and BF RV extraction are shown in 3.1 and 3.2 for two of the SEBs in the *APOGEE/Kepler* overlap. 3.2 for KIC 6131659, illustrates that the BF does a superior job at resolving multiple velocity components than the CCF method does and additionally clearly identifies the system’s three-component nature, which was not visible in the CCF. These same comparisons are illustrated here (and also in §5) for a couple of cases within the *AuPOGEE/TESS* subset.

## 2.4 ANU 2.3-m Spectroscopy: The Wide Field Spectrograph (WiFeS)

In §4 (Clark Cunningham et al., 2020), spectroscopic observations were collected from the Wide Field Spectrograph (WiFeS) (Dopita et al., 2007) and echelle spectrograph on the Australian National University’s (ANU) 2.3 m telescope<sup>3</sup> at Siding Spring Observatory. WiFes in an image slicer integral field (IFU) spectrograph, in this approach the collected image is sliced in the image plane and re-arranged such that different parts of the image are allowed through a slit and a dispersing element. For our observations the B3000 grating and the RT560 dichroic were selected, resulting in spectral coverage of 3500 - 6000Å. After extracting and reducing the object spectra with IRAF<sup>4</sup> packages CCDPROC and KPNOSLIT. The wavelength was acquired from a Ne-Ar arc lamp exposure taken on the same observation date as the object spectra(Clark Cunningham et al., 2020). Exposures of standard spectrophotometric standard stars (Hamuy et al., 1994) are used to flux calibrate the spectrum’s flux following Bessell (1999). This reduced object spectrum (with  $S/N = 300/\text{resolution element}$ ) was fitted to a grid of synthetic spectra from Munari et al. (2005), weighing regions sensitive to to variations in surface gravity (following Penev et al. (2013) to derive atmospheric parameters for the EB HD 54236A (see §4.2.3 (Clark Cunningham et al., 2020)).

---

<sup>3</sup><http://rsaa.anu.edu.au/observatories/siding-spring-observatory>

<sup>4</sup>IRAF is distributed by the National Optical Astronomy Observatory, which is operated by the Association of Universities for Research in Astronomy (AURA) under cooperative agreement with the National Science Foundation.

## 2.5 SOuthern Astrophysical Research Telescope (SOAR): Goodman High Throughput Spectrograph

Installed on the f/16.6 Nasmyth platform of the 4.1 m SOuthern Astrophysical Research (SOAR) telescope in Cerro Pacho, Chile. These spectra were first trimmed to 6620–6750Å and normalized using a 7th-order spline function to the continuum to allow the measurement of the EW of the Li I 6708 Å resonance lines of the EB HD 54236A (See §4 (Clark Cunningham et al., 2019)).

In Chapter 3 (§3), I describe the full characterization a subset of SEB II's within the *APOGEE/Kepler*. This *APOGEE/Kepler* subset is explored in HR-diagram and stellar evolutionary space using age estimates derived from these well constrained stellar parameters. Age estimates of primary and secondary binary components allowed coevality tests on each of the SEB IIs, which test the underlying assumption in stellar formation theory that binary stars form at the same time, from the same intermolecular cloud.

In Chapter 4 (§4) I outline the analysis of the young eclipsing binary tertiary system in the constellation Puppis, HD 54236 (Clark Cunningham et al., 2020). By employing a variety of photometric observations in tandem with spectroscopy, we showed that the system was indeed a previously unknown EB with the wide, CPM tertiary (HD 54236B). Through the extraction of the system's stellar parameters, and the application of multiple stellar chronometers, we determine its estimated age and rate of coevality. Additionally, through the use of Gaia common kinematics combined with these solutions, we determine the ancestral stellar association membership of this system.

In Chapter 5 (§5) I summarize my most recent project exploring the overlap between *APOGEE* targets of known multiplicity (The Gold Sample Price-Whelan et al. (2020)) and *TESS* photometric observations. In this work, *APOGEE Gold Sample* identified binary systems are cross referenced through location (Right Ascension, Declination) with the *TESS* observed targets. *TESS* photometry was used to refine the reported *APOGEE* orbital periods, and in cases where the BF method of RV extraction was applicable, completed on each  $\text{ApVisit}$  spectrum. In the remainder of *Gold Sample/TESS* targets, where the BF methodology was not applicable, CCF RV values were acquired from the *TESS* pipeline.

Chapter 6 includes a discussion of the projects contained in this dissertation, a summary of knowledge gained, and potential future work using these methodologies.

## CHAPTER 3

### ***APOGEE/Kepler* Overlap Yields Orbital Solutions for a Variety of Eclipsing Binaries**

Abstract<sup>1</sup>

Spectroscopic eclipsing binaries (SEBs) are fundamental benchmarks in stellar astrophysics and today are observed in breathtaking detail by missions like the Transiting Exoplanet Survey Satellite (*TESS*), *Kepler*, and Apache Point Observatory Galactic Evolution Experiment (*APOGEE*). We develop a methodology for simultaneous analysis of high-precision *Kepler* light curves and high-resolution, near-infrared spectra from *APOGEE* and present orbital solutions and evolutionary histories for a subset of SEBs within this overlap. Radial velocities extracted from *APOGEE* spectra using the Broadening Function (BF) technique are combined with *Kepler* light curves and to yield binary orbital solutions. The BF approach yields more precise radial velocities than the standard cross-correlation function, which in turn yields more precise orbital parameters and enables the identification of tertiary stars. The orbital periods of these seven SEBs range from 4 to 40 days. Four of the systems (KIC 5285607, KIC 6864859, KIC 6778289, and KIC 4285087) are well-detached binaries. The remaining three systems have apparent tertiary companions, but each exhibit two eclipses along with at least one spectroscopically varying component (KIC 6449358, KIC 6131659, and KIC 6781535). *Gaia* distances are available for four targets which we use to estimate temperatures of both members of these SEBs. We explore evolutionary histories in *H-R* diagram space and estimate ages for this subset of our sample. Finally, we consider the implications for the formation pathways of close binary systems via interactions with tertiary companions. Our methodology combined with the era of big data and observation overlap opens up the possibility of discovering and analyzing large numbers of diverse SEBs, including those with high flux ratios and those in triple systems.

---

<sup>1</sup>Published 2019 August 12: The Astronomical Journal, Volume 158, Number 3, The American Astronomical Society

### 3.1 Introduction

The Apache Point Observatory Galactic Evolution Experiment (*APOGEE*) is studying our Galaxy in fantastic detail by providing high-resolution spectra for some 150,000 stars (Majewski et al., 2015). Some of these belong to double-lined spectroscopic eclipsing binaries (SEBs), and a further subset have been observed by the *Kepler* spacecraft (Borucki et al., 2010) and appear in the *Kepler* Eclipsing Binary Catalog (Kirk et al., 2016). These *APOGEE/Kepler* SEBs, which have several *APOGEE* spectra at different epochs, give a unique opportunity to combine the spectra with the *Kepler* light curve to model the binary orbit and directly measure fundamental stellar parameters, including mass and radius. They can then be used to explore and constrain stellar evolution, stellar populations, and orbital kinematics.

While much work has gone into exploring *Kepler* eclipsing binaries (EBs) as a population, fewer studies have maximally utilized complementary spectra to fully characterize these stellar systems. A notable exception is Matson et al. (2017), which found the radial velocities (RVs) of 40 *Kepler* binaries, 35 of them double-lined and the remainder single-lined. Their work used medium-resolution ground-based spectra, but the authors note that high-resolution spectra is more optimal. In another example, Torres et al. (2018) used *K2* light curves of the Ruprecht 147 cluster together with high resolution spectra and the cluster’s well-modeled metallicity to constrain the orbital parameters extracted from spectroscopic binary cluster members. In addition, Lehmann et al. (2012) analyzed the quadruple system KIC 4247791 by combining *Kepler* light curves and moderate resolution spectra.

Many studies have used *APOGEE* and *Kepler* data together, such as the APOKASC catalog (Pinsonneault et al., 2018, 2014), which combines *APOGEE* stellar parameters with *Kepler* asteroseismology. However, such works tend to ignore stellar multiplicity. The SEB overlap between *APOGEE* and *Kepler* in particular remains relatively unexplored. There is also synergy with the *Kepler* planet survey which identifies candidate planet systems, some of which are found to be eclipsing binaries, with or without tertiaries, with follow-up RV observations with *APOGEE* (Fleming et al., 2015). The frequency of binaries, with and without tertiary companions, is a necessary component of computing transiting exoplanet astrophysical false-alarm probabilities (e.g. Morton et al., 2016).

EBs have long been used as fundamental benchmarks for stellar astrophysics (e.g., Torres et al., 2015), including more recently as benchmarks for exoplanet properties (e.g., Stassun et al., 2017), to test asteroseismic inferences of stellar parameters (e.g., Gaulme et al., 2016), and even for assessing trigonometric parallaxes (Stassun et al., 2018). In addition, as they are often observed as SEBs, EBs are useful for assembling reliable statistics on the occurrence of higher order multiples (e.g., tertiary companions) and on the relationship of companion properties to the

properties of the EB. For example, Tokovinin (1997) found the incidence of wide tertiaries to be strongly linked to the orbital period of the inner binary. Additional well-studied EBs can help to further test these relationships.

In this work, we identify 33 promising *APOGEE/Kepler* SEBs and compute full orbital solutions with a suite of stellar parameters for seven of them. In section 3.2.1, we detail our sample selection, data processing, and modeling methodology. We further show how the broadening function (BF) technique is a superior method to extract multiple velocity components from *APOGEE* spectra. Subsequently section 3.3 discusses each of the seven modeled systems in turn and presents orbital solutions. Finally, section 3.4.1 places the SEBs in the context of each star’s stellar evolutionary history and explores the relationship of the EB orbital properties to the presence of tertiary companions.

## 3.2 Data and Methods

### 3.2.1 Sample Selection

We use the following criteria and filters to arrive at a candidate sample of promising SEBs in the *APOGEE/Kepler* overlap. We begin with the *Kepler* EB catalog compiled by Kirk et al. (2016). From this catalog we select targets that have both their primary and secondary eclipses observed by *Kepler*; this limits our selection to binaries with inclinations close to  $90^\circ$ . We further require the light curve to be semi- or well-detached, with the morphology parameter significantly less than 1. Next, a luminosity limit of  $H < 14$  magnitudes was imposed, as fainter targets are unlikely to have *H*-band *APOGEE* spectra with a sufficiently high signal-to-noise ratio (S/N). We also require the targets to have multiple cross-correlation function (CCF) peaks from the *APOGEE* pipeline (Nidever et al., 2015) visible by eye in one epoch. Finally, the binaries must have been observed by *APOGEE* at least three times, and thus have at least three `apVisit` spectra, with no quality flags present.

Taken together, these criteria result in 33 candidates, which are listed in Table 1, plus one additional candidate that has already been analyzed (Rawls et al., 2016). Of these, we perform a detailed analysis of seven. The notes in Table 1 indicate why we choose to exclude the other systems at this time. Several are being investigated by the *Kepler APOGEE* EB Working Group, some have only three *APOGEE* visits, which would make a good RV curve solution challenging without additional spectra, some have low S/N ratios, one shows significant ellipsoidal variations, which are not included in our photometric model, and two remain good candidates for future analyses.



Table 3.1: Promising SEBs Observed by *APOGEE* and *Kepler*, Sorted by *Kepler* Magnitude ( $K_p$ ).

KIC	APOGEE ID	Visits	$K_p$	$P_{orb}$ (day)	SE Depth (frac)	Morphology	Reference	Notes
9246715	2M20034832+4536148	2	10.08	171.28	0.1124	0.11	Rawls et al. (2016)	
2708156	2M19302686+4318185	3	10.67	1.89	0.0625	0.57		Only three visits
3120320	2M19291007+3817041	3	11.28	10.27	0.0127	0.14		Kepler APOGEE/EB WG
4851217	2M19432016+3957081	6	11.32	2.47	0.1815	0.58		Low S/N ratio
3439031	2M19203184+3830492	3	11.50	5.95	0.4156	0.33		Kepler APOGEE/EB WG
5285607	2M19390532+4027346	6	11.69	3.90	0.0403	0.36	This work	
6449358	2M19353513+4149543	25	11.72	5.78	0.0120	0.31	This work	
10206340	2M19245882+4714573	3	11.78	4.56	0.2431	0.61		Only three visits
6864859	2M19292405+4223363	25	11.93	40.88	0.2426	0.06	This work	
4931073	2M19351913+4001522	6	12.18	26.95	0.0564	0.08		Kepler APOGEE/EB WG
3127817	2M19355993+3813561	6	12.24	4.33	0.0512	0.48		Kepler APOGEE/EB WG
3335816	2M19184759+3824238	3	12.40	7.42	0.0106	0.16		Kepler APOGEE/EB WG
5284133	2M19373173+4027078	6	12.50	8.78	0.0492	0.15		Future work
3542573	2M19232622+3838017	3	12.61	6.94	0.0837	0.25		Only three visits
2711114	2M19240341+3758109	3	12.63	2.86	0.0022	0.29		Only three visits
4281895	2M19441242+3923418	6	12.76	9.54	0.0652	0.13		Only three visits
4660997	2M19340328+3942410	6	12.78	0.56	0.2527	0.62		Ellipsoidal variations
4473933	2M19363898+3933105	6	12.87	103.59	0.0126	0.25		Low S/N ratio
2305543	2M19280644+3736023	3	12.97	1.36	0.1052	0.50		Only three visits
3241619	2M19322278+3821405	3	13.06	1.70	0.1625	0.44		Only three visits
4285087	2M19463571+3919069	6	13.19	4.49	0.2408	0.31	This work	
2576692	2M19263432+3748513	3	13.19	87.88	0.2588	0.04		Kepler APOGEE/EB WG
6131659	2M19370697+4126128	27	13.20	17.53	0.1036	0.09	This work	
4847832	2M19401839+3957298	6	13.20	30.96	0.3200	0.08		Kepler APOGEE/EB WG
5025294	2M19414825+4010323	6	13.27	5.46	0.0010	0.18		Future work
6778289	2M19282456+4215080	25	13.31	30.13	0.1619	0.11	This work	
3248332	2M19383951+3819588	6	13.37	7.36	0.0974	0.20		Kepler APOGEE/EB WG
6610219	2M19320615+4200049	25	13.58	11.30	0.2899	0.20		Low S/N ratio
6781535	2M19321788+4216489	25	14.14	9.12	0.0305	0.12	This work	
4077442	2M19452193+3908260	6	14.35	0.69	0.0703	0.59		Kepler APOGEE/EB WG
3247294	2M19374558+3822510	6	14.35	67.42	0.1032	0.02		Kepler APOGEE/EB WG
3848919	2M19241352+3858278	3	14.48	1.05	0.3418	0.57		Low S/N ratio
5460835	2M19411125+4039416	6	14.72	21.54	0.0228	0.06		Low S/N ratio
4075064	2M19432862+3908535	6	15.71	61.42	0.0821	0.00		Low S/N ratio

### 3.2.2 RVs from APOGEE Spectra

The standard observing mode for *APOGEE* spectra has a total exposure time of roughly three hours, which is usually collected over a series of visits on different days. The visits are then combined into one spectrum per target (an `apStar` spectrum). We instead utilize individual visit spectra (`apVisit`), which are identified with their plate ID, date (MJD), and fiber ID. These may be retrieved from the SDSS Science Archive Server search tool with a simple search by *APOGEE* ID.

We continuum normalize the visit spectra and then de-spike them to remove erroneous spectral features due to tellurics. De-spiking consists of identifying outliers above or below the continuum by 0.7 or 3 times the standard deviation of the normalized flux, respectively. The below continuum factor is larger to avoid unintentionally removing real absorption line features. Around each outlier spike, a  $\pm 6 \text{ \AA}$  window is also flagged for removal. The python scripts used to retrieve, continuum normalize, and de-spike `apVisit` spectra are publicly available on GitHub<sup>2</sup>. They rely heavily on the *apogee* python package on GitHub described in Bovy (2016).

In the main *APOGEE* reduction pipeline (Nidever et al., 2015), RVs are measured using the CCF. In this approach, a template spectrum and a series of visit spectra for a given target are cross-correlated, giving the RV of the target star relative to the template.

The CCF method works because an observed stellar spectrum can be represented as a convolution of two functions: that of the astrophysical target (which includes natural broadening components such as thermal broadening, microturbulence effects, and instrumental broadening) and another function called the BF that contains the important RV information. The BF is formally presented in Rucinski (1992, 1999, 2002, 2004). Although the CCF method is very close to the real convolution that occurs in an *APOGEE* spectrum, cross-correlating a template spectrum with an observed stellar spectrum yields a function that inherits the natural broadening components present in both spectra. In this way the CCF is essentially a nonlinear proxy of the BF. Therefore, instead of using the CCF, in this work we measure the BF directly.

To extract BFs from our target spectra, we use a modified version of the BF software suite from Rawls et al. (2016) which is based on the method introduced by Rucinski (1992). A PHOENIX BT-Settl model atmosphere spectrum (Husser et al., 2013) is selected to match the target’s approximate spectral parameters as reported by APOGEE. The match cannot be exact as the two stars in a binary may not have identical spectral types and the model grid has a finite sampling in stellar parameters. In general, a mismatch in spectral type between the template and the target causes the BF to change in its intensity scale and quality, but the amplitudes of the RV components remain unchanged (Lu et al., 2001).

---

<sup>2</sup><https://github.com/mrawls/apVisitproc>

We examine the BF peaks by eye to identify their approximate locations on the RV axis and use a least-squares fitting procedure to fit one or more Gaussians to the BF. The location of each Gaussian’s mean is the RV, which we then correct with the barycentric velocity provided with each `apVisit` spectrum. Our reported RV uncertainties come from the error in fitting a Gaussian to each BF peak using least-squares. Much like in the *APOGEE* CCF pipeline (Nidever et al., 2015), it is ultimately the uncertainty in the measurement of the BF peak, which depends partially on its semi-arbitrary width, that determines the reported uncertainties for the RVs. This systematically underestimates the uncertainty of each RV measurement. The software used to extract RVs as described here is publicly available on GitHub.

In Figures 3.1 and 3.2, we demonstrate how the BF method produces significantly better separated peaks for *APOGEE* double-lined SEBs than the CCFs generated by the *APOGEE* pipeline. Due in part to the BF method having less of a peak-pulling effect, this more defined separation dramatically improves our ability to measure the RV of each component. We present the BF and measured RVs for each of our seven targets in the Appendix 3.7.

We also measure flux ratios in the *APOGEE* *H* band with our BF peaks, as the ratio of the peak areas is directly proportional to the flux ratio of the binary (Bayless & Orosz, 2006; Stassun et al., 2007). These BF flux ratios will generally differ from *Kepler*-derived flux ratios because of the difference in wavelength; *APOGEE* is an *H*-band spectrograph and *Kepler* has a broad visible light bandpass. The BF flux ratios are discussed further in Section 3.3.8 alongside other variables for RV extraction and temperature estimation.

### 3.2.3 *Kepler* Light Curve Processing

We use minimally processed *Kepler* long-cadence simple aperture photometry (SAP) to construct EB light curves for each target. Each light curve, and their uncertainties, are normalized by the median raw flux value of all available quarters. We de-weight data of poor quality by selecting times with *Kepler* quality flags  $> 0$ , and inflating the normalized flux uncertainties at these times by a factor of 10.

### 3.2.4 Orbital and Mass Solutions with **KEBLAT**

With RVs in hand, we turn to the photometric modeling of the *Kepler* light curves. We utilize a modular Python tool dubbed **KEBLAT** which is capable of separate or simultaneous modeling of the binary light curve, spectral energy distribution, and RV time series (Windemuth et al., 2018). Here, we simultaneously model *Kepler* light curves and *APOGEE* RVs of each EB in our sample to determine orbital solutions ( $P, e, \omega, i, t_{PE}$ ), stellar parameters ( $m_1, m_2, r_1, r_2, \frac{F_2}{F_1}$ ), quadratic limb-darkening coefficients under triangular reparameterization ( $q_{1,1}, q_{1,2}, q_{2,1}, q_{2,2}$ ;

**Figure 5.1** BF, CCF Velocity Component Resolution Comparison for KIC 6864859

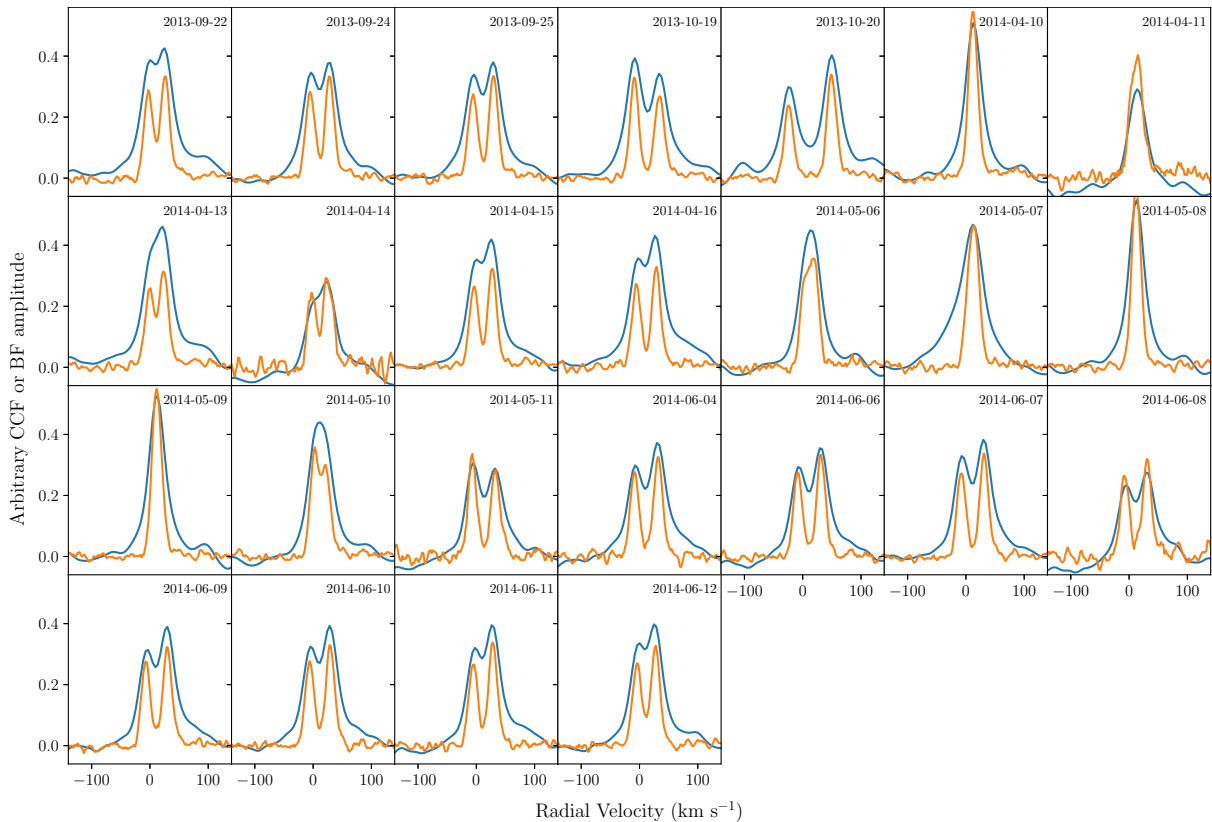


Figure 3.1: The BF (orange) is significantly better at resolving multiple velocity components from *APOGEE* visit spectra than the CCF (blue). This example shows visits for KIC 6864859. The y-axis amplitude is arbitrarily scaled for clarity. While it is clear from most of the CCFs that KIC 6864859 is a double-lined SEB, the BF more clearly separates the contribution from each star.

Kipping 2013), and systemic RV  $k_0$ . For parameter sampling purposes, we transform individual mass and radius parameters to sums and ratios, and parameterize  $e$  and  $\omega$  as  $e \cos \omega$  and  $e \sin \omega$ . Given a system’s total mass, period, eccentricity, argument of periastron, inclination, and time of primary eclipse, *KEBLAT* uses a Keplerian solver to compute the instantaneous positions and velocities of each stellar component. The positions, along with specified sizes and relative flux of the stars, are then used to determine the instantaneous light contribution during eclipse via a quadratic limb-darkening (Mandel & Agol, 2002) model for spherical bodies.<sup>3</sup> We account for finite sampling effects (Kipping, 2010) on the light curve by down-sampling one-minute eclipse profiles to the *Kepler* long cadence ( $dt = 0.0204$  day). Stellar and instrumental noise is marginalized by fitting the lowest non linear order quadratic polynomial around each eclipse. We apply quarterly crowding values from *Kepler* to model third light contamination. To account for underestimated observational uncertainties and additional noise, we fit for a systematic light curve

<sup>3</sup>The assumption of spherical stars requires that the stars be sufficiently detached to avoid tidal and rotational distortions.

**Figure 5.2** BF, CCF Velocity Component Resolution Comparison for KIC 6131659

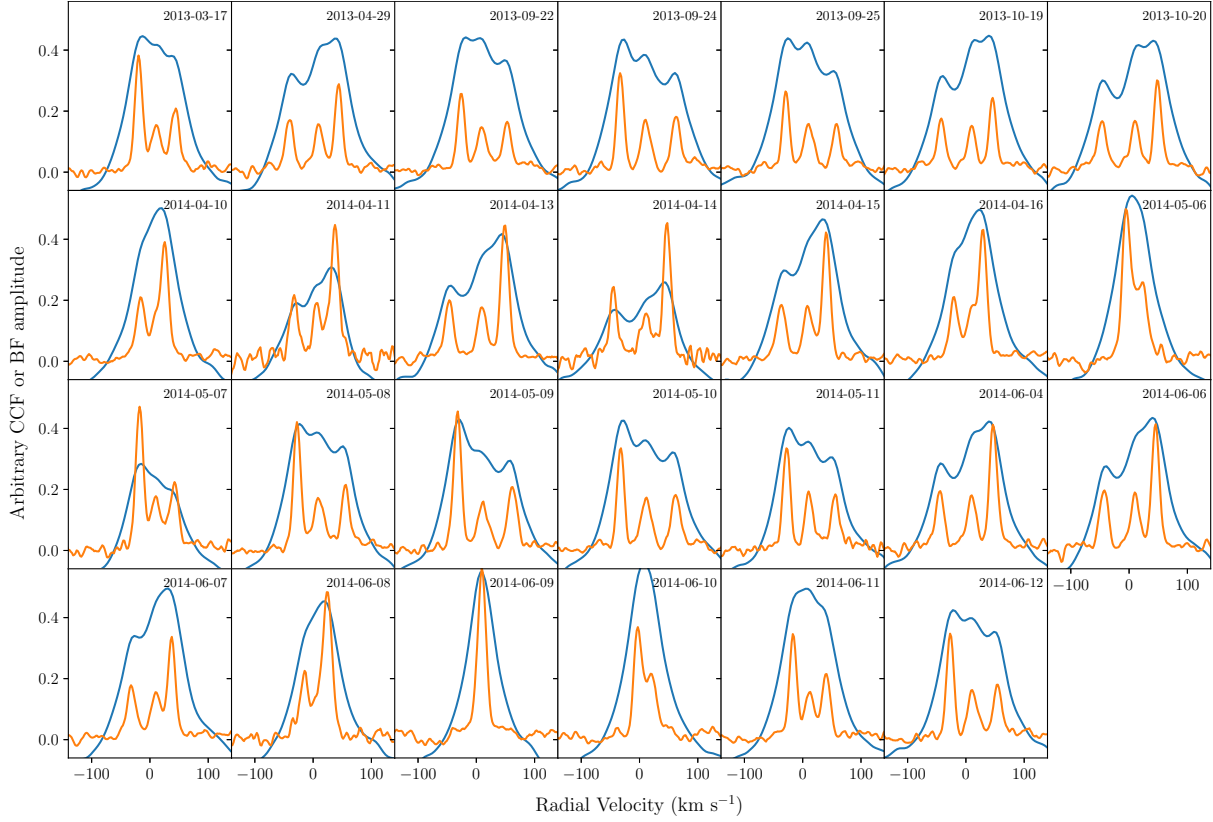


Figure 3.2: A second example, as in Figure 3.1, showing that the BF (orange) does a better job of resolving multiple velocity components than the CCF (blue). The y-axis amplitude is arbitrarily scaled for clarity. While it is clear from some of the CCFs that KIC 6131659 has more than one component, the three-component nature is immediately obvious in the BF.

error  $\sigma_{\text{sys,LC}}$ , which we add in quadrature to the observed errors.

The  $z$ -component of the velocity, as solved by *Kepler's* equation, is used to model the extracted RVs. For double-line eclipsing binary systems, where the RVs of both components are detected, the amplitudes of the primary and secondary RV are related to the masses of the secondary and primary, respectively. For single-line EBs, where only the RV of the brightest component is detected, only the mass function  $f_M$  of the system can be constrained, where

$$f_M = \frac{M_2^3 \sin^3 i}{(M_1 + M_2)^2}. \quad (3.1)$$

As with the light curve data, we fit for a systematic RV error parameter  $\sigma_{\text{sys,RV}}$  to account for underestimated noise.

We combine RVs with *Kepler* light curve information to model the system and find a best-fit solution. We first determine the light curve and RV solutions separately, and then fit the RV and

light curve simultaneously. The simultaneous RV+LC model has 17 free parameters in total. The model is optimized via a least-squares algorithm `lmfit` (Newville et al., 2016), and then uses the best-fit solution to seed Monte Carlo Markov Chain (MCMC) simulations with `emcee` (Foreman-Mackey et al., 2013), in order to sample the posterior distributions of each parameter. We use broad, uniform priors and run the Markov chains with 128 walkers for  $\sim 100,000$  iterations, visually inspecting trace plots for convergence. We report the 50%, 16%, and 86% values, i.e., the mean and  $1\sigma$  uncertainties for each parameter. For more details on the `KEBLAT` model, including parameter bounds, see Windemuth et al. (2018).

### 3.2.5 Radius ratio - flux ratio - inclination Degeneracy

For light curves with partially or grazing eclipsing geometries, there exists a degeneracy between radius ratio and flux ratio when eclipses are observed in a single photometric band. For this reason, we use additional constraints on the *Kepler* light curve flux ratios with spectroscopic *H*-band flux ratios obtained from the BF for SEBs exhibiting shallow eclipses (KIC 5285607 and KIC 6781535). For these two systems, we place a Gaussian prior on the RV+LC solution  $I$  with  $\mu$  centered around the BF-derived flux ratio and  $\sigma = 0.2$ .

### 3.2.6 Temperatures from Flux Ratios and Radii

Obtaining effective temperatures of the stars in these SEBs requires additional analysis. The `KEBLAT` model does not provide a measurement of stellar temperatures directly, but only indirectly via the flux ratio in the *Kepler* bandpass. In addition, the *APOGEE* Stellar Parameter and Chemical Abundances Pipeline (ASPCAP) processing reports only a single combined light effective temperature for each system (Pérez et al., 2016). This ASPCAP temperature is likely to be biased due to the contamination of the brighter star’s spectrum by the fainter star. Here we address both of these issues to estimate individual stellar effective temperatures.

The orbital solutions described in section 3.2.4 yield sums and ratios of radii. In addition, the light curve analyses yield flux ratios ( $F_{\text{ratio}} \equiv \frac{F_2}{F_1}$ ) in the *Kepler* bandpass that are primarily constrained by the observed eclipse depths. By assuming that ASPCAP effective temperature is the flux-weighted average of the system,  $T_{\text{avg}} = (F_1 T_1 + F_2 T_2) / (F_1 + F_2)$ , and defining the primary star as the one that provides the majority of the light, we can use the following relationships between the flux ratio  $F_{\text{ratio}}$ ,  $T_{\text{avg}}$ , stellar radii  $R_1$  and  $R_2$ , and distance  $d$  to find flux and temperature estimates for the individual binary components separately. First, we solve for the binary’s flux sum using *Gaia* distance estimates from Bailer-Jones et al. (2018):

$$F_{\text{sum}} = \frac{\sigma T_{\text{avg}}^4 (R_1^2 + R_2^2)}{d^2}, \quad (3.2)$$

from which we can compute the individual fluxes as

$$F_1 = \frac{F_{\text{sum}}}{1 + F_{\text{ratio}}} \quad (3.3)$$

and

$$F_2 = F_{\text{sum}} - F_1. \quad (3.4)$$

Then, we use the relationship between  $T_{\text{ave}}$ ,  $F_{\text{ratio}}$ , and the individual stellar fluxes to solve for the temperature of each star:

$$T_{\text{avg}} = T_2 \frac{F_{\text{ratio}}^{-1} T_{\text{ratio}}^{-1} + 1}{F_{\text{ratio}}^{-1} + 1}, \quad (3.5)$$

which yields

$$T_1 = \sqrt[4]{\frac{F_1 d^2}{\sigma R_1^2}} \quad (3.6)$$

and

$$T_2 = \sqrt[4]{\frac{F_2 d^2}{\sigma R_2^2}}. \quad (3.7)$$

However, these resulting temperature estimates are likely systematically underestimated. In the ASPCAP pipeline, *APOGEE* spectra are compared to a synthetic spectral model to resolve quantities like effective temperature. When a detached binary signature is present in stellar spectra, the additional component can cause the spectrum to be fit by a cooler synthetic template. This leads to a systematic underestimation in the binaries' effective temperatures of roughly 300 K (El-Badry et al., 2017). The systematic underestimation is a function of the effective temperature of the primary and the mass ratio of the system. We follow their method for each system to correct for this effect.

### 3.3 Results

The joint light curve and RV analysis for each of the seven systems is presented in detail in the following subsections. We present the orbital and mass solutions together in 3.3.

In all systems, we define the primary eclipse ( $\phi = 0$ ) as the deeper eclipse. This corresponds to when the primary star is eclipsed by the secondary star. Usually, the primary star is the brighter of the two, and the light curve definition of primary and the RV definition of primary agree. However, we note the secondary star in KIC 6781535 is brighter in the *APOGEE* *H*-band than the primary. In the figures that follow, we color code the RV of the primary star in red and the RV of the secondary star in orange.

Table 3.2: Binary Orbital and Stellar Parameters

	KIC 5285607	KIC 6864859	KIC 6778289	KIC 6449358	KIC 4285087	KIC 6131659	KIC 6781535 <sup>a</sup>
$f_M^b$	...	...	...	$0.126^{+0.002}_{-0.002}$	...	...	...
$M_1 (M_\odot)$	$1.557^{+0.038}_{-0.035}$	$1.411^{+0.028}_{-0.028}$	$1.512^{+0.022}_{-0.022}$	...	$1.135^{+0.013}_{-0.014}$	$0.942^{+0.010}_{-0.010}$	$1.003^{+0.039}_{-0.038}$
$M_2 (M_\odot)$	$1.346^{+0.033}_{-0.033}$	$1.354^{+0.028}_{-0.028}$	$1.092^{+0.019}_{-0.018}$	...	$1.101^{+0.013}_{-0.014}$	$0.703^{+0.008}_{-0.008}$	$1.034^{+0.040}_{-0.040}$
$R_1 (R_\odot)$	$2.003^{+0.062}_{-0.054}$	$1.655^{+0.012}_{-0.013}$	$1.748^{+0.009}_{-0.009}$	$2.1254^{+0.0007}_{-0.0006}$	$1.033^{+0.010}_{-0.012}$	$0.908^{+0.003}_{-0.003}$	$1.199^{+0.113}_{-0.065}$
$R_2 (R_\odot)$	$1.679^{+0.063}_{-0.087}$	$1.455^{+0.012}_{-0.012}$	$0.998^{+0.005}_{-0.005}$	$0.6977^{+0.0005}_{-0.0004}$	$1.026^{+0.011}_{-0.011}$	$0.616^{+0.003}_{-0.003}$	$1.434^{+0.066}_{-0.114}$
$P_{\text{orb}} (\text{day})$	$3.89940111^{+4.4e-8}_{-4.5e-8}$	$40.8778425^{+2.9e-7}_{-3.0e-7}$	$30.1301385^{+3.5e-7}_{-3.5e-7}$	$5.77679431^{+5.0e-8}_{-4.9e-8}$	$4.48603142^{+5.1e-8}_{-5.4e-8}$	$17.52782741^{+2.2e-7}_{-2.3e-7}$	$9.12208640^{+2.5e-7}_{-2.4e-7}$
$t_{pe} (\text{day})^c$	$126.577647^{+1.1e-5}_{-9.7e-6}$	$158.3189733^{+9.2e-6}_{-7.6e-6}$	$122.100819^{+1.0e-5}_{-1.0e-5}$	$122.0739252^{+7.1e-6}_{-7.2e-6}$	$133.450881^{+1.1e-5}_{-1.1e-5}$	$127.042190^{+1.1e-5}_{-1.1e-5}$	$138.838193^{+4.8e-5}_{-6.6e-5}$
$i (\text{rad})$	$1.3656^{+0.0015}_{-0.0009}$	$1.5415^{+0.0001}_{-0.0001}$	$1.55876^{+0.00001}_{-0.00001}$	$1.5327^{+0.0001}_{-0.0001}$	$1.5210^{+0.0001}_{-0.0001}$	$1.5558^{+0.0001}_{-0.0001}$	$1.4749^{+0.0007}_{-0.0004}$
$e \sin \omega$	$1.3e-6^{+9.0e-4}_{-1.2e-4}$	$-0.0254^{+0.0006}_{-0.0005}$	$-0.2337^{+0.0004}_{-0.0004}$	$0.00060^{+0.00046}_{-0.00040}$	$1.8e-4^{+1.4e-3}_{-3.0e-4}$	$-0.0127^{+0.0004}_{-0.0005}$	$0.0215^{+0.0034}_{-0.0026}$
$e \cos \omega$	$-8.6e-7^{+3.5e-6}_{-4.1e-6}$	$-0.634115^{+0.00001}_{-0.00001}$	$0.051090^{+0.000005}_{-0.000005}$	$-0.00023^{+1.0e-5}_{-1.1e-5}$	$-5.9e-5^{+3.7e-6}_{-3.8e-6}$	$7.1e-5^{+1.7e-6}_{-1.8e-6}$	$0.25005^{+0.00001}_{-0.00001}$
$F_2/F_1$	$0.6579^{+0.0959}_{-0.1025}$	$0.7256^{+0.0139}_{-0.0124}$	$0.19155^{+0.00002}_{-0.00002}$	$0.010752^{+6.5e-6}_{-6.5e-6}$	$0.9455^{+0.0396}_{-0.0356}$	$0.1480^{+0.0010}_{-0.0010}$	$1.0654^{+0.2195}_{-0.2384}$
$q_{1,1}$	$0.3690^{+0.0158}_{-0.0157}$	$0.4313^{+0.0158}_{-0.0176}$	$0.2930^{+0.0146}_{-0.0146}$	$0.3570^{+0.0082}_{-0.0099}$	$0.4632^{+0.0369}_{-0.0413}$	$0.1961^{+0.0042}_{-0.0039}$	$0.3786^{+0.0389}_{-0.0366}$
$q_{1,2}$	$0.0335^{+0.0407}_{-0.0242}$	$0.1113^{+0.0121}_{-0.0112}$	$0.3112^{+0.0179}_{-0.0169}$	$0.2961^{+0.0085}_{-0.0068}$	$0.3046^{+0.0518}_{-0.0460}$	$0.9959^{+0.0031}_{-0.0068}$	$0.7549^{+0.0938}_{-0.1037}$
$q_{2,1}$	$0.4027^{+0.0249}_{-0.0710}$	$0.3662^{+0.0269}_{-0.0259}$	$0.3991^{+0.0265}_{-0.0260}$	$0.3436^{+0.1530}_{-0.1270}$	$0.5470^{+0.0680}_{-0.0509}$	$0.0424^{+0.0076}_{-0.0070}$	$4056^{+0.0711}_{-0.0553}$
$q_{2,2}$	$0.0905^{+0.1343}_{-0.0579}$	$0.2377^{+0.0226}_{-0.0213}$	$0.3220^{+0.0329}_{-0.0306}$	$0.3189^{+0.3426}_{-0.2208}$	$0.2275^{+0.0427}_{-0.0381}$	$0.9380^{+0.0459}_{-0.0923}$	$0.2689^{+0.2181}_{-0.1750}$
$M_1 + M_2 (M_\odot)$	$2.903^{+0.068}_{-0.064}$	$2.765^{+0.052}_{-0.052}$	$2.604^{+0.038}_{-0.038}$	...	$2.236^{+0.025}_{-0.026}$	$1.645^{+0.017}_{-0.017}$	$2.040^{+0.073}_{-0.074}$
$M_2/M_1$	$0.863^{+0.014}_{-0.013}$	$0.960^{+0.015}_{-0.015}$	$0.723^{+0.009}_{-0.009}$	...	$0.969^{+0.007}_{-0.008}$	$0.746^{+0.005}_{-0.005}$	$1.030^{+0.026}_{-0.025}$
$R_1 + R_2 (R_\odot)$	$3.679^{+0.031}_{-0.033}$	$3.110^{+0.019}_{-0.020}$	$2.746^{+0.013}_{-0.013}$	$2.8231^{+0.0010}_{-0.0009}$	$2.060^{+0.008}_{-0.008}$	$1.525^{+0.005}_{-0.005}$	$2.632^{+0.034}_{-0.033}$
$R_2/R_1$	$0.839^{+0.055}_{-0.067}$	$0.879^{+0.008}_{-0.007}$	$0.5708^{+0.0003}_{-0.0003}$	$0.3283^{+0.0002}_{-0.0002}$	$0.993^{+0.020}_{-0.018}$	$0.679^{+0.003}_{-0.003}$	$1.222^{+0.113}_{-0.153}$
$b^d$	$1.5146^{+0.0473}_{-0.0576}$	$1.2407^{+0.0081}_{-0.0075}$	$0.3860^{+0.0005}_{-0.0005}$	$0.3413^{+0.0009}_{-0.0008}$	$0.7215^{+0.0079}_{-0.0076}$	$0.5533^{+0.0041}_{-0.0042}$	$1.9034^{+0.0960}_{-0.1341}$
$e$	$6.7e-5^{+9.6e-4}_{-6.2e-5}$	$0.63462^{+0.00001}_{-0.00001}$	$0.2392^{+0.0004}_{-0.0004}$	$0.00064^{+0.00045}_{-0.00033}$	$3.4e-4^{+1.3e-3}_{-2.6e-4}$	$0.0127^{+0.0005}_{-0.0004}$	$0.2510^{+0.0005}_{-0.0002}$
$\ln(\sigma_{\text{LC, sys}})$	$-8.76^{+0.01}_{-0.01}$	$-8.84^{+0.01}_{-0.01}$	$-8.48^{+0.01}_{-0.01}$	$-8.419^{+0.006}_{-0.006}$	$-6.81^{+0.01}_{-0.01}$	$-7.54^{+0.01}_{-0.01}$	$-8.12^{+0.01}_{-0.01}$
$k_0 (\text{m s}^{-1})$	$61668.8^{+532.1}_{-488.9}$	$93945.5^{+139.6}_{-142.6}$	$72332.2^{+213.8}_{-212.4}$	$68694.7^{+144.0}_{-147.0}$	$91275.4^{+248.5}_{-256.1}$	$89867.7^{+127.1}_{-125.2}$	$44547.4^{+633.7}_{-627.5}$
$\ln(\sigma_{\text{RV, sys}} (\text{m s}^{-1}))$	$7.40^{+0.26}_{-0.23}$	$6.54^{+0.14}_{-0.13}$	$7.04^{+0.12}_{-0.11}$	$6.27^{+0.23}_{-0.20}$	$6.65^{+0.29}_{-0.23}$	$6.82^{+0.10}_{-0.10}$	$8.28^{+0.12}_{-0.11}$

<sup>a</sup> Broad Gaussian prior on the flux ratio used based on the BF results ( $\sigma = 20\%$  BF value).<sup>b</sup>  $f_M$  is the mass function as defined in §3.2.4; instead of fitting directly for  $M_1$  and  $M_2$ , we used  $f_M$  for KIC 6449358 because it is a single-lined spectroscopic binary.<sup>c</sup> The fit zero-point for the time of primary eclipse is in units of BKJD (BJD - 2,454,833). The primary eclipse is defined here as the deeper of the two. This differs from the KEBC (Kirk et al., 2016) primary eclipse definition for KIC 6864859 only because the two eclipses have very similar depths.<sup>d</sup> The impact parameter  $b$  is defined as  $a \cos i / R_1$ , where  $q_1^1, q_2^1$  and  $q_1^2, q_2^2$  are triangularized quadratic limb-darkening coefficients for star 1 and star 2 (see Section 3.2.4 for details). We use natural log for the systematic light curve and RV error terms for fitting flexibility.



### 3.3.1 KIC 5285607

KIC 5285607 is a grazing ( $i = 79^\circ$ ) 3.9 day eclipsing binary with similar mass stellar components ( $M_1 = 1.56 M_\odot$ ,  $M_2 = 1.35 M_\odot$ ). The stars are in a circular orbit, as exhibited by the sinusoidal shape of the RV and occurrence of secondary eclipse at a phase of  $\sim 0.5$  as seen in Figure 3.3.

Because the eclipses in the light curves are shallow (4% loss of light), the impact parameter is highly degenerate with the flux and radius ratio. That is, a solution with similar flux contributions from both components in a more inclined system yields the same shallow eclipses as a solution with a much brighter primary component in a more edge-on system. This degeneracy can be ameliorated with additional information from spectra. Therefore, we place a Gaussian prior on the flux ratio parameter based on the BF fits, with a  $0.2 \ 1\sigma$  width. With this flux ratio constraint, we find that the secondary star is about 80% the size of the primary, with absolute dimensions of  $2.0 R_\odot$  and  $1.7 R_\odot$  for the primary and secondary components, respectively.

### 3.3.2 KIC 6864859

KIC 6864859 is a highly eccentric ( $e \sim 0.6$ ), slightly inclined ( $i = 88^\circ.32$ ) 40.9 day eclipsing binary with components of similar mass ( $M_1 = 1.41 M_\odot$ ,  $M_2 = 1.35 M_\odot$ ) and radii ( $R_1 = 1.66 R_\odot$ ,  $R_2 = 1.46 R_\odot$ ). The best-fit model is shown in Figure 3.4. The system's highly eccentric orbit gives rise to irregularly shaped RVs and a secondary eclipse near phase  $\sim 0.125$ . Figure 3.5 shows clear brightening events of the system between the primary and secondary eclipses, with maximal amplitudes of  $\sim 0.3$  ppt at phase  $\sim 0.065$ , the predicted phase of periastron passage from KEBLAT. This behavior is consistent with tidal distortions in an eccentric orbit near periastron, and is symptomatic of a class of objects known as heartbeat stars (Thompson et al., 2012). Both primary and secondary eclipse residuals exhibit small amplitude ( $\sim 0.5$  ppt) coherent structures; these are likely due to the nonspherical shape of the stars which is not explicitly modeled in KEBLAT.

We note that in our reduction process, some `apVisit` spectra were eliminated due to a very low signal-to-noise ratio that persisted after being run through our de-spike program. The majority of the remaining visits for this target resulted in well-separated peaks from the BF.

### 3.3.3 KIC 6778289

KIC 6778289 is a 30.1 day eclipsing binary with stellar components  $M_1 = 1.51 M_\odot$  and  $M_2 = 1.09 M_\odot$  in an eccentric ( $e = 0.2$ ), nearly edge-on ( $i = 89^\circ.3$ ) orbit. The simultaneous RV+LC fit is shown in Figure 3.6. The radii are  $R_1 = 1.75 R_\odot$  and  $R_2 = 1.0 R_\odot$ . This difference in radius gives rise to the difference in primary and secondary eclipse shape. The flat-bottom secondary eclipse indicates a total eclipse of the secondary component, while the primary eclipse is more V-shaped, e.g., more grazing. The larger residuals during the secondary eclipse is consistent with starspot modulation. The system has low ( $\approx 1\%$ ) third light contamination in the *Kepler* light curve which does not appear in the BF.

**Figure 5.3** Best-fit Joint LC+RV Solution for KIC 5285607

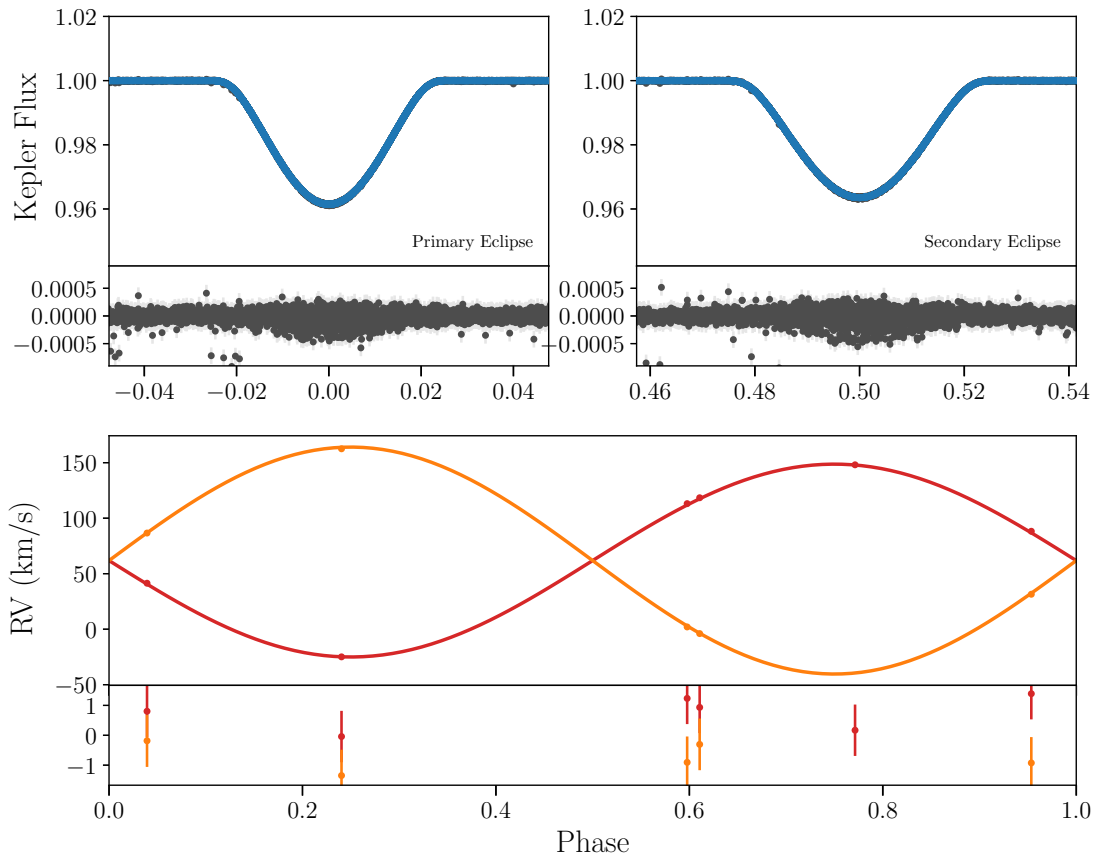


Figure 3.3: Simultaneous light curve (top panels) and RV (bottom panel) fits to *Kepler* and *APOGEE* observations for KIC 5285607. The light curve data and residuals are shown in dark gray, with the model overlaid in blue. Note the shallow and V-shaped primary and secondary eclipses, which indicate a grazing system. The phased RV panel shows the BF-derived values (points) and corresponding model (lines), where the primary RV is red and secondary RV is orange. The RV semi-amplitude is  $\sim 100 \text{ km s}^{-1}$  while the residual scatter is  $\sim 1 \text{ km s}^{-1}$ .

### 3.3.4 KIC 6449358

KIC 6449358 is a 5.8 day circular EB that may be a gravitationally bound to a distant tertiary companion.

The BF for this object exhibits two clear peaks, however, the second brightest peak is relatively stationary in RV while the brighter peak varies by  $\sim 60 \text{ km s}^{-1}$  over one orbit. This is shown in Figure 3.7 as well as in the Appendix 3.7. If the  $\sim$ stationary BF peak corresponded to a stellar binary component, it would require a system with an extremely large mass ratio  $M_2/M_1 > 10$ , which would be consistent with a white dwarf. However, the light curve constrains the radius ratio to be  $R_2/R_1 \sim 0.3$ , which makes this scenario physically implausible.

A more likely explanation for the  $\sim$ stationary RV component is that it belongs to a tertiary star,

**Figure 5.4** Best-fit Joint LC+RV Solution for KIC 6864859

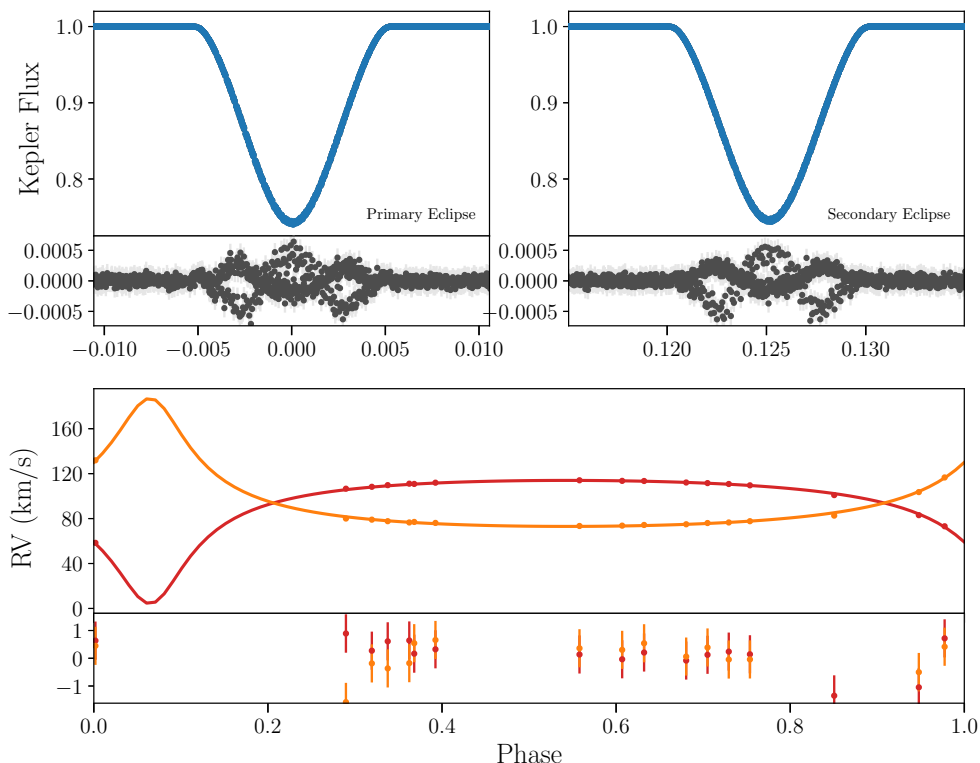


Figure 3.4: Simultaneous light curve (top panels) and RV (bottom panel) fits to *Kepler* and *APOGEE* observations of KIC 6864859. The primary and secondary eclipses are similar in shape and depth with  $\sim 25\%$  loss of light; the phase of the secondary eclipse and shapes of the RVs indicate an extremely eccentric system. The light curve residuals are small but have a coherent shape, likely due to tidal and rotational distortion of the stars.

and that the true secondary stellar component of the EB is too faint to be robustly detected by *APOGEE*. Indeed, the flux ratio in the *Kepler* bandpass is  $F_2/F_1 \sim 0.01$ . Thus, we effectively treat KIC 6449358 as a single-lined SEB in our model, and as a result we are only able to constrain the mass function,  $f_M$ , of the binary. Specifically, to reproduce the observed RV amplitude, our sum and ratio of mass solutions are degenerate, tending toward two extremes: high total mass ( $\sim 4 M_\odot$ ) with a low-mass ratio ( $q \sim 0.3$ ), or low total mass ( $1 M_\odot$ ) with a higher mass ratio ( $q \sim 0.67$ ).

We note that some *APOGEE* visits do suggest a small, third BF peak (see Appendix 3.7 for details). These marginal BF peaks have large RV variations from visit to visit, consistent with a low-mass star. This supports the scenario with a total mass  $\sim 2.3 M_\odot$  and a mass ratio of  $q \sim 0.45$ .

Figure 3.7 shows the best *KEBLAT* model fit to the light curve and RVs obtained using mass function  $f_M = \frac{M_2^3 \sin i}{(M_1 + M_2)^2}$  rather than  $M_1$  and  $M_2$ . The  $\sim$ stationary RV points, which are not fit, correspond to the putative third star, either a line-of-sight coincident or a tertiary companion in a hierarchical triple system. We favor the latter scenario, as the eclipses show timing varia-

**Figure 5.5** Eccentric Eclipsing System KIC 6864859

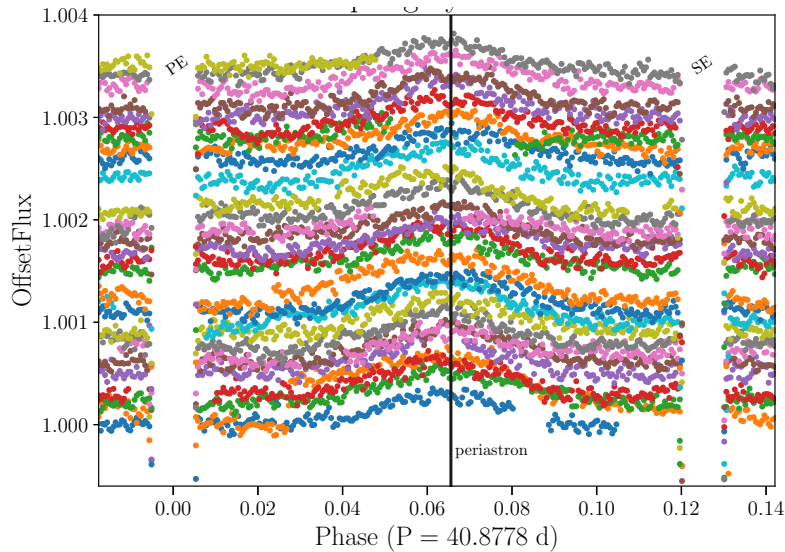


Figure 3.5: Heartbeat signatures of the eccentric eclipsing system KIC 6864659. The light curve surrounding the primary and secondary eclipses is folded in phase and offset vertically between each observed orbit, using different colors for visual clarity. The brightening between the primary and secondary eclipse is readily apparent around phase 0.065.

tions consistent with perturbations by a bound, tertiary component. These eclipse timing variations (ETVs) have been used to identify and characterize many *Kepler* EBs (e.g. Borkovits et al., 2016), and we fit these ETVs using a simple linear ephemeris based on the observed times of the primary eclipse. We then compute the observed minus computed ( $O - C$ ) eclipse times as a function of time. The result is shown in Figure 3.8. There is a clear parabolic or sinusoidal trend in the ETVs with an amplitude of  $\sim 0.0006$  day; the ETV timescale indicates that the perturbing tertiary body has a minimum period  $\sim 1450$  days. The architecture of this type of hierarchical triple – short, circular inner binary orbited by a distant tertiary companion – is consistent with dynamical processing via the Kozai (1962) mechanism.

### 3.3.5 KIC 4285087

KIC 4285087 is an equal mass binary ( $M_1 \approx M_2 \approx 1.1M_\odot$ ) in a circular, slightly inclined ( $i = 87^\circ.3$ ) 4.5 day orbit. We show the best-fit solution in Figure 3.9. The components are main-sequence dwarfs with similar radii ( $R_1 \sim R_2 \sim 1R_\odot$ ). The eclipses are of similar depth ( $\sim 30\%$ ), duration ( $\sim 0.2$  day), and shape (V), consistent with equal mass dwarfs orbiting each other.

4

<sup>4</sup>In KIC 6131659, the  $\sim$ stationary RV points near  $\sim 80\text{km s}^{-1}$  are measured RVs of a tertiary companion, while the orange curve shown here is the predicted RV of the unseen secondary, based on the locations of tentative BF peaks in the Appendix (see §??). The flat-bottom secondary eclipse indicates that the system is close to edge-on with a radius ratio of  $\sim 0.33$ , breaking the inclination-radius ratio degeneracy. The primary eclipse residuals are signifi-

**Figure 5.6** Best-fit Joint LC+RV Solution for KIC 6778289

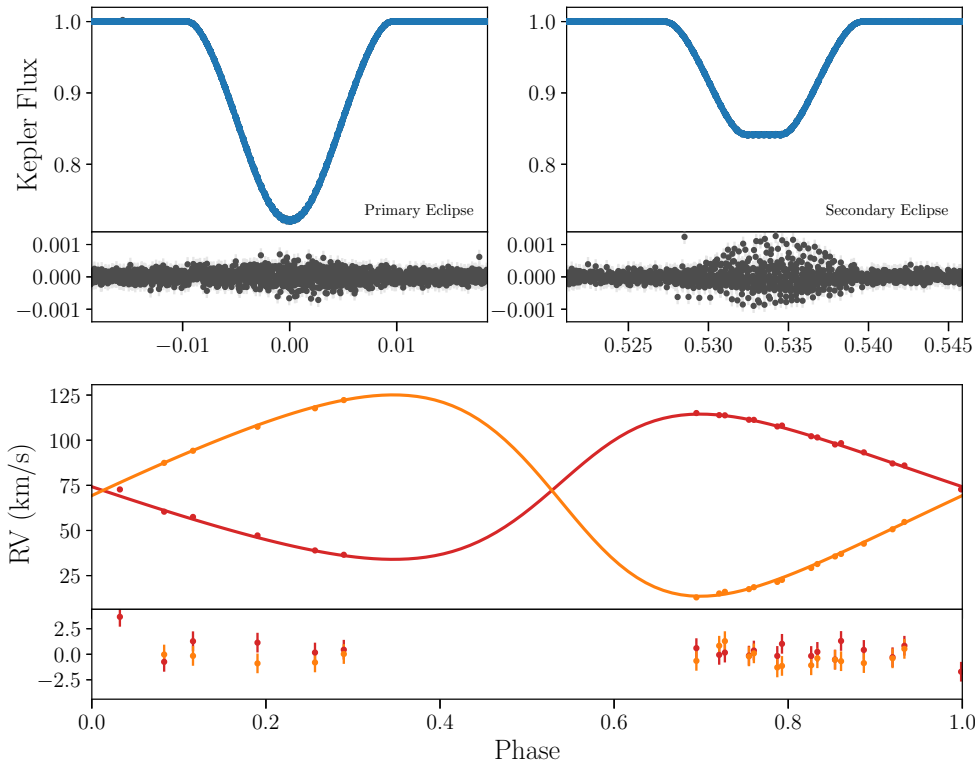


Figure 3.6: Simultaneous light curve (top panels) and RV (bottom panel) fits to *Kepler* and *APOGEE* data for KIC 6778289. Different eclipse depths along with a flat-bottomed secondary eclipse indicate a smaller and dimmer secondary. Additionally, the unequal amplitudes and shape of the RV indicates an unequal mass binary with significant orbital eccentricity.

### 3.3.6 KIC 6131659

KIC 6131659 is a mass ratio of 0.75 binary ( $M_1 = 0.9 M_\odot$ ,  $M_2 = 0.7 M_\odot$ ) in a 17.5 day, close-to-circular orbit. Figure 3.10 shows the simultaneous RV+LC fit to the data. The primary and secondary eclipses are relatively deep, with 35% and 10% losses of total system light, respectively. The residuals to the light curve fit show correlated structure, which may be due to poor limb-darkening modeling and/or a varying third light component which deviates from the *Kepler* crowding values.

There is a third light component readily visible in the BF (see Appendix in §?? Figure ??), but it is not RV-variable. This suggests it may be a line-of-sight contamination source or a gravitationally bound body in a hierarchical triple with an orbital period much longer than 17.5 days. The light curve does not show apparent ETVs, but this does not preclude the presence of a gravitationally bound tertiary.

---

cant during ingress and egress, consistent with eclipse timing variations due to a tertiary companion (see Figure 3.8

**Figure 5.7** Best-fit Joint LC+RV Solution for KIC 6864859

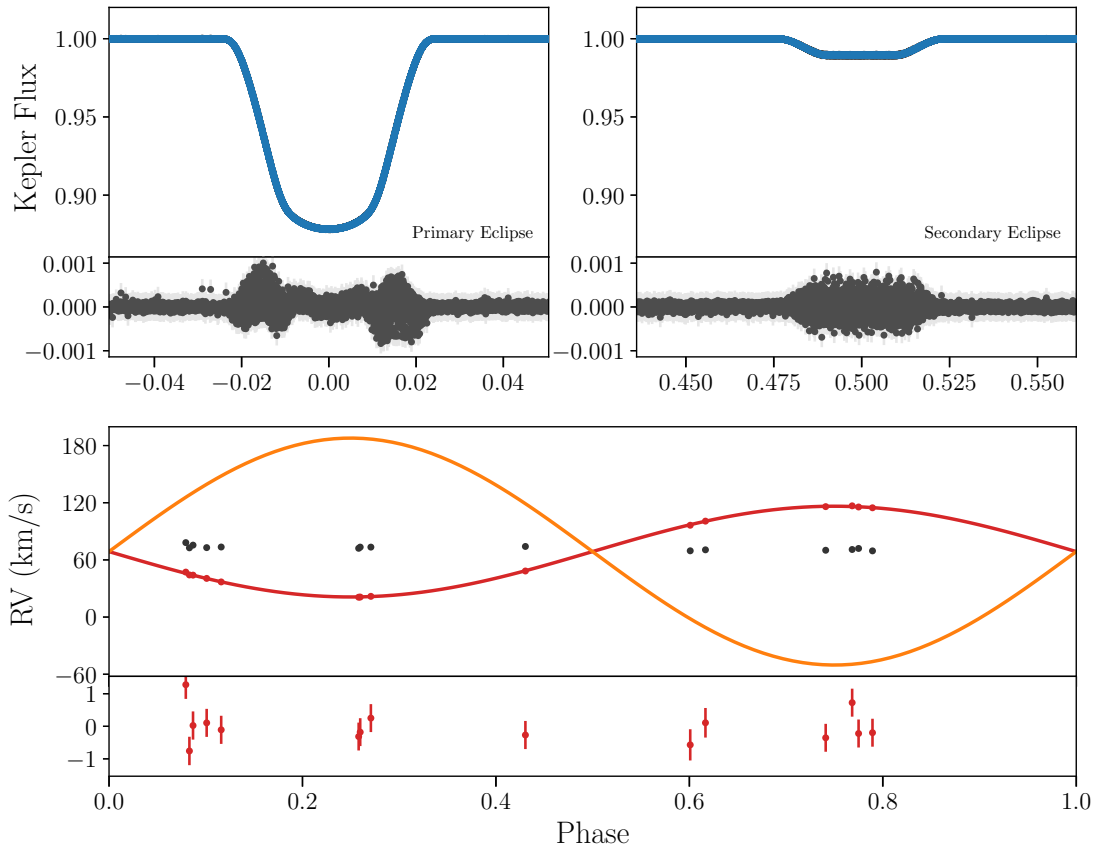


Figure 3.7: Simultaneous RV+LC fit for KIC 6449358, a single-lined spectroscopic binary suspected in a hierarchical triple system. We utilize mass function here rather than individual component masses to obtain the RV fit.)

### 3.3.7 KIC 6781535

KIC 6781535 is an eccentric ( $e = 0.25$ ), grazing ( $i = 84^\circ$ ), 9.1 day binary. The best-fit solution (see Figure 3.11) yields binary components of similar masses ( $M_2/M_1 \approx 1.0$ ) but slightly different radii ( $R_2/R_1 \approx 1.2 \pm 0.1$ ), which suggests a slightly evolved system. The shallow eclipses poorly constrain the system's impact parameter, flux ratio, and radius ratio. As a result of this degeneracy, we apply a Gaussian prior on the light curve flux ratio parameter from spectra, following the same method as used for KIC 5285607 (see section 3.3.1).

Similarly to KIC 6131659, there is a third light component visible in the BF (see Figure 3.11) that is not RV-variable, indicating either a line-of-sight coincident third star or gravitationally bound tertiary companion. There are symmetric structures in the light curve residuals, most noticeably during primary eclipse, consistent with variable third light contribution, changes to the binary orbit due to additional bodies, or starspot modulations. Because the system exhibits shallow, grazing eclipses, it was not conducive to an ETV analysis.

**Figure 5.8** Primary Eclipse Timing Variations for KIC 6449358

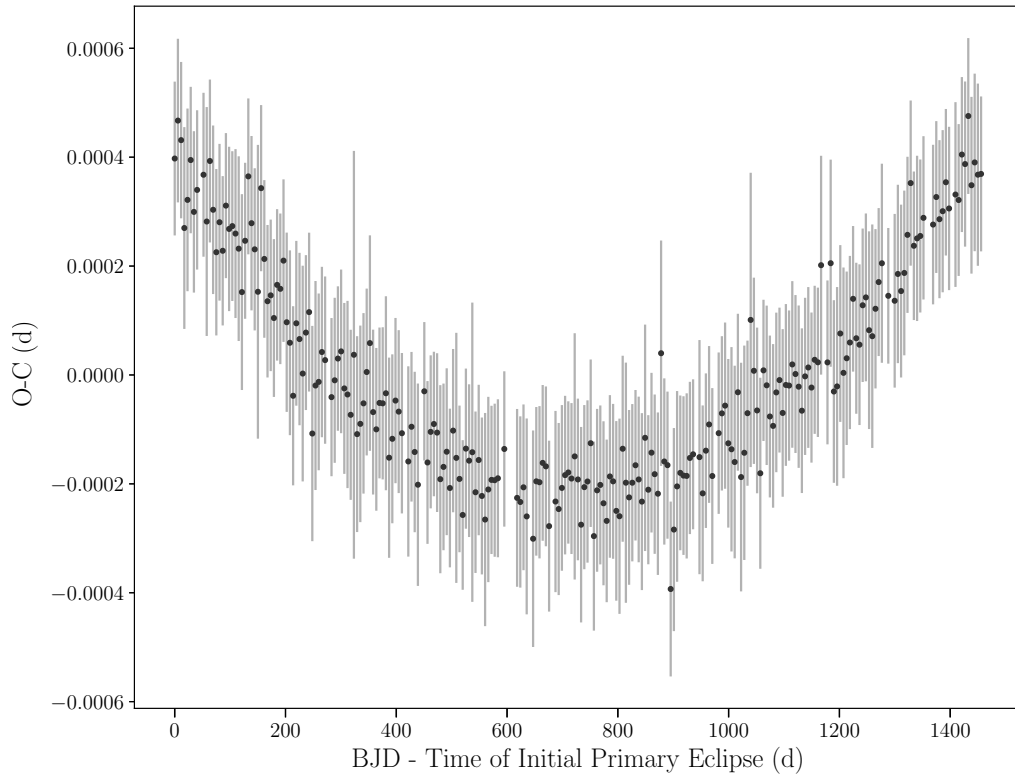


Figure 3.8:  $O - C$  diagram for KIC 6449358, showing primary eclipse timing variations; the ETVs exhibit a half-sinusoid trend, giving a rough estimate for the minimum period of the tertiary perturber to be  $P \sim 1450$  days.

### 3.3.8 Supplemental Physical Parameters

In addition to the main results in Table 3.3, we report some additional physical parameters in Table 3.3.8. As discussed in Section 3.2.6, we can use the BF peak area ratios to measure the  $H$ -band flux ratio of each system. We can also combine *Gaia* parallax information with our measured fluxes, radii, and the ASPCAP  $T_{\text{eff}}$  to estimate individual stellar temperatures. These parameters, along with adopted values from external sources, are summarized in Table 3.3.8.

**Figure 5.8** Primary Eclipse Timing Variations for KIC 6449358

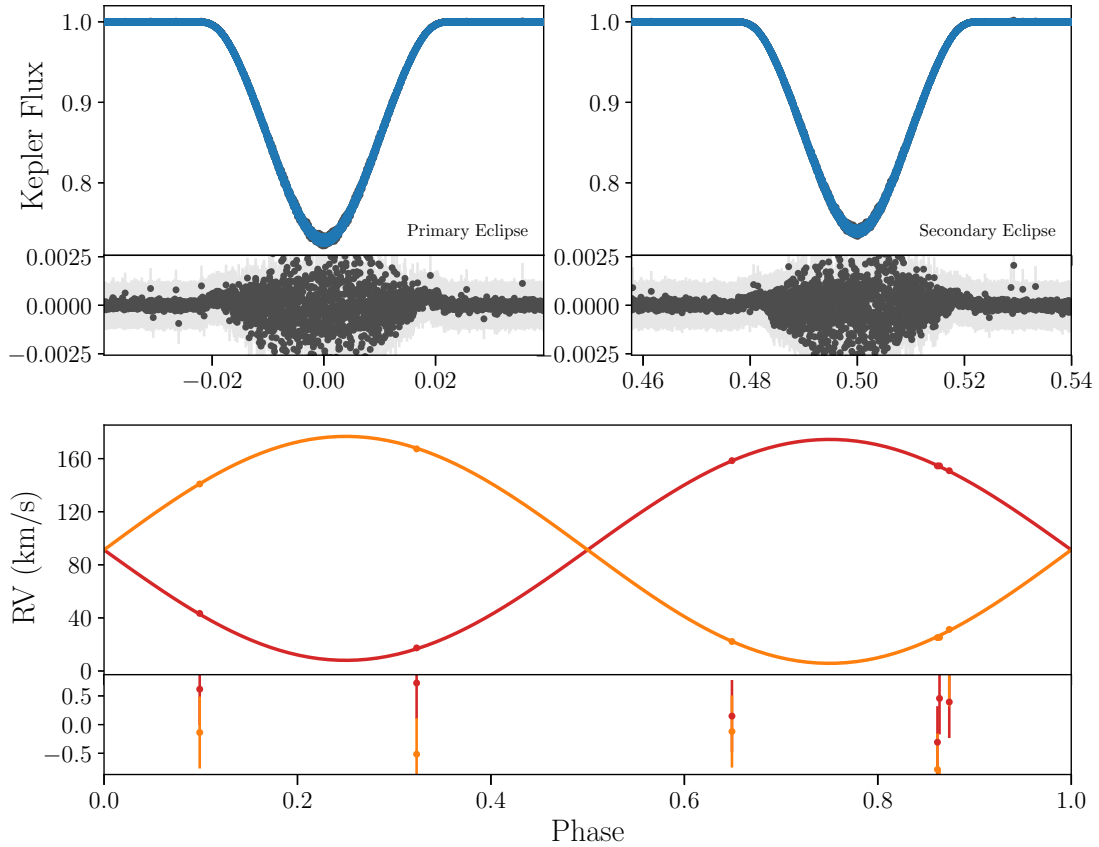


Figure 3.9: Simultaneous light curve (top panels) and RV (bottom panel) fits to the *Kepler* and *APOGEE* observations. The phase of secondary eclipse and shape of RVs indicate EBs in a  $\sim$  circular orbit. The light curve residuals during eclipse suggest the presence of a variable third light contribution, or non-Keplerian photometric effects given its short period. ( $\sim$  4 days).



**figure 5.9** Best-fit Joint LC+RV Solution for KIC 4285087

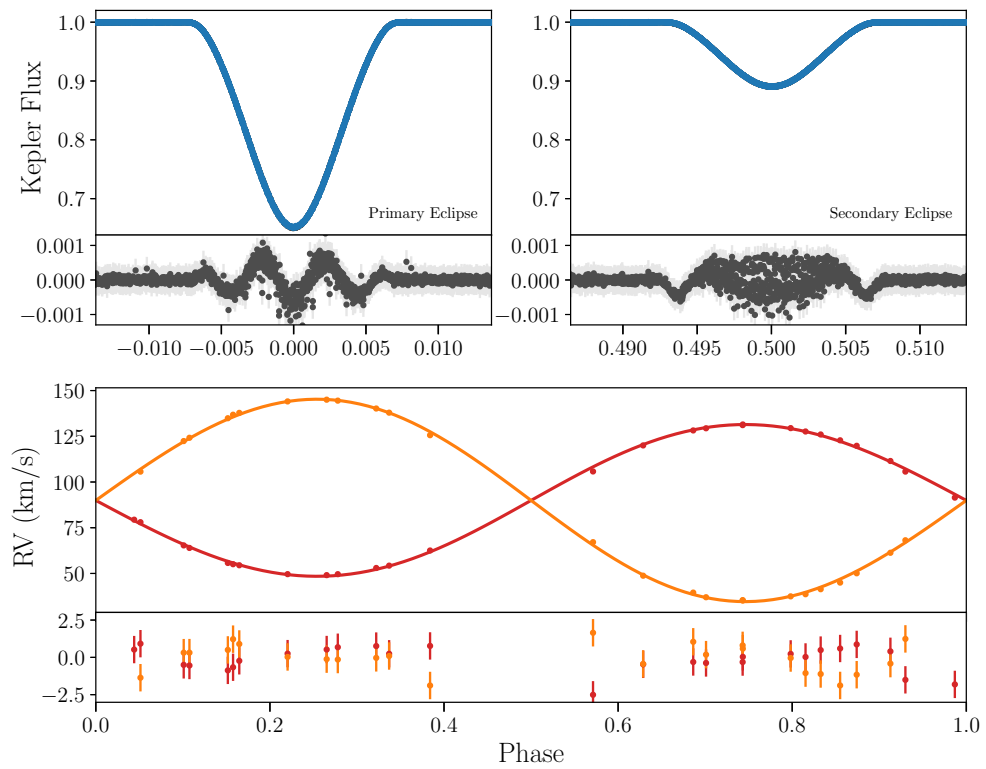


Figure 3.10: Simultaneous light curve (top panels) and RV (bottom panel) fits to the *Kepler* and *APOGEE* observations for KIC 6131659. The primary and secondary eclipses are relatively deep, with 35% and 10% losses of total system light, respectively.

**figure 5.10** Best-fit Joint LC+RV Solution for KIC 6131659

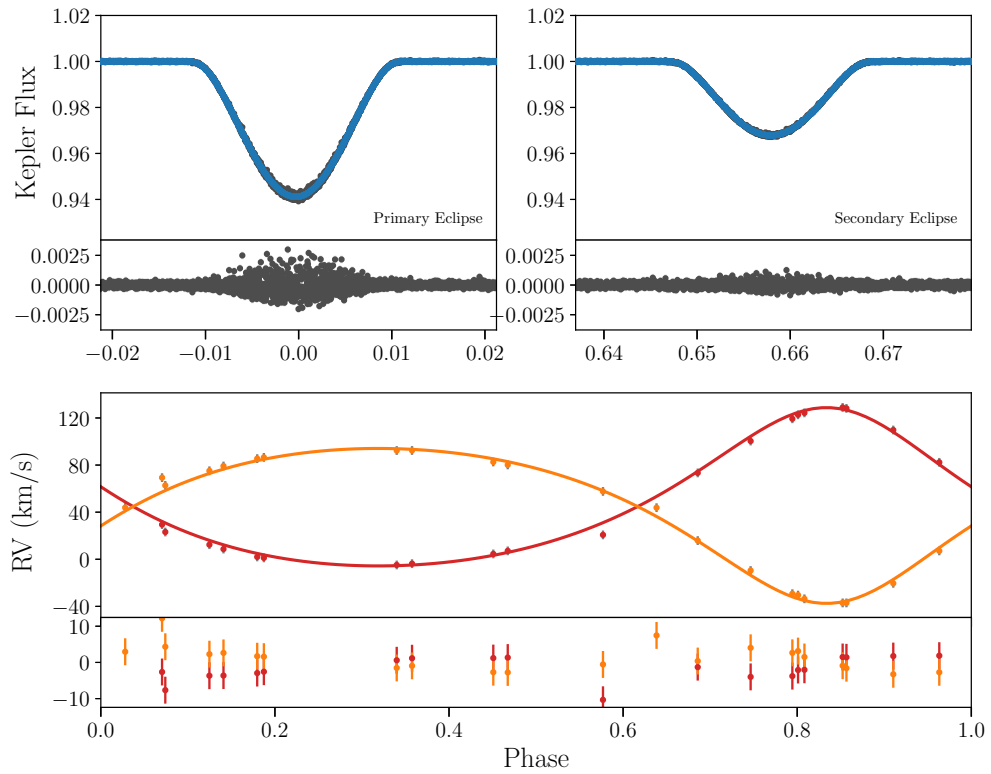


Figure 3.11: Top panels show the light curve model (blue) for KIC 6781535 overlaid against data (gray) as a function of phase. Bottom panel shows the RV model (lines) for primary (red) and secondary (orange) components overlaid on top of the APOGEE-extracted data (points). The models correspond to the best-fit joint LC+RV solution.

Table 3.3: Parameters Related to RV Extraction and Temperature Estimates

	KIC 5285607	KIC 6864859	KIC 6778289	KIC 6449358	KIC 4285087	KIC 6131659	KIC 6781535 <sup>a</sup>
BF flux ratio ( $F_2/F_1$ )	$0.620 \pm 0.027$	$0.811 \pm 0.028$	$0.462 \pm 0.029$	$0.392 \pm 0.014$	$0.997 \pm 0.023$	$0.648 \pm 0.028$	$1.253 \pm 0.115$
ASPCAP $T_{\text{eff}}$ (K) <sup>a</sup>	$6495 \pm 156$	$6417 \pm 159$	$6572 \pm 162$	$6237 \pm 179$	$5664 \pm 146$	$4845 \pm 98$	$5749 \pm 125$
Gaia parallax (mas) <sup>b</sup>	$1.254 \pm 0.0216$	$1.4897 \pm 0.0241$	$0.9093 \pm 0.0222$	$1.1974 \pm 0.0264$	$1.619 \pm 0.0312$	$-0.5117 \pm 1.0713$	...
Gaia distance (pc) <sup>b</sup>	$799 \pm 14$	$671 \pm 11$	$1100 \pm 27$	$835 \pm 18$	$617 \pm 12$	...	...
$\log g_1$ (cgs) <sup>c</sup>	$4.028 \pm 0.013$	$4.150 \pm 0.010$	$4.133 \pm 0.008$	...	$4.454 \pm 0.006$	$4.496 \pm 0.005$	$4.161 \pm 0.019$
$\log g_2$ (cgs) <sup>c</sup>	$4.118 \pm 0.015$	$4.244 \pm 0.012$	$4.479 \pm 0.010$	...	$4.478 \pm 0.007$	$4.705 \pm 0.006$	$4.253 \pm 0.021$
$T_{\text{eff}}$ offset (K) <sup>d</sup>	350	80	250	...	20	350	100
Adopted $T_{\text{eff},1}$ (K)	$6845 \pm 328$	$6497 \pm 159$	$6822 \pm 162$	$6737 \pm 178$	$5689 \pm 146$	$5195 \pm 98$	$5849 \pm 125$
Adopted $T_{\text{eff},2}$ (K)	$6716 \pm 293$	$6541 \pm 283$	$7265 \pm 440$	$8788 \pm 658$	$5735 \pm 105$	...	...

<sup>a</sup> DR14 (Pérez et al., 2016) <sup>b</sup> Bailer-Jones et al. (2018) <sup>c</sup> Computed directly from  $M$  and  $R$  as reported in Table 3.2. <sup>d</sup> El-Badry et al. (2017)

## 3.4 Discussion

### 3.4.1 Evolutionary Histories

With such well-characterized stars, we can investigate each binary’s age and evolutionary history with two different approaches. In the following we assume normal Milky Way metallicities of  $-0.5 < [M/H] < 0$ .

First we explore the  $H$ - $R$  diagram in  $\log g$  vs.  $\log T_{\text{eff}}$  after first correcting our temperature estimates following El-Badry et al. (2017). We calculate  $\log g$  for each star directly from the `KEBLAT` mass and radius. We also use the `KEBLAT` masses and radii to determine the system ages in the mass-radius space directly, which avoids any dependence on distance or on our disentangling of the individual component temperatures.

In both approaches, we use Dartmouth evolutionary tracks (Dotter et al., 2008) and consider only the portion of the track with  $\log g \geq 4.1$ . This effectively only includes the main sequence. For consistency, we adhere to the `KEBLAT` definition of star 1 (primary) and star 2 (secondary) in which star 1 is the member of the SEB being eclipsed during the primary eclipsing event, and star 2 (secondary) as the member eclipsed during the secondary eclipsing event.

Figure 3.12 shows all of the SEBs in the  $\log g$  vs.  $\log T_{\text{eff}}$  diagram, and Figure 3.13 shows each SEB system individually. In general, the systems are broadly consistent with ages ranging from about 0.8 to about 3 Gyr, and the two components of each system appear to be consistent with a common age. Figure 3.14 represents these systems in the mass-radius diagram, where again all six systems modeled appear consistent with coevality for the same range of ages as above.

### 3.4.2 Mass-Luminosity Relationships

In order to verify that our targets are on the main sequence, we create a mass-luminosity plot (Figure 3.15) using the stellar masses from Table 3.3 and calculated  $H$ -band luminosities explained below. These luminosities are independent of the ASPCAP temperature estimates and corrections from El-Badry et al. (2017) used to derive Figures 3.13 and 3.14. The results represent a comparison to theoretical models that complements the mass-radius relationship presented in Figure 3.14, and is less reliant on light curve modeling, which may have degenerate radius solutions in grazing geometries. To calculate  $H$ -band luminosities, we use distances derived from *Gaia* parallaxes (Bailer-Jones et al., 2018) to convert apparent  $H$ -band magnitudes from 2MASS (Skrutskie et al., 2006) to absolute magnitudes. We check that the  $H$ -band magnitudes were not taken during eclipse by cross referencing the time of 2MASS observations to the EB ephemeris. We then compute the system  $H$ -band luminosities from absolute magnitudes using the sun as a reference, with an  $H$ -band magnitude of 3.32 from Cohen et al. (2003). We disentangle the separate luminosities for each stellar component in the system using the observed *APOGEE*  $H$ -band flux ratios (see Table 3.3). In Figure 3.15, we show each system using the same plotting convention as Figures 3.12 to 3.14, where solid and open circles correspond to primary and secondary components, respectively. We overplot for comparison theoretical masses and  $H$ -band magnitudes from Dartmouth isochrones (Dotter et al., 2008) at subsolar and solar metallicity and a range of ages (0.8-5 Gyr). In general, as previously concluded, members of the same binary system follow the same evolutionary track, i.e., are coeval.

**Figure 5.11** Spectroscopic  $H$ - $R$  Diagram for Systems with *Gaia* Distances

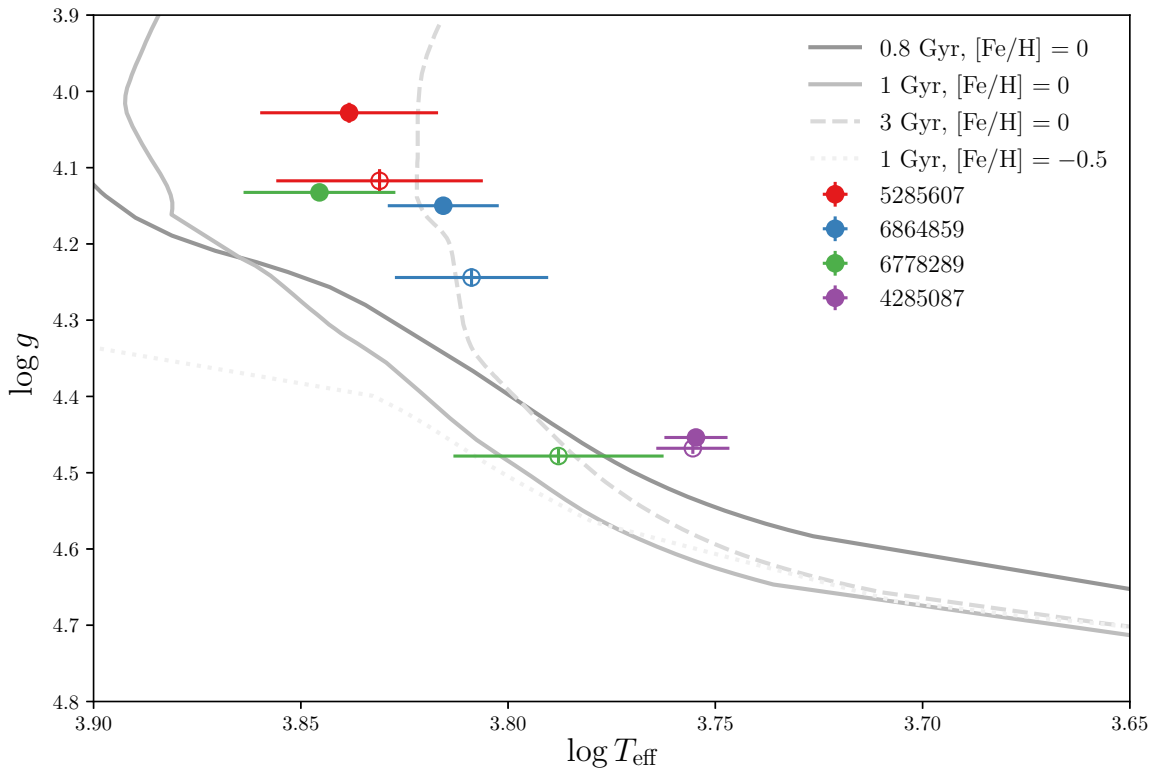


Figure 3.12: Spectroscopic  $H$ - $R$  diagram for the systems with *Gaia* distances. Primaries are depicted with the solid circles while secondaries are open circles. A variety of Dartmouth isochrones are plotted with a range of ages 0.8–3 Gyr and metallicities (subsolar to solar).

We exclude KIC 6449398 from this analysis, because it is a single-lined SEB. We also exclude KICs 6131659 and 6781535, which have negative parallax values from *Gaia*. For this reason we could not include these targets in the spectroscopic  $H$ - $R$  diagram for our systems with *Gaia* distances. We did not include reddening corrections to the distance modulus calculations; however, reddening effects should be minimal in the near-IR (2MASS and *APOGEE*  $H$ -band) compared to the visible (*Kepler*).

### 3.4.3 Tertiary Companions

In our subset of SEBs, we identified three candidate triple systems. The binaries with possible tertiary companions are KIC 6131659, KIC 6781535, and KIC 6449358 (see Sections 3.3.6, 3.3.7, and 3.3.4, respectively). The first two of these systems exhibit clear third BF component peaks in nearly all RV visits. We fit these third peaks with Gaussians, similar to the Gaussian fits for the primary and secondary BF components. In both cases, the third BF components do not have RV variations above the noise, which suggest that these third members are either line-of-sight contamination sources or gravitationally bound in hierarchical triples with orbital periods much longer than that of the observed SEB.

**Figure 5.12** Spectroscopic *H-R* Diagram for Systems with *Gaia* Distances

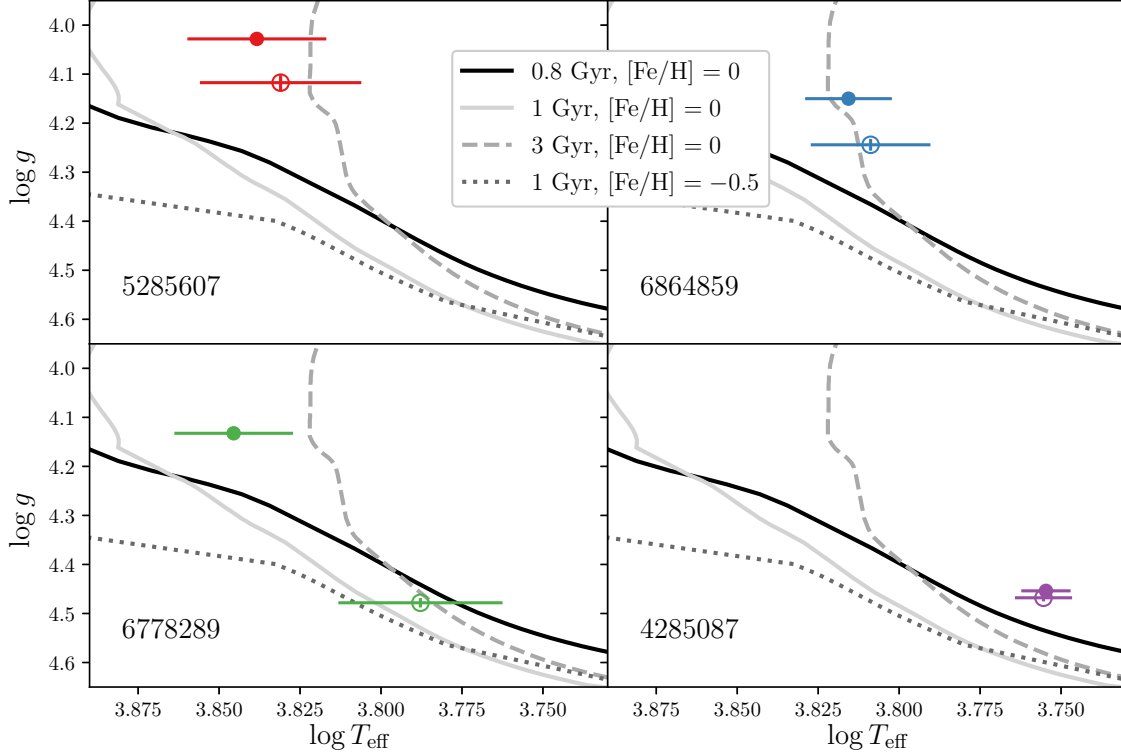


Figure 3.13: Same as Figure 3.12, showing each SEB system individually. The filled circles model the primary star of the SEB, and the hollow circles the secondaries.

While statistics on multiplicity are not complete, numerous studies have found tertiary systems composed of a tight binary orbited by a distant third member. Statistics from Tokovinin et al. (2006) indicate that roughly 63% of spectroscopic binaries have tertiary companions in a wide orbit. In binaries with shorter periods (less than 3 days) this percentage rises to 96%, but in longer period binaries (12 or more days) this percentage is only 34%.

The incidence of triples among *Kepler* close eclipsing binaries (as are the ones in our analysis) is at least  $\sim 20\%$  (Rappaport et al., 2013; Conroy et al., 2014), and likely higher for tertiaries with longer periods beyond *Kepler*'s finite observing time.

Evidence from both spectroscopic and photometric observations indicate that KIC 6449358 belongs to a hierarchical triple system (see section 3.3.4). The BF for this system shows a stationary tertiary peak in a few of the *APOGEE* visits. The mid times of eclipses in the *Kepler* light curve also exhibit sinusoidal variations in time; these ETVs indicate that the tertiary has a period  $\gtrsim 1450$  days.

Interestingly, among our sample we do not detect tertiary companions among the shortest-period binaries. In particular, neither of the two EBs with  $P_{\text{orb}} < 5$  days exhibit a clear tertiary in our data. It is not yet clear whether existing observations might already exclude the presence of tertiaries at very large separations that might not appear in our data; additional imaging observations might be required to identify such stars. At the same time, two of the four

**Figure 5.13** Radius Versus Mass

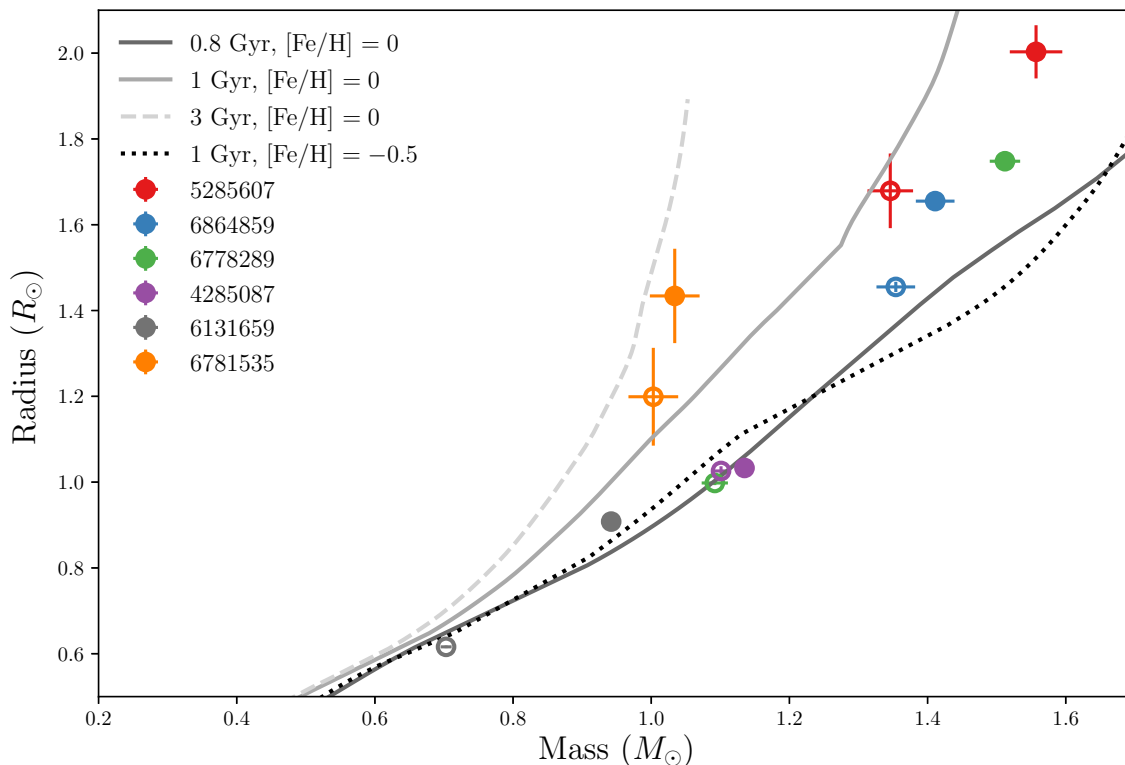


Figure 3.14: Radius versus mass diagram for all seven systems. Primaries are shown as solid circles and secondaries as open circles. Dartmouth isochrones for a variety of ages and metallicities are also plotted. All seven systems are consistent with coevality, ranging in age from about 1 to about 3 Gyr, assuming a normal Milky Way metallicity of  $[M/H] = -0.5$

EBs with  $P_{\text{orb}} > 9$  days are triples, which would appear to be an overabundance of tertiaries among the longest-period EBs, albeit with a small sample. However, we note that one of these (KIC 6781535,  $P_{\text{orb}} \approx 9$  days) is a modestly evolved system (see Figure 3.14), and excluding that case yields an occurrence of one-third of triples among our EBs with  $P_{\text{orb}} > 12$  days), fully consistent with the results of Tokovinin et al. (2006).

### 3.5 Summary

We thoroughly characterize seven SEBs that have been observed by both *Kepler* and *APOGEE*. Our targets are selected from the *Kepler* EB catalog, and limited to bright, detached EB targets with both primary and secondary eclipses observed by *Kepler*, high inclination, and multiple *APOGEE* visits. We identify an additional 26 SEBs which may warrant similar studies. We demonstrate that the BF is a superior method for extracting RVs from *APOGEE* visit spectra compared to the CCF used in the present reduction pipeline. This is particularly true for systems with multiple RV-variable components. While such an analysis is beyond the scope of this work,

**Figure 5.15** Mass-luminosity Relationship

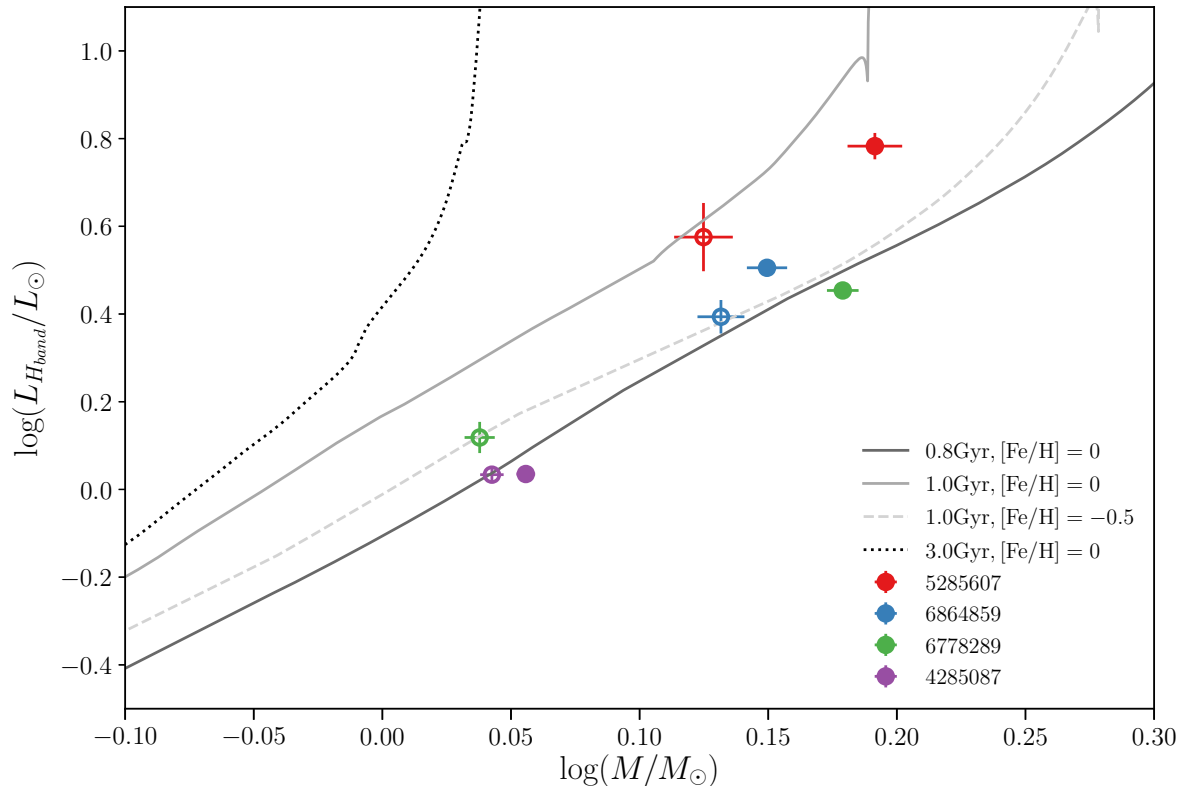


Figure 3.15: Mass-luminosity relationship for the four targets with accurate *Gaia* distances and RV-derived masses. The primaries are shown in solid circles and secondaries in open circles. Dartmouth isochrones (Dotter et al., 2008) are overplotted as gray lines, corresponding to a variety of ages and metallicities.

if the BF method were applied to the full data set of multiple-visit *APOGEE* targets, it would most likely reveal many previously unknown SEBs and other interesting RV-variable sources. RVs are extracted from `apVisit` spectra using the BF method and the *Kepler* light curves are normalized, de-weighted, and modeled using `KEBLAT`. The light curve and RV solutions are first determined individually, and then computed simultaneously. We use the resulting physical parameters to estimate stellar temperatures, investigate coevality, and explore candidate triple systems.

Using our analysis we find that our target’s binary members are coeval with ages ranging from 1 to 3 Gyr, assuming normal Milky Way metallicity ( $-0.5 < [M/H] < 0$ ). The exception is KIC 6781535, which lies closer to a slightly metal poor ( $[M/H] \sim -1.0$ ) 3 Gyr isochrone. Our systems being broadly consistent with coevality confirms a common assumption in star formation that members of multiples form at the same time, and also effectively calibrates stellar evolution modeling.

Overlap between large-scale surveys like *APOGEE*, *Kepler*, and *Gaia* allows us to discover and analyze many diverse SEBs, including systems with very low flux ratios and those in higher order systems. The statistics on the triples within our subset with respect to the orbital period of inner



binaries is broadly consistent with statistics from the field Tokovinin (1997), though there may be some tension with our sample in that the shortest-period EBs do not appear to be spectroscopic triples. This is in contrast to the expectation that shortest-period EBs are most likely to be hierarchical triples. It is possible that very wide tertiaries do exist in these systems but have yet to be identified via imaging.

We have shown that through tools like *KEBLAT* and the BF analysis of *APOGEE* spectra, it is possible to perform high-quality analysis of large numbers of SEBs with a variety of properties. This opens up great promise for future SEBs identified in *TESS* and *SDSS-V* data.

## **3.6 Acknowledgements**

We would like to thank Scott Fleming for critical guidance and discussion and Paul A. Mason for valuable brainstorming and advice. We recognize the SDSS Faculty And Student Team (FAST) initiative for supporting this work through a partnership with New Mexico State University. J=MC<sup>2</sup> thanks the Fisk-Vanderbilt Masters-to-PhD Bridge Program, Amanda Cobb, Kelly Holley-Bockelmann, and Nancy Chanover for continued empowerment of a woman and new mother in STEM. M.L.R celebrates that this work has encompassed two births, one wedding, and multiple graduations among the lead authors.

## **3.7 Clark-Cunningham et al. 2019 Appendix**

### **3.7.1 TIC 021980925**

### **3.7.2 TIC 283889669**

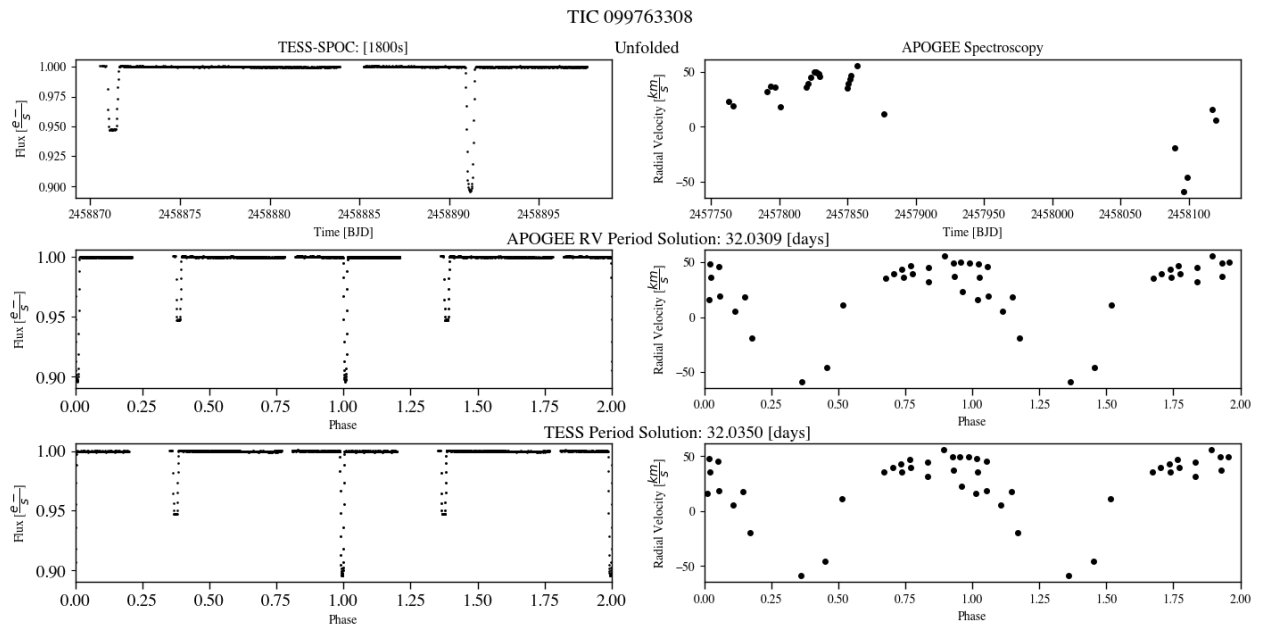


Figure 3.16: TIC 099763308 Spectroscopic and Photometric analysis: **Top-Left:** Unfolded *TESS-SPOC* LC. **Top-Right:** Unfolded *APOGEE* RV curve. **Middle-Left:** *TESS-SPOC* LC folded onto the *APOGEE Gold Sample* period solution. **Middle-Right:** *APOGEE* RV curve folded onto the *APOGEE Gold Sample* period solution. **Bottom-Left:** *TESS-SPOC* LC folded onto our *TESS* BLS periodicity estimate. **Bottom-Right:** *APOGEE* RV curve folded onto our *TESS* BLS periodicity estimate.

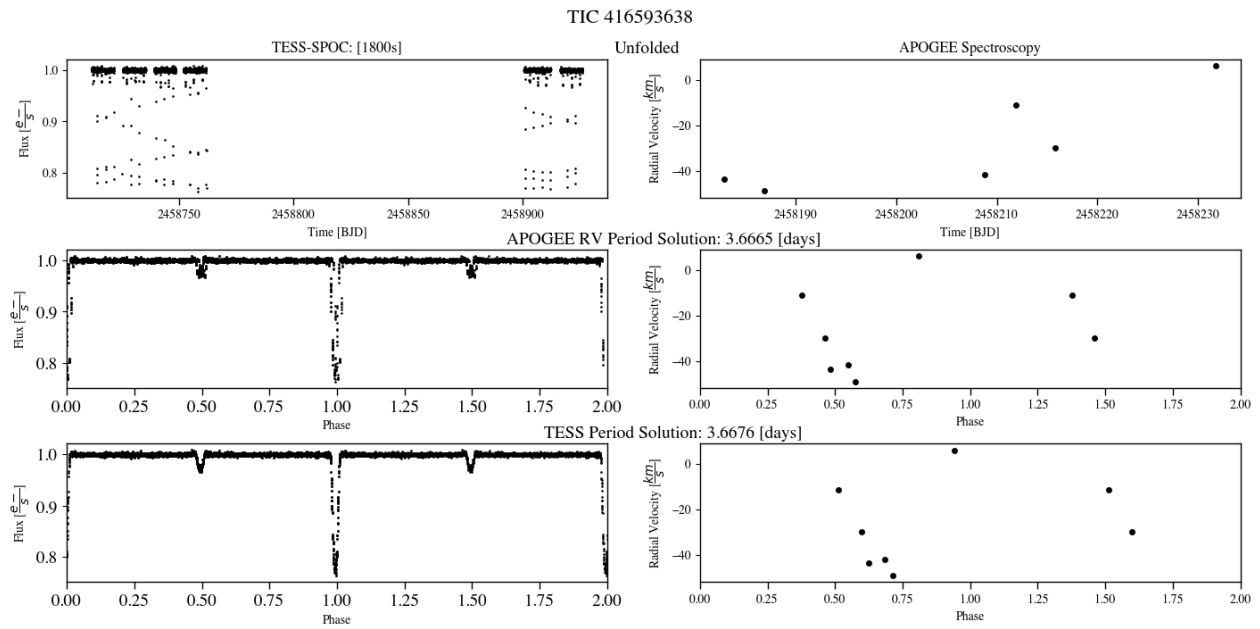


Figure 3.17: TIC 416593638 Spectroscopic and Photometric analysis: **Top-Left:** Unfolded *TESS-SPOC* LC. **Top-Right:** Unfolded *APOGEE* RV curve. **Middle-Left:** *TESS-SPOC* LC folded onto the *APOGEE Gold Sample* period solution. **Middle-Right:** *APOGEE* RV curve folded onto the *APOGEE Gold Sample* period solution. **Bottom-Left:** *TESS-SPOC* LC folded onto our *TESS* BLS periodicity estimate. **Bottom-Right:** *APOGEE* RV curve folded onto our *TESS* BLS periodicity estimate.

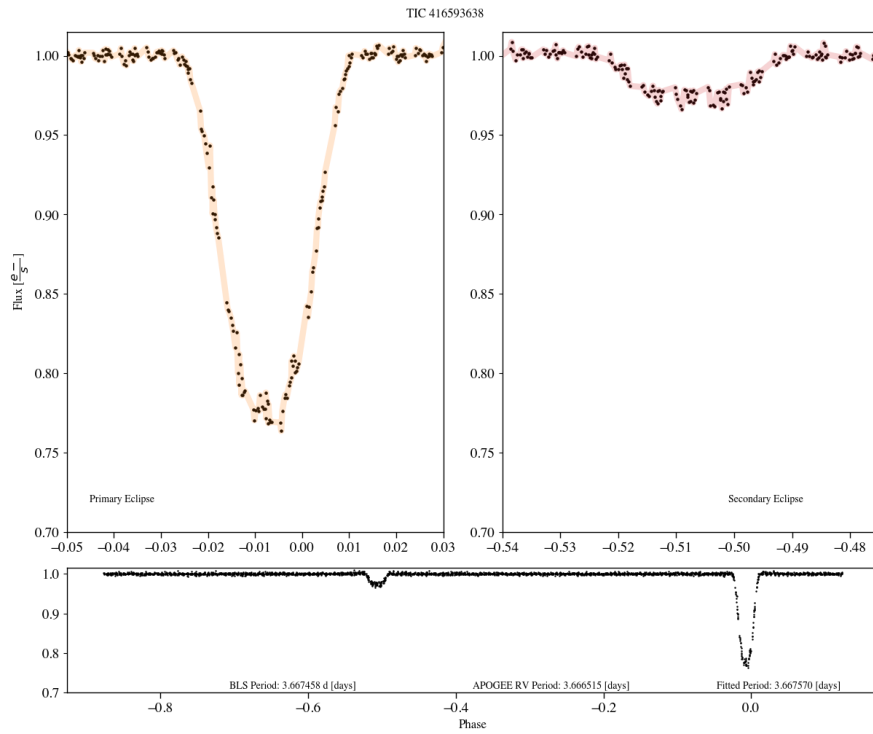


Figure 3.18: TIC 416593638 Primary and Secondary eclipsing events. These eclipsing events are derived through folding the *TESS-SPOC* photometry onto the results of its BLS periodicity analysis.

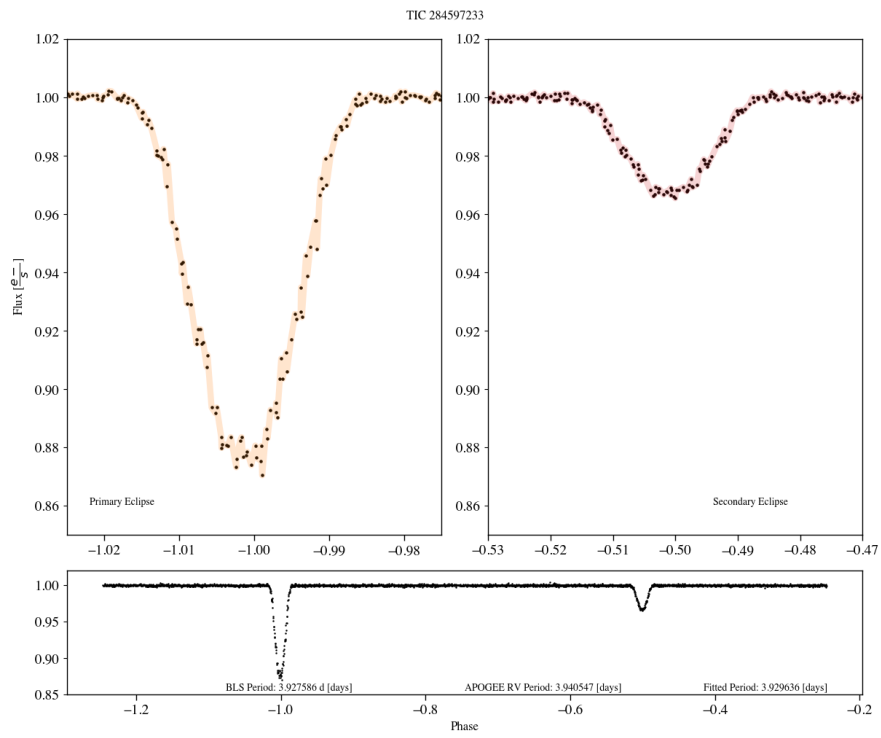


Figure 3.19: TIC 284597233 Primary and Secondary eclipsing events. These eclipsing events are derived through folding the *TESS-SPOC* photometry onto the results of its BLS periodicity analysis and subsequent iterative fit of diminishing step sizes. This target inherited noise in its photometry even after normalization and smoothing were completed by the *Astropy* and *wotan* packages.

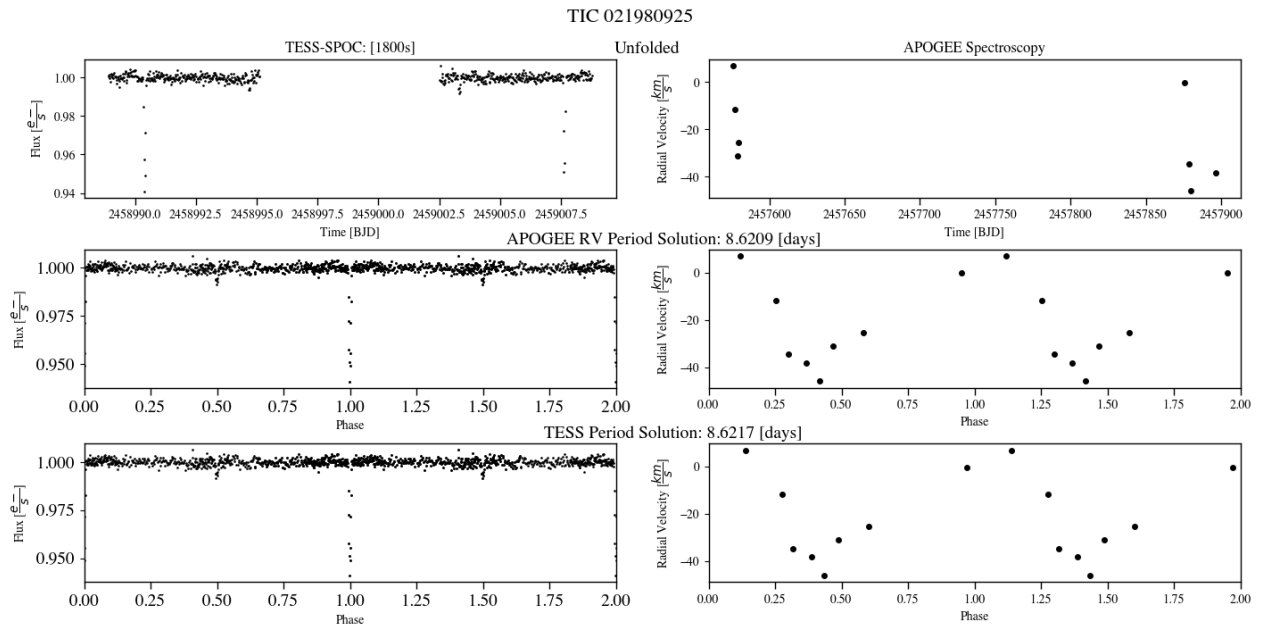


Figure 3.20: TIC 021980925 Spectroscopic and Photometric analysis: **Top-Left:** Unfolded *TESS-SPOC* LC. **Top-Right:** Unfolded *APOGEE* RV curve. **Middle-Left:** *TESS-SPOC* LC folded onto the *APOGEE Gold Sample* period solution. **Middle-Right:** *APOGEE* RV curve folded onto the *APOGEE Gold Sample* period solution. **Bottom-Left:** *TESS-SPOC* LC folded onto our *TESS* BLS periodicity estimate. **Bottom-Right:** *APOGEE* RV curve folded onto our *TESS* BLS periodicity estimate.

figures/JMCC2022/TIC283889669LC\_RV\_phase.png

Figure 3.21: TIC 283889669 Spectroscopic and Photometric analysis: **Top-Left:** Unfolded *TESS-SPOC* LC. **Top-Right:** Unfolded *APOGEE* RV curve. **Middle-Left:** *TESS-SPOC* LC folded onto the *APOGEE Gold Sample* period solution. **Middle-Right:** *APOGEE* RV curve folded onto the *APOGEE Gold Sample* period solution. **Bottom-Left:** *TESS-SPOC* LC folded onto our *TESS* BLS periodicity estimate. **Bottom-Right:** *APOGEE* RV curve folded onto our *TESS* BLS periodicity estimate.

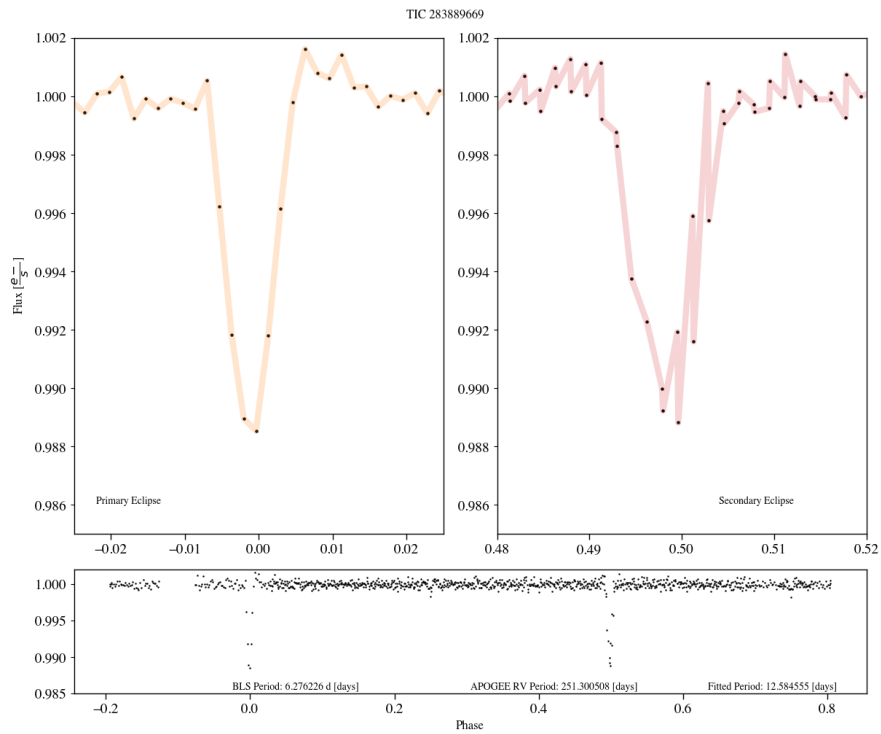


Figure 3.22: TIC 283889667 Primary and Secondary eclipsing events. These eclipsing events are derived through folding the *TESS-SPOC* photometry onto the results of its BLS periodicity analysis. From the shape of the eclipsing events in this system it is likely that this system is a total eclipsing binary, close to being directly in our line of sight.



## CHAPTER 4

### **A *KELT/TESS* Eclipsing Binary in a Young Triple System Associated with the Local "Stellar String" Theia 301**

#### Abstract<sup>1</sup>

HD 54236 is a nearby, wide common-proper-motion visual pair that has been previously identified as likely being very young by virtue of strong X-ray emission and lithium absorption. Here we report the discovery that the brighter member of the wide pair, HD 54236A, is itself an eclipsing binary (EB), comprising two near-equal solar-mass stars on a 2.4-d orbit. It represents a potentially valuable opportunity to expand the number of benchmark-grade EBs at young stellar ages. Using new observations of Ca II H&K emission and lithium absorption in the wide K-dwarf companion, HD 54236B, we obtain a robust age estimate of  $225 \pm 50$  Myr for the system. This age estimate and *Gaia* proper motions show HD 54236 is associated with Theia 301, a newly discovered local "stellar string", which itself may be related to the AB Dor moving group through shared stellar members. Applying this age estimate to AB Dor itself alleviates reported tension between observation and theory that arises for the luminosity of AB Dor C when younger age estimates are used.

#### **4.1 Introduction**

Eclipsing binary (EB) stars are foundational to stellar astrophysics by virtue of providing all of the fundamental physical properties of stars to high accuracy, with which to test and benchmark theoretical stellar evolution models, and to probe the ages of interesting Galactic populations. In a review of the field, Torres et al. (2012) identified approximately 100 EBs whose parameters have been determined with sufficient accuracy to serve as stringent model benchmarks. Only one

---

<sup>1</sup>Published 2020 September 23: The Astronomical Journal, Volume 160, Number 187, The American Astronomical Society

of these benchmark-grade EBs includes stars still in the pre-main-sequence (PMS) phase of evolution (V1174 Ori; Stassun et al., 2004). In addition, only about 25 of these EBs have measured metallicities, and an even smaller number have independent age constraints (as provided by, e.g., membership in clusters or moving groups), limiting the ability of even these benchmark-grade EBs to serve as the most stringent tests of stellar models. Additional benchmarks for early stellar evolution are critical in building our understanding of stellar formation.

A number of ground and space based exoplanet transit surveys are operating that find EBs in large numbers, either as unintentional false positives or as intentional targets. The KELT survey (Pepper et al., 2007, 2012), has so far identified four bright transiting exoplanets (Siverd et al., 2012; Beatty et al., 2012; Pepper et al., 2012; Collins et al., 2014), in conjunction with a very large number of EBs (e.g. Pepper et al., 2008).

In the course of commissioning the KELT-South telescope we identified the bright, X-ray source HD 54236A as an EB. It is listed in the SIMBAD database as a PMS star and listed in the SACY catalog as possessing Li in its spectrum, a diagnostic of stellar youth. It also possesses a wide common-proper-motion (CPM) companion, HD 54236B, which in turn provides the opportunity for independent checks on key parameters such as system age. Most recently, the Transiting Exoplanet Survey Satellite (*TESS*) observed the HD 54236 system (HD 54236A has TIC ID 238162238 in the *TESS* Input Catalog; Stassun et al., 2019).

At the same time, the advent of *Gaia* has revolutionized our understanding of stellar multiples (e.g., Oelkers & Stassun, 2018), stellar associations (e.g., Oh et al., 2017), and the 3D structure of the solar neighborhood (e.g., Kounkel & Covey, 2019). Indeed, very recent investigations of the full phase-space structure of stars in the solar neighborhood reveal previously unrecognized “stellar strings”, long filamentary groups of young stars that appear to encode the large spiral-arm structures from which they formed (Kounkel et al., 2020). Thus, HD 54236 represents a valuable opportunity to expand the number of known benchmark-grade EBs at young stellar ages, and to test recent suggestions of young “stellar strings” in the solar neighborhood.

In §4.1.1 we describe the overall context of the HD 54236 system, including the presence of HD 54236B as a known, wide CPM tertiary. In §4.2 we present the photometric observations and the spectroscopic observations obtained for the system used to identify HD 54236A as a previously unknown EB, and to determine the basic physical properties of the stellar components. In §4.3 we present the results of our analysis, including orbital solutions, light curve extracted stellar parameters including temperature and radius estimates for both components in the EB, SED modeling and resultant measurement of the stellar masses, and determination of the system age through consideration of the lithium abundances and the Ca II H&K activity. Finally, in §4.4 we consider the membership of HD 54236 in relation to a newly discovered “stellar string”, Theia 301, which itself is related to the AB Dor moving group through common membership be-

tween their filamentary stars. We conclude in §4.5 with a brief summary of our findings.

### 4.1.1 The HD 54236 System

HD 54236A is a  $V=9.26$  object in the constellation Puppis. It was identified as a member of a common proper motion binary in the first CCDM catalog (Soderblom et al., 1993). It is also listed as a visual binary in the Washington Visual Double Stars catalog (Mason et al., 2001). It was identified as a possible pre-main sequence (PMS) object from the SACY survey (Torres et al., 2006): first through its detection as a strong X-ray source, and then through Li observed in its spectrum. Torres et al. (2006) classified HD 54236A as spectral type G0V, and HD 54236B as spectral type K7V.

The total proper motion is  $17.25 \pm 0.22$  mas yr<sup>-1</sup> for both HD 54236 A and B (values from the Gaia archive Gaia Collaboration et al., 2018), and the equivalent width (EW) of the Li line is given in the SACY catalog as 120 mÅ for A and 40 mÅ for B. No uncertainties are provided in the SACY catalog for the Li EW values. Below we report updated precise measurements of the Li EW and abundances for the stars.

HD 54236A is in a fairly crowded part of the sky, and thus all our photometry to date is blended with nearby stars at some level. We will pay special attention in § 4.2.2 to describing the degree of blending in each set of observations. To clarify the environment, Figure 4.1 displays a DSS image of the HD 54236 system, the eclipsing binary HD 54236A and its common proper motion (CPM) companion, HD 54236B at a distance of  $\sim 21$  AU. Surrounding, unrelated field stars are also identified. This observational ecosystem includes:

- HD 54236A ( $V=9.26$ ), spectral type  $\sim G0$ , which is the principal object of study in this paper and which we identify as an eclipsing binary.
- HD 54236B, which is 6.5" south of HD 54236A and is  $V=13.2$ , spectral type  $\sim K7$ . It is a common proper-motion companion of HD 54236A, and we confirm below that it shares the systemic radial velocity of HD 52236A also.
- The bright star HD 54262, which is 54" east of HD 54236A and is  $V=9.31$ . Based on its reported proper motion of  $\mu_\alpha = -55.06 \pm 0.06$  mas yr<sup>-1</sup> and  $\mu_\delta = -1.36 \pm 0.06$  mas yr<sup>-1</sup>, compared to the proper motion of the HD 54236 system of  $\mu_\alpha = -8.01 \pm 0.06$  mas yr<sup>-1</sup> and  $\mu_\delta = -15.28 \pm 0.05$  mas yr<sup>-1</sup> (Gaia), it appears certain that HD 54262 is not associated with the HD 54236 system.
- A very distant ( $\sim 3529$  pc; Gaia Collaboration et al., 2018) and faint star ( $V = 14.6$ ) that is 7.4" to the north of HD 54236A (TIC 767642478) is not physically associated with the HD 54236 system.

**Figure 4.1** Digitized Sky Survey Image of Tertiary HD-54236

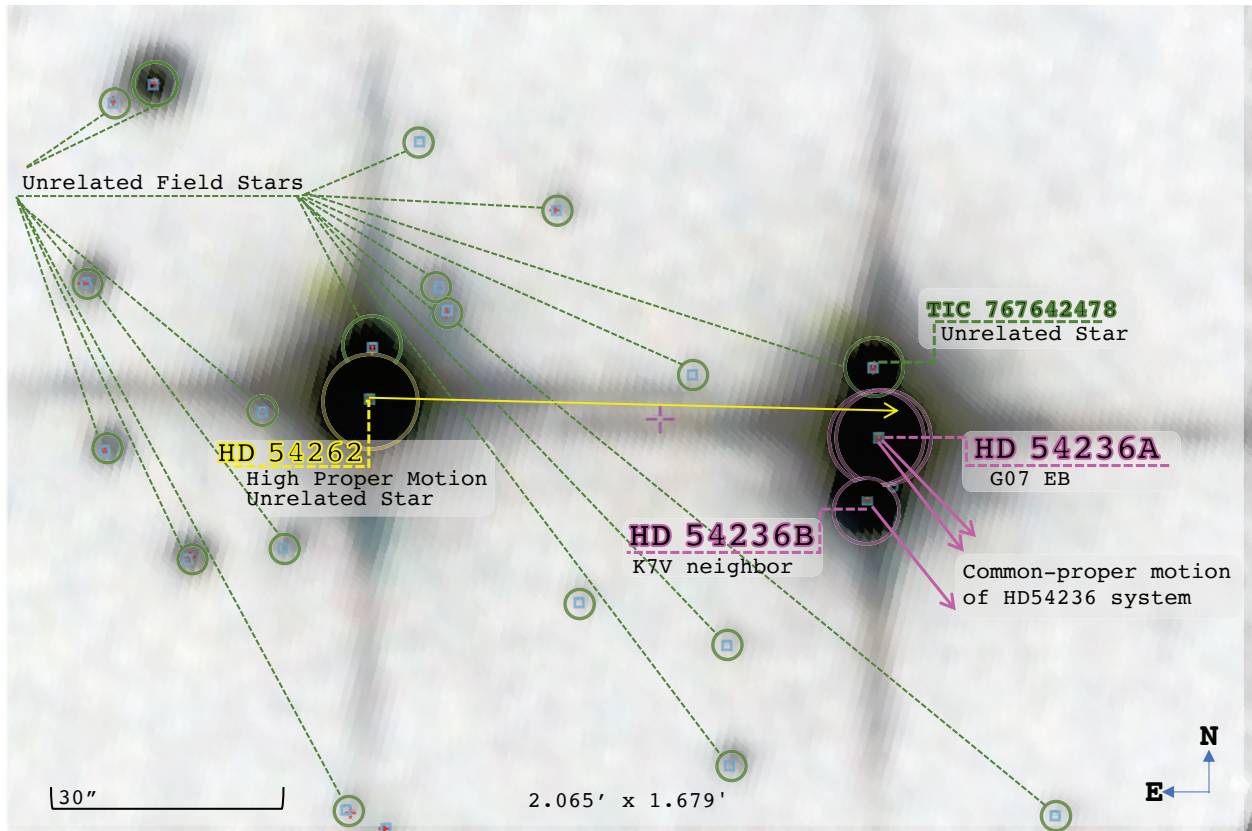


Figure 4.1: DSS image of the HD 54236 tertiary system and its common-proper-motion is highlighted in fuchsia. The tertiary system includes HD 54236A (the eclipsing binary), and HD 54236B, the CPM tertiary member  $\sim 6.5''$  south of HD 54236A. Surrounding, unrelated stars (like TIC 767642478, the distant faint star to the north) are shown in green. HD 54262, an unrelated high proper motion star to the east is highlighted in yellow.

Thus, to our knowledge, the HD 54236 system physically comprises three stars: HD 54236A which we identify below as an eclipsing binary (two stars, unresolved) and HD 54236B as a wide CPM tertiary companion that is visually resolved with a separation from HD 54236A of  $6.5''$ .

## 4.2 Data

### 4.2.1 Photometric Observations

#### 4.2.1.1 KELT-South Photometry

The Kilodegree Extremely Little Telescope-South (KELT-South) is a dedicated exoplanet transit telescope located at the Sutherland observing station of the South African Astronomical Observatory (SAAO). The telescope, hardware, and the primary exoplanet survey is described in Pepper

et al. (2012). The KELT observations are taken with a Kodak Wratten #8 red-pass filter, resembling a widened Johnson-Cousins  $R$ -band.

KELT-South conducted a commissioning run from Jan 4, 2010, to Feb 19 2010. During that run, KELT-South continuously observed a field centered at  $\alpha = 08:16:00$ ,  $\delta = -54:00:00$ , with repeated 30 s exposures. After removal of poor-quality images, we have a total of 3,041 images across 29 individual nights. We generated relative photometry from flat-fielded images using a modified version of the ISIS image subtraction package (see also Alard & Lupton, 1998; Alard, 2000; Hartmann et al., 2004), in combination with point-spread function fitting using the stand-alone DAOPHOT II (Stetson, 1987, 1990) package, and the SExtractor program (Bertin & Arnouts, 1996). A more complete explanation of our pipeline procedures, and the algorithms, are provided in Siverd et al. (2012).

One of the transit candidates was HD 54236A. Although the depth and out-of-eclipse variation of the lightcurve indicated that the target was unlikely to be a transiting planet, the prospect that it represented a bright PMS eclipsing binary prompted us to gather additional data of this target. The KELT light curve of HD 54236A is shown in Fig. 4.2.1.1.

**Figure 4.2** Phase Folded KELT Lightcurve of HD54236

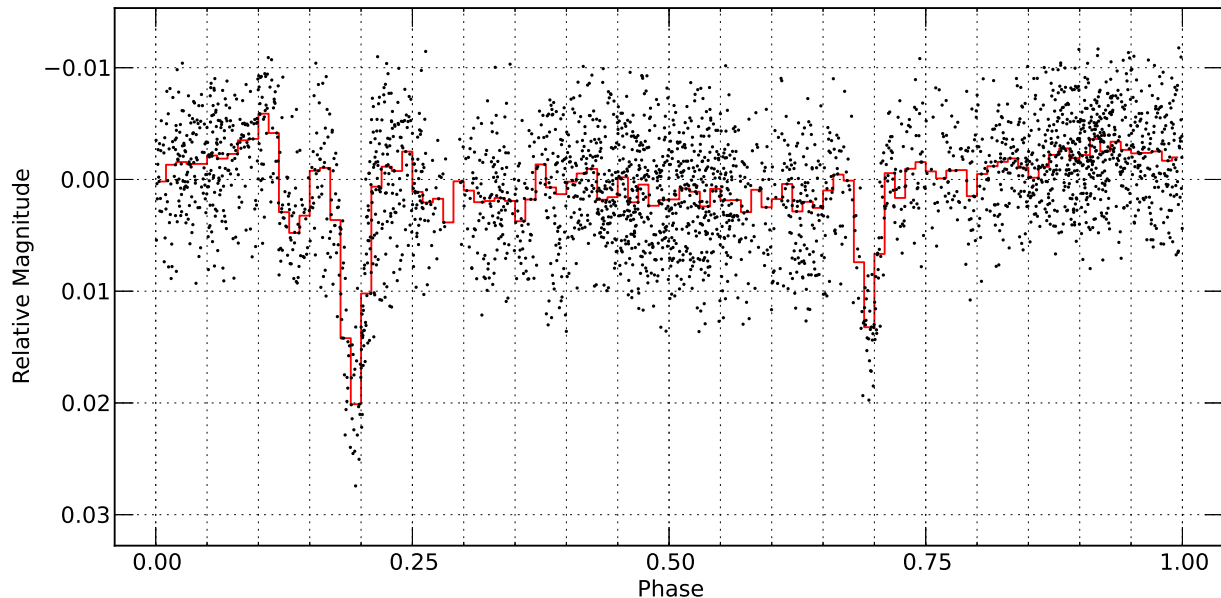


Figure 4.2: Phase-folded lightcurve of HD 54236A from KELT. Small symbols represent individual measurements, red lines represent the binned light curve.

Because of the very wide-field nature of the KELT observing setup, with the accompanying large pixel scale (23" per pixel), the KELT lightcurve of HD 54236A (Fig. 4.2.1.1) is blended with all of the other stars identified in Figure 4.1. The largest component of blended flux comes from HD

54262, which is about 0.33 mag fainter than HD 54236A. Therefore, the eclipse depths seen by KELT are at least 40% shallower than the true depths.

An initial periodicity analysis yielded a most likely orbital period of  $\sim 2.4$  d. In addition, there is an out-of-eclipse variation of a nearly sinusoidal morphology in the KELT light curve with a best-fit period of 2.3955 d, i.e., slightly shorter period than the orbital (eclipse) period. A more detailed examination of the out-of-eclipse variations is provided by the *TESS* light curve (see below).

#### 4.2.1.2 PEST Photometry

One of the partners of the KELT-South survey is the Perth Exoplanet Survey Telescope (PEST), operated by T.G. Tan. PEST consists of a 12" Meade LX200 SCT f/10 telescope, with a focal reducer yielding f/5. The camera is an SBIG ST-8XME, with 1.2 arcsec/pixel.

PEST observed HD 54236A on the night of April 25, 2012, for 119 minutes around the predicted time of primary transit in the Cousins *R*-band, although the ephemeris was poor given the elapsed time between the original observations and the PEST observations (over 2 years). The observations caught the last hour of the primary eclipse egress plus an hour after the eclipse. This light curve is more pure than the discovery KELT light curve in that it excludes light contamination from HD 54262. The PEST light curve does however still include light contamination from the faint visual companion HD 54236B. The raw photometry of the combined HD 54236A/B system was extracted using the C-Munipack software package<sup>2</sup> (written by David Motl) to perform aperture photometry. Relative photometry was derived using a set of three nearby comparison stars via a custom-written program.

The PEST light curve is shown in Figure 4.3, together with the KELT data scaled by a factor of 3 in flux to account for the additional dilution of the KELT data by the high proper motion bright star HD 54262. The addition of the PEST photometry allowed us to refine the orbital period from the KELT data because of the expanded time baseline.

#### 4.2.1.3 TESS Photometry

*TESS* observed HD 54236 (TIC 238162238) in Sectors 6, 7, and 8 from December 15th, 2018, to February 27th, 2019. The 2-minute cadence light curves were processed using the Lightkurve Python module (Lightkurve Collaboration et al., 2018). We extracted the light curves using the optimized aperture selected by the Science Processing Operations Center (SPOC) pipeline. The mask was chosen to avoid the high proper motion star to the west, HD 54262, from blending the

---

<sup>2</sup><http://c-munipack.sourceforge.net/>

**Figure 4.3** Phase Folded KELT Lightcurve of HD54236 Overfitted With PEST Follow-Up

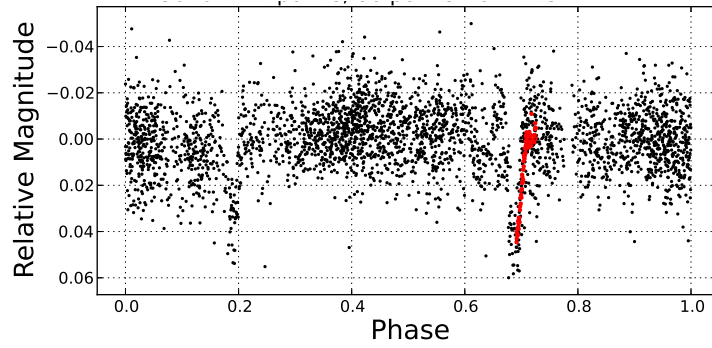


Figure 4.3: Phase-folded lightcurve of HD 54236A from KELT (*black points*) with the follow-up data from PEST over-plotted (*red points*). Since the KELT data includes the flux from the unrelated high proper motion star HD 54262, the KELT data are multiplied by a factor of 3 to match the egress slope from the PEST data.

photometry of HD 54236 (see Figure 4.4). The tertiary star, HD 54236B, remains blended but as it contributes only 2.5% of the flux we do not attempt to correct for it.

**Figure 4.4** TESS Sectors 6, 7, 8 Optimal SPOC Apertures

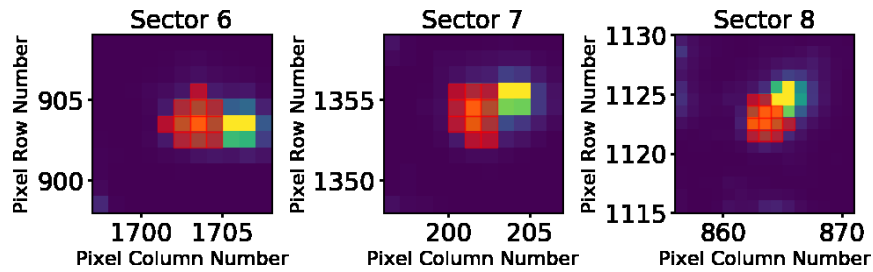


Figure 4.4: *TESS* Target Pixel File cutouts of HD 54236 for Sectors 6, 7, and 8. The red aperture mask is the optimal aperture from the SPOC pipeline, chosen to avoid the distant faint star to the north, TIC 767642477, from blending the photometry.

To estimate the background, we required a brightness threshold such that the pixels in the Target Pixel File that are 0.1% times the standard deviation below the overall median flux of pixels in the selected aperture. We then subtracted the background from our source signal and normalized by the median flux.

To remove long-term trends and to assist with normalization of the flux baselines between sectors and satellite downlink times, we utilized a Biweighted Midcorrelation filter (via the Wotan package; Hippke et al. 2019). We chose a window size of 3 times the  $\sim 2.4$  d period to ensure at least 3 transits are included in each window and will not be overfitted by the smoothing function. The long-term detrended light curve is shown in Figure 4.5.

**Figure 4.5** TESS Photometry Sectors 6, 7, 8

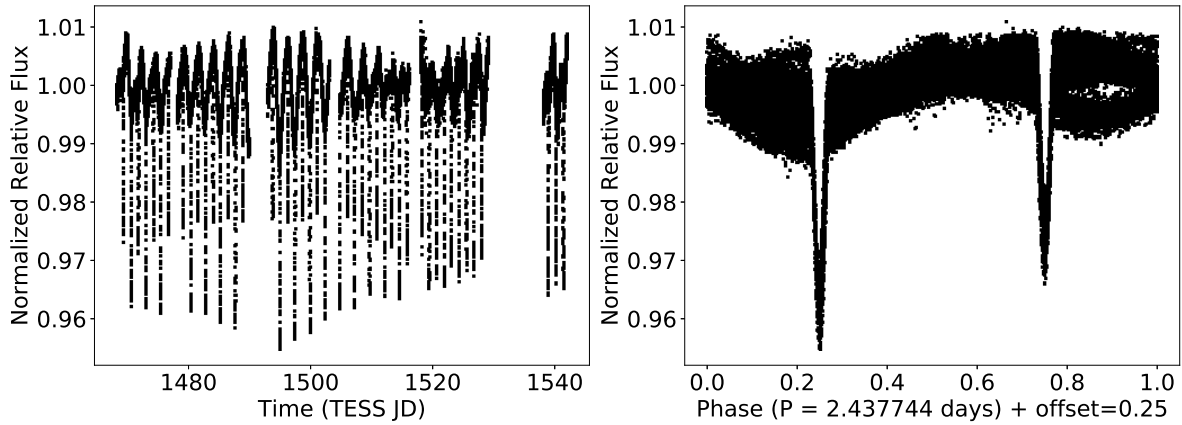


Figure 4.5: TESS Photometry **Left:** TESS light curve of HD 54236 in Sectors 6, 7, and 8. **Right:** Phase-folded TESS light curve.

We then utilized the Astropy implementation of the Box-fitting Least Squares (BLS) algorithm to estimate the period of the evident out-of-transit variations. We used a period range from 1.5 to 11 d with 10000 steps in frequency and a transit duration range of 1 to 24 hr. In Figure 4.6, we focused on a region of the BLS periodogram centered on 2.43 d and are able to identify the orbital period of 2.4377 d along with another prominent periodic feature corresponding to a period of 2.3782 d, which we attribute to the rotational period of one or both of the stars in the EB.

**Figure 4.6** Box Least Squares Periodicity Analysis

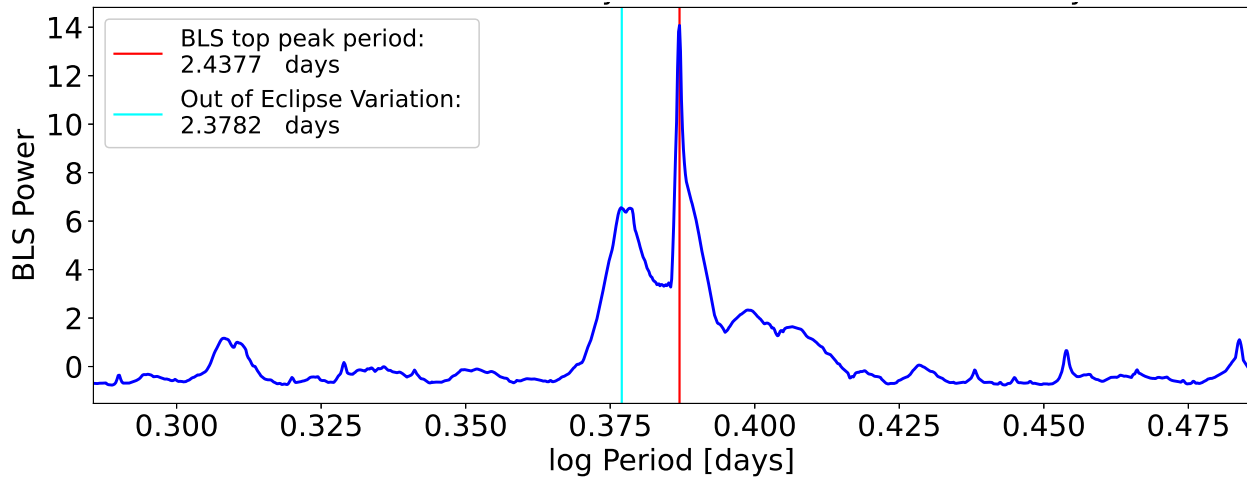


Figure 4.6: BLS periodogram, showing the most prominent periodic features, corresponding to the eclipse period but also showing a similar but different period of 2.3782 d which we attribute to the stellar rotation period (see the text).

To remove this out-of-eclipse variation, we then used a 24-hr window for our smoothing func-



tion. In Figure 4.7, we show the first 10 days of our *TESS* light curve with the trend line that is fit to the flux baseline in red. Since the Biweighted Midcorrelation filter is median-based, it is less sensitive to outliers and ignores the transit events. In Figure 4.5, we show the final phase-folded *TESS* light curve on the orbital period estimated above from the *TESS* light curve. We report a final system ephemeris combining all of the available light curve data in Section 4.3.1.

**Figure 4.7** Box Least Squares Periodicity Analysis

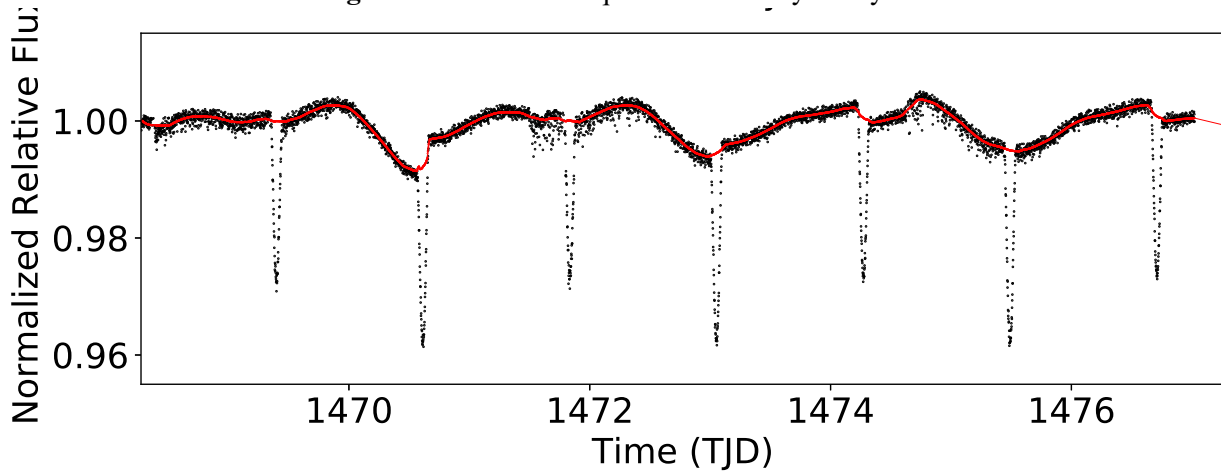


Figure 4.7: The first 10 days of the *TESS* light curve spanning Sectors 6 to 8, shown in *TESS* Julian Days (TJD). The black points are the *TESS* data and the red line is the Biweighted Midcorrelation filter applied to the flux baseline. We used a window size of 6 hours which equals to 3 times the transit duration reported by BLS.

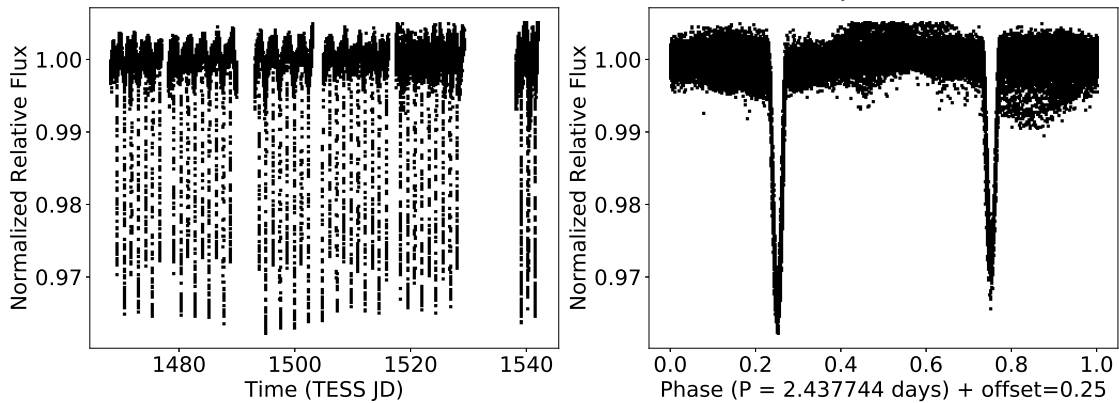


Figure 4.8: The phase folded *TESS* light curve that was smoothed using a Biweighted Midcorrelation filter as described in §4.2.1.3. The out-of-transit variations seen in Figure 4.6 are removed in these data.

## 4.2.2 Spectroscopic Observations

Spectroscopic Observations of the HD 54236 were acquired from the Wide Field Spectrograph (WiFeS) and echelle spectrograph on the ANU 2.3 m telescope from the Australian National University<sup>3</sup>, and, the Goodman High Throughput Spectrograph (Clemens et al., 2004), installed on the  $f/16.6$  Nasmyth platform of the 4.1 m SOUTHERN Astrophysical Research (SOAR) telescope. In what follows, each instrument and the analysis of its spectroscopic observations are described.

## 4.2.3 ANU 2.3m Spectroscopy

We obtained a single 100-sec exposure of HD 54236A using WiFeS (Dopita et al., 2007) on the ANU 2.3 m telescope at Siding Spring Observatory, Australia. WiFeS is an image slicer integral field spectrograph, where the B3000 grating and the RT560 dichroic were selected for our observations, giving the spectral coverage of 3500–6000Å at a resolution of  $\lambda/\Delta\lambda = 3000$ . The object spectrum was extracted and reduced with the IRAF<sup>4</sup> packages CCDPROC and KPNOSLIT, with the wavelength solution provided by a Ne-Ar arc lamp exposure taken on the same night. The spectrum is flux calibrated against exposures of spectrophotometric standard stars from Hamuy et al. (1994), employing techniques described in Bessell (1999). The resulting flux-calibrated spectrum had signal-to-noise of  $S/N = 300$  per resolution element.

The reduced object spectrum was fitted to a grid of synthetic spectra from Munari et al. (2005), spaced at intervals of 100 K in  $T_{\text{eff}}$ , 0.5 dex in  $\log g$ , 0.5 dex in  $[\text{Fe}/\text{H}]$ , and 0.02 magnitudes in  $E(B - V)$ . Discrepancies between the object spectrum and the synthetic template are largely due to differences in the flux calibration between them but prevent no analytical obstacle as spectral matching is done based on spectral features, rather than its overall shape. We weighted regions sensitive to  $\log g$  variations preferentially, including the Balmer jump, the MgH feature at 4800Å, and the Mg b triplet at 5170Å. Details of the data reduction and spectral fitting process can be found in § 3.2.1 of Penev et al. (2013). The resulting derived atmospheric parameters for HD-54236A are  $T_{\text{eff}} = 6350 \pm 100$  K,  $\log g = 5.0 \pm 0.3$ , and  $[\text{Fe}/\text{H}] = -0.5 \pm 0.5$  (see Figure 4.9, top panel). Note that this analysis assumes that HD 54236A is a single star, when in fact it is a binary. We return to a discussion of this in § 4.3.5.4.

We also observed the fainter CPM tertiary companion star HD 54236B. The analysis is displayed, as for HD 54236A, in Figure 4.9 bottom panel, and yields the following stellar parameters:  $T_{\text{eff}} = 4400 \pm 200$ K,  $\log g = 4.8 \pm 0.35$ ,  $[\text{Fe}/\text{H}] = -0.5 \pm 0.44$  (Bayliss et al., 2013).

<sup>3</sup><http://rsaa.anu.edu.au/observatories/siding-spring-observatory>

<sup>4</sup>IRAF is distributed by the National Optical Astronomy Observatory, which is operated by the Association of Universities for Research in Astronomy (AURA) under cooperative agreement with the National Science Foundation.

**Figure 4.9** Spectroscopic Analysis of Trinary System HD-54236

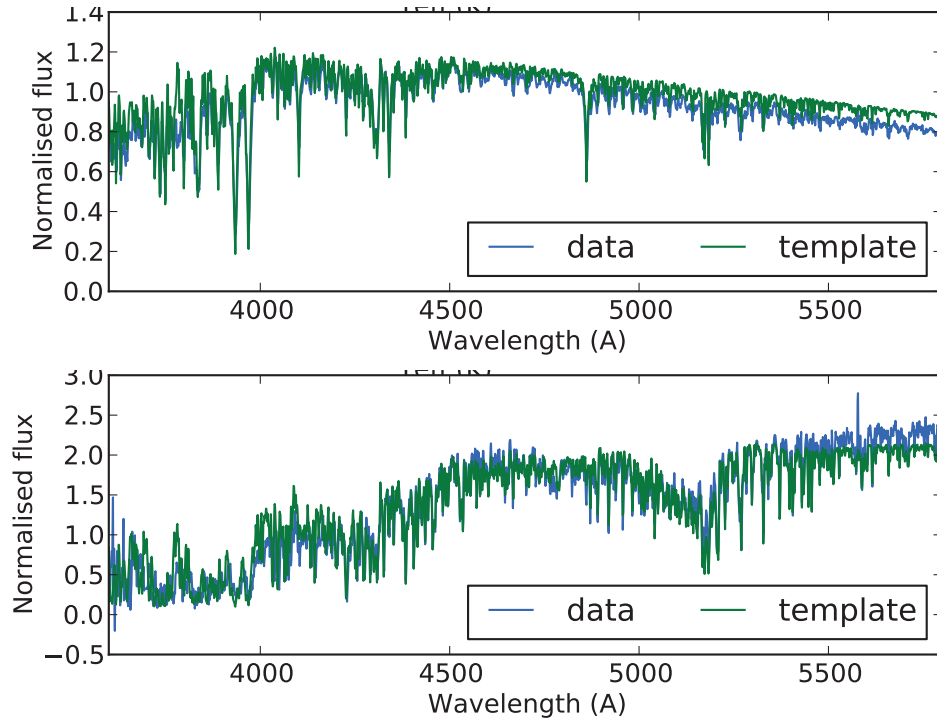


Figure 4.9: **Top:** Spectral analysis of the stellar parameters of HD 54236A, the eclipsing binary. **Bottom:** Spectral analysis of the stellar parameters of the tertiary member, HD 54236B. The observed spectra for both HD 54236A and HD 54236B are shown in blue, while their respective templates modeled in green. Discrepancies between the target spectra and its template are largely due to differences in flux calibration, however, spectral matching is done based on spectral features rather than overall shape.

In addition, from this spectrum we have verified the Li EW of HD 54236A reported by SACY (120 mÅ). We obtain an EW of  $140 \pm 20$  mÅ for the Li line at 6708 Å, representing the blended EW of both stars in the HD 54236 EB.

The WiFeS spectrograph was also used to measure the radial velocities of the eclipsing stars. One spectrum was obtained on HJD 2456104.838 using WiFeS at medium resolution ( $\lambda/\Delta\lambda = 7000$ ), where both components of the spectroscopic binary were resolved. The observation and data analysis process follows Penev et al. (2013). The velocities were measured via cross correlation as described in the next section, and are reported along with the full set of velocities described below in Table 4.1.

#### 4.2.4 High-resolution Spectroscopy: Radial Velocities

Nine high-resolution observations of HD 54236A were obtained using the ANU 2.3 m echelle spectrograph, at a resolution of  $\lambda/\Delta\lambda \approx 23000$ , velocity dispersion of  $4.0 \text{ km s}^{-1} \text{ pixel}^{-1}$ , in the

spectral range 4200–6700Å, over 20 echelle orders. The data was reduced with the IRAF package CCDPROC, extracted and normalized using ONEDSPEX. The wavelength solution was provided by Th-Ar arc lamp exposures that bracketed each science exposure. A standard 950 sec exposure of the target yields a signal-to-noise of  $S/N = 40$  per resolution element. The instrument setup, observations, and data reduction process are detailed in Zhou et al. (2014).

We cross-correlated the object spectra against a series of radial velocity standard star spectra taken during twilight each night. The cross-correlation peaks for the two spectroscopic components of the object were resolved in the observations, we were therefore able to extract radial velocities for both components in each observation by fitting Gaussians to the two cross-correlation peaks. We take the stronger peak to represent the (more massive) primary component. An example cross-correlation function (CCF) for the observation on HJD 2456057.93945 is shown in Figure 4.10.

**Figure 4.10** Cross Correlation Radial Velocity Extraction HD-54236

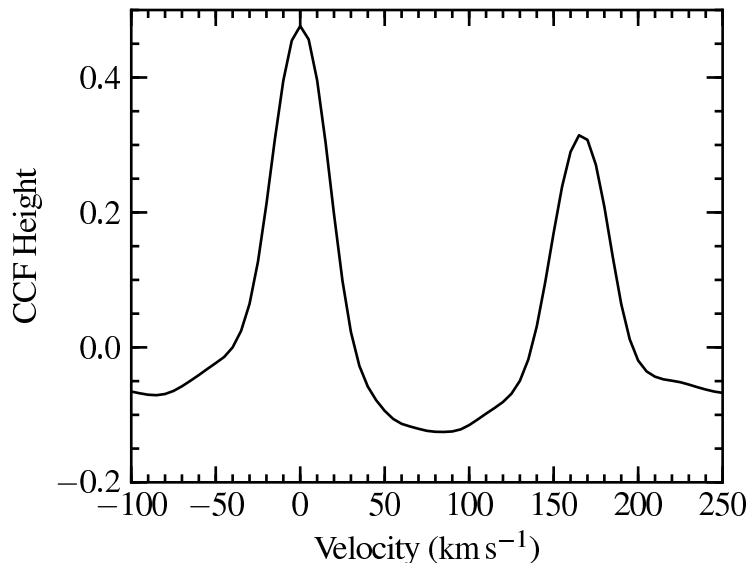


Figure 4.10: Cross-correlation function for the spectrum taken on HJD 2456057.93945226, with the ANU 2.3 m echelle at  $R = 23000$ . The CCF shown is the average CCF of the cross correlations from all echelle orders, excluding those with very low cross-correlation heights. The cross-correlations are performed against RV standard star exposures taken on the same night. For clarity, the highest peak (presumed to correspond to higher mass, primary component in the eclipsing binary, has been shifted in this figure to be at  $0 \text{ km s}^{-1}$ .

The radial velocity is calculated as the mean over all orders not affected by telluric contamination, weighted by their respective signal-to-noise ratio; the scatter in the measurements over the orders gives the error in the radial velocity measurement for that epoch. The complete set of primary and secondary radial velocities determined from these observations and are summarized in Table 4.1.

Table 4.1: RV Observations of HD 54236 A

HJD (UTC)	Primary RV (km s <sup>-1</sup> )	Secondary RV (km s <sup>-1</sup> )	Source
2456057.93945	-88.7 ± 1.3	76.9 ± 0.9	ANU 2.3m
2456057.95085	-90.6 ± 1.4	78.9 ± 1.1	ANU 2.3m
2456058.92243	21.7 ± 1.2	-46.3 ± 1.1	ANU 2.3m
2456059.92704	6.6 ± 1.5	-35.2 ± 0.8	ANU 2.3m
2456061.96015	84.9 ± 1.4	-109.1 ± 1.1	ANU 2.3m
2456086.48771	63.4 ± 1.0	-90.4 ± 1.0	SOAR 4.1m
2456087.85052	-55.9 ± 2.0	36.9 ± 1.9	ANU 2.3m
2456087.86683	-54.3 ± 1.6	30.1 ± 2.7	ANU 2.3m
2456088.84221	75.9 ± 1.2	-102.7 ± 1.0	ANU 2.3m
2456088.85501	73.4 ± 1.2	-101.7 ± 1.1	ANU 2.3m
2456104.83853	-68.8 ± 1.1	61.3 ± 1.6	ANU 2.3m

#### 4.2.4.1 SOAR Spectroscopy

HD 54236 A & B were observed on UT 20120605 and UT 20120607 using the Goodman High Throughput Spectrograph (Clemens et al., 2004), installed on the f/16.6 Nasmyth platform of the 4.1m SOUTHERN Astrophysical Research (SOAR) telescope. The spectrograph used the 1200 l/mm grating in M5 mode, a 0.46-arcsecond wide slit, a GG-495 blue-blocking filter, imaged onto a 4096×4096 Fairchild CCD detector, having square 15μm pixels (0.15 arcsecs/pixel). This setup yields a central wavelength of  $\simeq 6890\text{\AA}$ , a wavelength range of  $\simeq 6275\text{--}7495\text{\AA}$ , a spectral dispersion of 0.304Å per pixel and a three-pixel resolving power of  $R \simeq 7000$  at 6400Å. The FWHM of cross-correlated CuHeAr arc lines is 4.7279 pixels or 62.58 km s<sup>-1</sup>. Using this setup, HD 54236 A and B were separately observed for exposure times of 300- and 900-seconds, respectively, on UT 20120605, and 300- and 600-seconds, respectively, on UT 20120607, resulting in spectra having maximum S/N near to H $\alpha$  of  $\simeq 350$  for HD 54236A and 100 for HD 54236B.

For each target, we measured heliocentric radial velocities and Li I 6708Å equivalent widths. CCD instrumental effect removal (such as de-biasing and flat-fielding), as well as the extraction of wavelength calibrated spectra, was performed using standard IRAF procedures. Heliocentric radial velocities were determined relative to the International Astronomical Union standard stars HR 6468, HR 6859, HD 120223 and HD 126053. Cross-correlation of the velocity standards against one other shows that the zero-point relative to the standard system is accurate to  $\sim 0.2$  km s<sup>-1</sup>. The CCF is the average from all echelle orders, excluding those with very low cross-correlation heights and are performed against RV standard star exposures taken on the same night. The radial velocity standard stars on these nights shows that the system is stable to  $\simeq 0.5$  km s<sup>-1</sup> over the course of the night.

The radial velocities for the eclipsing components of HD 54236A are reported with the other radial velocity measurements in Table 4.1. For the single star HD 54236B, we obtain a systemic velocity of  $-12.0 \pm 0.3 \text{ km s}^{-1}$ . As shown below, this velocity is consistent with the systemic velocity of the HD 54236A eclipsing binary system.

In order to measure the EW of the Li I 6708 Å resonance lines, the Goodman spectra were first trimmed to 6620–6750 Å and normalized using a 7th-order spline function fit to the continuum. Equivalent widths were measured using both Gaussian fits and direct integration to check for consistency. The region of the spectrum around the Li line is shown in Figure 4.11. The measured Li EWs for the eclipsing stars in HD 54236A are  $66 \pm 6 \text{ mÅ}$  for the primary star and  $47 \pm 5 \text{ mÅ}$  for the secondary star. Note that these are the directly observed EWs; below we correct these EWs for the mutual dilution of the two stars’ spectra when we transform these EWs into Li abundances.

**Figure 4.11** Lithium Absorption Lines HD54236

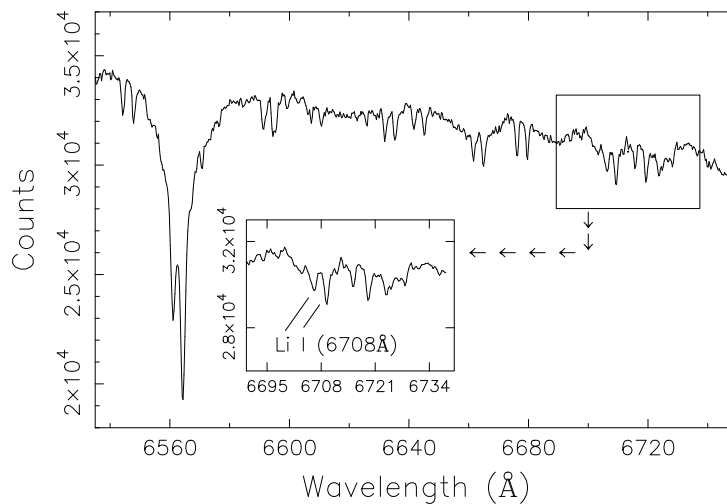


Figure 4.11: Region of the Li line from the SOAR spectrum of HD54236, taken June 7, 2012.

### 4.3 Results

With the above data in hand for the HD 54236 system, including photometric light curves and spectroscopic measurements of the component radial velocities and individual stellar spectra, in this section we determine the orbital parameters as well as constraints on the system age from consideration of the Li absorption and Ca HK emission. To remind the reader, the system comprises three stars, two eclipsing components in HD 54236A and a single CPM star in HD 54236B.

### 4.3.1 System Ephemeris

Analysis of all of the available light curve and radial-velocity data together (see §4.2.1–4.2.2), including in particular the KELT, PEST, and the exquisitely precise *TESS* light curves, spanning a total time baseline of more than 10 yr, leads to the final orbital ephemeris determination of  $P_{\text{orb}} = 2.43742 \pm 0.00014$  d and  $\text{HJD}_0 = 2455199.5980 \pm 0.0021$ .

### 4.3.2 Orbit Solution

We performed a simultaneous Keplerian orbit fit to the radial velocity measurements of the two eclipsing components of HD 54236A. We fit the ANU and SOAR radial velocities simultaneously, without attempting to introduce any possible systematic offset between the two. Thus, in total we fit 11 primary radial velocities and 11 secondary radial velocities which are listed in Table 4.1. The resulting orbit solution is shown in Figure 4.3.2 and summarized in Table 4.2. The orbital eccentricity is consistent with zero, which is not surprising given the very short orbital period, hence for the remainder of our analysis we assume a circular orbit ( $e \equiv 0$ ).

**Table 4.2** HD-54236 A Orbital Solution

Table 4.2: Orbital Solution of HD 54236 A

$q$	$e$	$v_\gamma$	$a \sin i$
$0.9132 \pm 0.012$	$0.009 \pm 0.008$	$-10.0 \pm 0.5 \text{ km s}^{-1}$	$9.810 \pm 0.080 R_\odot$

**Figure 4.12** HD-54236 A Radial Velocity Solution

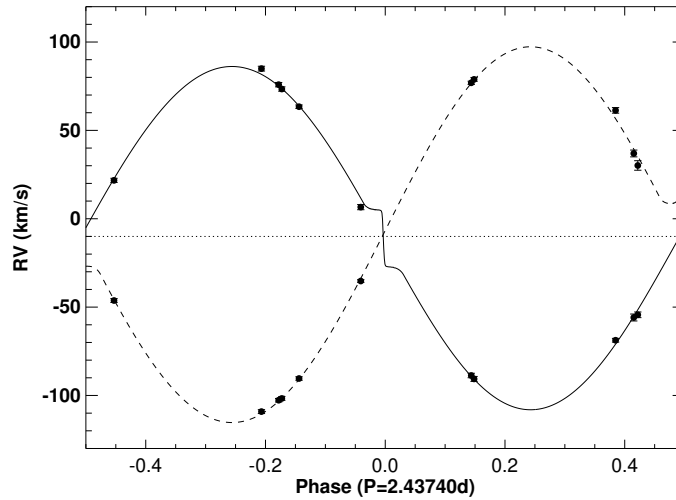


Figure 4.12: RV solution for HD 54236A: The primary is modeled with the solid line, and the secondary with the dashed line.

### 4.3.3 PHOEBE Light Curve Model

The PHysics of Eclipsing BinariEs, (Prsa et al., 2011; Prša et al., 2016) commonly referred to as PHOEBE is an EB modeling code which enhances upon the Wilson-Devinney (Wilson & Devinney, 1971) method with improved model fidelity. Functions are available through PHOEBE that provide generation of highly characterized synthetic light curves given orbital and stellar parameters.

We invoke PHOEBE to produce synthetic light curves for model fitting to our detrended TESS light curve, adopting the orbital parameters determined from the orbit solution (Section 4.3.2), such that the principal fitting parameters are the ratio of effective temperatures ( $T_{\text{ratio}}$ ), the sum of the stellar radii ( $R_{\text{sum}}$ ), and the orbital inclination ( $i$ ). This is appropriate given the circular orbit, where to first order  $T_{\text{ratio}}$  is set by the relative eclipse depths and  $R_{\text{sum}}$  is set by the eclipse durations, moderated by  $i$ .

We use a Genetic Algorithm (GA) to converge to a model light curve solution. Previous work (see, e.g., Metcalfe, 1999) has shown GA techniques to be robust for model fitting eclipsing binary light curves and thus inspired a modified version we utilize here. For computational efficiency we downsample the TESS 2-min cadence light curve by a factor of 15 and run PHOEBE using the Legacy backend, which is markedly faster.

The fitting algorithm starts with the generation of an initial random population of 500 model parameter sets [ $T_{\text{ratio}}$ ,  $R_{\text{sum}}$ ,  $i$ ] in our parameter space, each of which is encoded as a single object representation referred to as a gene. For each model we set the effective temperatures by apportioning the spectroscopically determined average (6350K) according to the flux-weighted sum of the two stars and the current iteration of  $T_{\text{ratio}}$ . For each gene a corresponding model light curve is computed in PHOEBE, and the  $\chi^2$  between the observed and model fluxes is calculated.

To thoroughly explore our parameter space we propagate this population over the course of 20 generations resulting in a total sample of 10,000 models. Iteration of genes from one generation (parent) to the next (child) is done using single point crossover. The members of each parent generation used in the crossover are chosen via roulette wheel until re-population is achieved. The probability of each selection is weighted by the reciprocal of the  $\chi^2$  goodness-of-fit metric. To help maintain diversity between generations (i.e., to avoid local minima) we introduce a 10% chance for random mutation within the constraints for the parameters at inception.

After sampling is complete we discard the first 15 generations in order to prevent the lack of convergence in previous generations from contaminating our result. The fitted parameter distributions of the cleaned sample of 2500 models is illustrated in the corner plot (Fig. 4.13). The distributions are gaussian-like in shape with well determined modal values. Thus, we determined the converged solutions as the mean values of these distributions and the uncertainties as the standard



deviations. The final converged model is shown over our TESS light curve in Figure 4.14 as well as the residuals between the two. There is evidence of some minor systematics in the residuals of the primary eclipse with an amplitude of  $\sim 0.003$  relative flux units, however this is only  $\lesssim 1\%$  of the eclipse depth of  $\sim 0.035$  relative flux units, which we deem acceptable.

We use the fitted  $T_{\text{ratio}}$  together with the spectroscopically determined flux ratio of 3.0/4.5, and solve Stefan-Boltzmann's Law to obtain  $R_{\text{ratio}}$ , which with the fitted  $R_{\text{sum}}$  yields the final individual radii. Similarly, the fitted  $T_{\text{ratio}}$  together with the final  $R_{\text{ratio}}$  and the flux ratio yields the final individual temperatures. Finally, using the final  $i$  we obtain the stellar masses via the orbit-solution determined  $a \sin i$  and  $q$ .

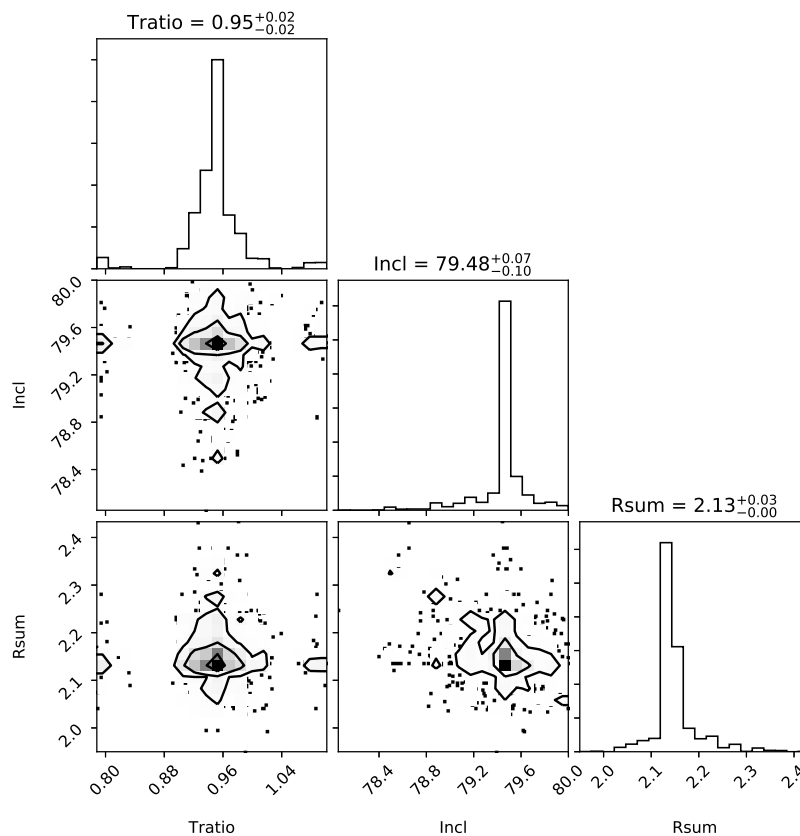


Figure 4.13: Corner plot of fitted parameters for cleaned sample of 2500 model light curves. Values atop distribution are the median values and the 0.16 & 0.84 quantiles.

### 4.3.4 SED Analysis

The radii and effective temperature solutions from the PHOEBE analysis (Table 4.2) were used in Spectral Energy Distribution (SED) modeling, fitting only for extinction and distance. This is done to ensure that our  $T_{\text{eff}}$  solutions correctly reproduce the observed shape of the SED, and

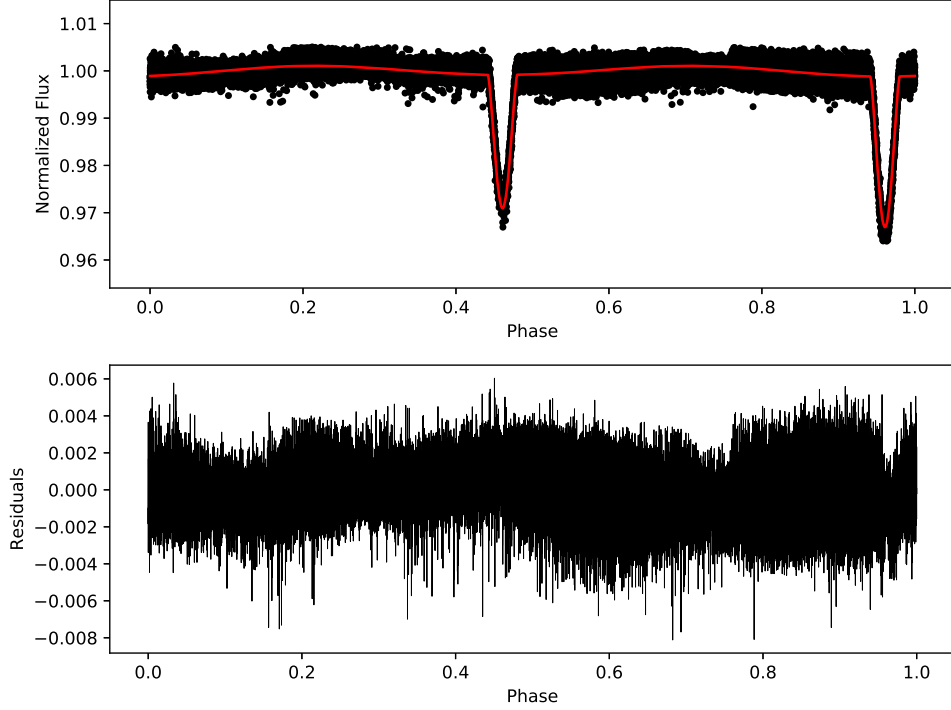


Figure 4.14: Light curve fitting for HD 54236A using GA converged model solution. There remain some small systematics in the residuals in eclipse, the amplitude of which are of order 1% of the eclipse depths. The final stellar parameters from this solution are listed in Table 4.1.

**Table** PHOEBE Fit Parameters and Solutions of HD-54236A

Table 4.3: PHOEBE Fit Parameters and Solutions of HD 54236A

$T_{\text{eff},1}$	$6480 \pm 103 \text{ K}$
$T_{\text{eff},2}$	$6155 \pm 155 \text{ K}$
$R_1$	$1.128 \pm 0.044 R_{\odot}$
$R_2$	$1.021 \pm 0.044 R_{\odot}$
$i$	$79.4 \pm 0.2^{\circ}$
$M_1$	$1.179 \pm 0.029 M_{\odot}$
$M_2$	$1.074 \pm 0.027 M_{\odot}$

that the inferred distance from this analysis corresponds to the known *Gaia* distance. From Figure 4.16 the SED fits for HD 54236A (top) and HD 54236B (bottom) show a very good agreement with our  $T_{\text{eff}}$  determinations. The *Gaia* distance to HD 54236 is  $131.8 \pm 0.5$  pc, the best-fit distance from the SED analysis is in agreement at  $136 \pm 6$  pc, providing a strong validation of the temperatures and radii that we have determined for both stars in the EB.

For the companion star, HD 54236B, the *Gaia* distance was adopted in fitting the SED to solve for the stellar radius. The stellar radius combined with the  $\log g$  yields an estimate for the mass.

### Spectral Energy Distribution: HD54236A, HD54236B

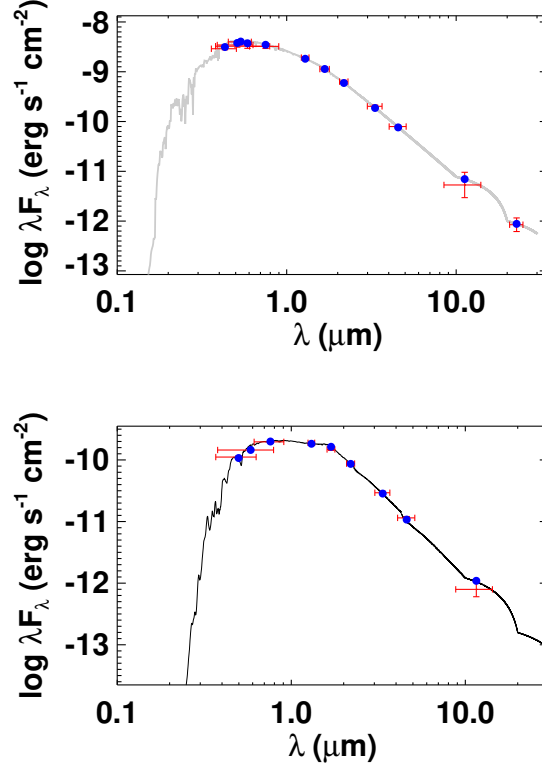


Figure 4.15: *Top*: SED fit of HD 54236A *Bottom*: HD 54236B SED fit. Red symbols are observed broadband fluxes, curves are the best-fit model atmospheres, and blue symbols are the model fluxes for comparison to the observed fluxes.

For the radius we find  $0.65 \pm 0.06 R_{\odot}$  and a mass estimate of  $0.65 \pm 0.11 M_{\odot}$ . These are fully consistent with the empirical relations of Torres et al. (2012) who give a similar but more precise mass estimate of  $0.67 \pm 0.04 M_{\odot}$ .

#### 4.3.5 System Age

In order to establish an age estimate for the HD 54236 system, we consider two commonly used stellar chronometers, namely the abundance of Li and the strength of chromospheric activity in the Ca II H&K lines. While the Ca II H&K activity indicator will be enhanced in the eclipsing pair HD 54236A because of their short orbital period and therefore likely enhanced rotation, we utilize the existence of the wide tertiary companion star, HD 54236B, to obtain a clean estimate of the Ca II H&K activity age for the system. This analysis is carried out through the comparison of Ca II H&K spectral features against those of similar effective temperatures from three different open clusters spanning the range of age estimates covered in 4.3.5.1. Finally, in an at-

tempt to establish association of the system with other nearby stars of similar age, we consider the space motion of the HD 54236 system. For context, in Fig. 4.3.5.3 we show the components of the HD 54236A system in the  $T_{\text{eff}}$ -Radius plane compared to the Yonsei-Yale stellar evolutionary tracks (Yi et al., 2001) for the spectroscopically determined  $[\text{Fe}/\text{H}]$  of  $-0.5$ . We also represent all three stars—the eclipsing components of HD 54236A and the tertiary HD 54236B—in the H-R diagram plane compared to the PMS evolutionary models of Baraffe et al. (1998). All of which suggest an age near the ZAMS or slightly younger, consistent with the other age diagnostics discussed above.

### Spectral Energy Distribution: HD54236A, HD54236B

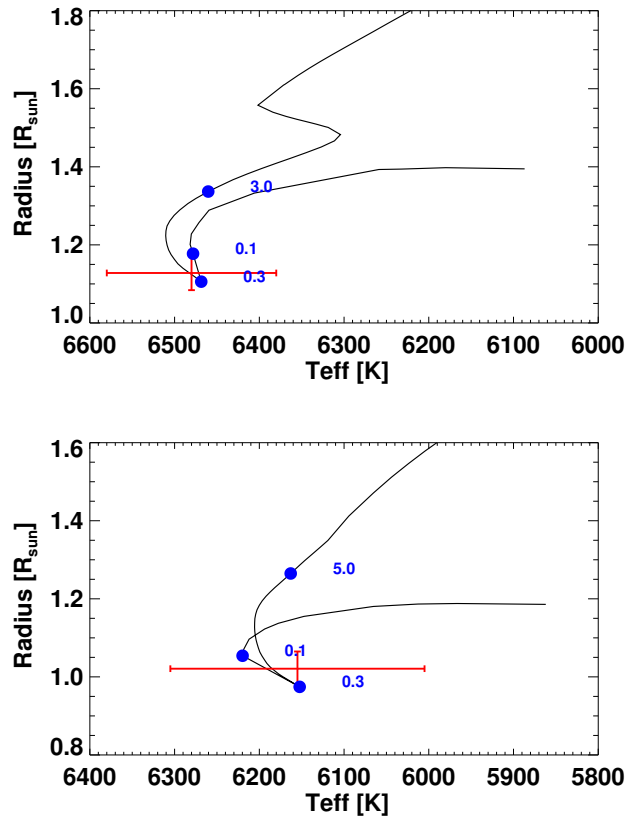


Figure 4.16: *Top:*  $T_{\text{eff}}$ -Radius diagram for the primary star of the HD 54236A system. *Middle:*  $T_{\text{eff}}$ -Radius diagram for the secondary star of the HD 54236A system. Both are in the  $T_{\text{eff}}$  vs Radius plane and show the Yonsei-Yale stellar evolutionary tracks (Yi et al., 2001), which suggest an age for HD 54236A near the ZAMS (which occurs at an age of 300 Myr in these models) and roughly consistent with an age of  $225 \pm 50$  Myr as determined from other age diagnostics.

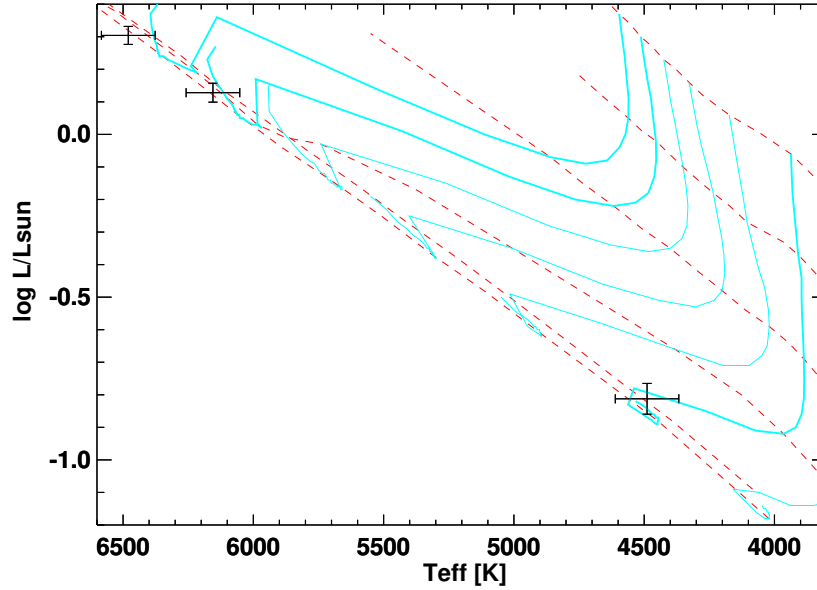


Figure 4.17: H-R diagram showing all three components of the HD 54236 system (black symbols) compared to the PMS evolutionary models of Baraffe et al. (1998); shown are isochrones at ages of 1, 3, 10, 30, 100, and 300 Myr (red dashed lines) and tracks for masses of  $0.6\text{--}1.2 M_{\odot}$  in increments of  $0.1 M_{\odot}$  (blue curves)

#### 4.3.5.1 Lithium

The observed Li EWs for the three stellar components in the HD 54236 system are indicative of a relatively young system age intermediate between the youngest pre-main-sequence clusters and older main sequence clusters. For example, from the analysis of Li EW in young stars of various ages, Aarnio et al. (2008) finds that young stars with K spectral type and ages of  $\sim 50$  Myr have Li EW of  $100\text{--}200 \text{ m}\text{\AA}$ , somewhat larger than what we observe in the HD 54236B star (spectral type late K). Therefore it is likely that the HD 54236 system has an age somewhat older than 50 Myr. To determine the Li inferred age of the system more precisely, we analyzed the observed Li EWs for the three stars in HD 54236 in the context of other young clusters.

First, we corrected the observed EWs for the two eclipsing stars to account for the mutual dilution of the two stars' spectra in our combined light observations.

Based on the stars' final  $T_{\text{eff}}$  values from our PHOEBE modeling and SED fits, we converted the Li EW into Li abundances,  $A(\text{Li})$ , using standard curve-of-growth techniques (Soderblom et al., 1993) and applying a NLTE correction (Carlsson & Stein, 1994).

The sample from Sestito & Randich (2005) contains 22 clusters spanning a range of ages from  $\sim 5\text{-Myr}$  to  $\sim 6\text{--}8 \text{ Myr}$ , for our comparison, we gathered  $A(\text{Li})$  for several of these open clus-

ters ranging in age from 35 Myr to 1.2 Gyr and follow the same curve-of-growth and NLTE correction in our abundance calculation method for the HD 54236 system. The stellar censuses for our comparison clusters shown in 4.18 are as follows, in the young clusters with ages less than  $\sim 100$  Myr: NGC 2547 contains 7 stars, IC 2391 has 6, IC 2602 contains 31 and  $\alpha$  Per contains 39 stars. In the ZAMS clusters, with ages  $\sim 100$  Myr are the Pleiades with its seven sisters, Blanco 1 which consists of 17 stars, and M35 with a total of 27. The intermediate comparison clusters have ages of  $\sim 200$ – $300$  Myr and are represented by NGC 2516, M34 and M7 or NGC 6457 which have 22, 38, and 24 stars respectively. The oldest clusters used for comparison were of ages greater than  $\sim 400$  Myr, these included the UMa Group with 14 stellar members, NGC 6633 with 22 stars, Coma Ber with roughly 40 stars forming its distinctive V shape, Hyades containing 14 stars, and NGC 752, the oldest comparison, having 5 members. The data set used in Sestito & Randich (2005) (and used for comparison in this work) are a collection of independent results from a variety of authors using a degree of models to investigate the evolution of Lithium abundances and their associated timescales.

From visual inspection of Fig. 4.18, it is clear that the three stars'  $A(Li)$  generally follow the trend with  $T_{\text{eff}}$  observed in young clusters with ages of 100–400 Myr. To constrain the likely age more precisely, we calculated the  $\chi^2$  probability of the three stars'  $A(Li)$  agreement with each of the comparison clusters shown in the figure. We obtain the following probabilities for the HD 54236 system Li abundances:  $P(\text{age} < 100 \text{ Myr}) = 0.03$ ,  $P(\text{age} \sim 100 \text{ Myr}) = 0.09$ ,  $P(\text{age} 200\text{--}300 \text{ Myr}) = 0.40$ ,  $P(\text{age} > 300 \text{ Myr}) < 0.01$ . Therefore, statistically the pattern of  $A(Li)$  with  $T_{\text{eff}}$  observed for the three stars in HD 54236 is most consistent with an age of 200–300 Myr. However, a younger age of  $\sim 100$  Myr cannot be entirely ruled out on the basis of the Li abundances alone.

#### 4.3.5.2 Ca H & K

The strength of the emission cores in the H & K lines of Ca II near  $3950\text{\AA}$  are a commonly used tracer of chromospheric activity and thus, through the empirical rotation-activity relationship of FGK dwarfs, can be used as an age indicator. Given the short orbital period of the eclipsing pair in HD 54236A, it is a good assumption that the two stars have tidally interacted and therefore the stars are likely to have their current rotation governed not by the rotation-activity-age relation, but rather by tidal synchronization with the orbit. Indeed, we observe a roughly sinusoidal variation in the eclipsing system light curve at very nearly the orbital period (see § 4.3.1), confirming that the stars likely rotate at very nearly the orbital period due to their close separation. Current rotation-activity-age relationships (in this case the age- $R'_{HK}$  relationship) are based on single-star angular momentum evolution, so this rules out using the HD 54236A system to determine the system age using chromospheric activity measures.

### Equivalent Width of Lithium Abundances of HD-54236

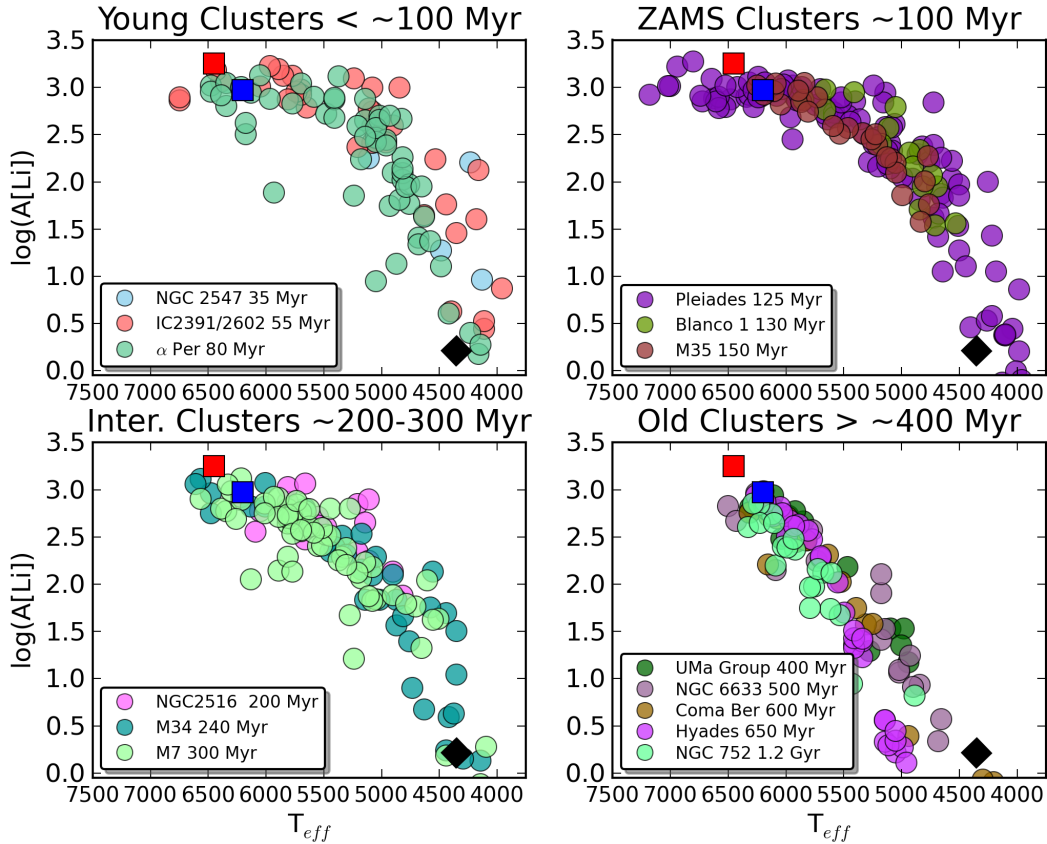


Figure 4.18: Lithium abundance analysis for a range of ages of clusters: Comparison of EW of lithium abundances from the HD 54236 system to several different clusters ranging in age from 35 Myr to 1.2 Gyr (sample clusters and their parameters are from Sestito & Randich, 2005). From these comparisons we can see that the stellar components in the HD 54236 system (shown with red and blue squares for the primary and secondary stars in the eclipsing binary primary HD 54236A) are indicative of a relatively young age: between PMS clusters and older main sequence clusters.

Fortunately, the single K-dwarf star in the system (HD 54236B) *can* be used for this purpose. We utilize the high S/N spectrum obtained with the ANU WiFeS spectrograph. Both because our spectrum was not absolutely flux calibrated and because the late spectral type of HD 54236B places it beyond the calibration of existing age-activity relationships (e.g. Wright et al., 2011; Mamajek, 2008), we have instead simply compared our observed spectrum with suitable late-type standards from several young clusters.

In Figure 4.3.5.2, we plot the WiFeS spectrum of the Ca II H&K spectral region for HD 54236B against stars with similar effective temperatures ( $4200K \leq T_{eff} \leq 4520K$ ) from three different

open clusters spanning the same range of ages found in our analysis of the Li abundances in the previous section 4.3.5.1.

The open cluster spectra were taken from the Keck HIRES and VLT UVES public archives and convolved down to match the lower resolution of the WiFeS observation. We performed a manual examination of the available spectra to confirm that the open cluster stars plotted are typical in their level of activity for their respective ages.

The agreement of the comparison open cluster spectra to the HD 54236B spectrum outside of the Ca II H&K lines is good evidence that the selected open cluster stars are of appropriately similar spectral type. This is important because the change in level of activity in this age range is a fairly sensitive function of spectral type. For instance, at Pleiades age the Ca II H&K emission cores transition from very strongly present for  $T_{\text{eff}} \lesssim 4300$  K to modest (at this spectral resolution) for  $T_{\text{eff}} \gtrsim 4475$  K, a change of only 175 K.

Nevertheless, all of the Pleiades show significant Ca II emission (even at the WiFeS resolution) at levels significantly higher than observed in HD 54236B. In contrast, there is also agreement between the observed mild emission in HD 54236B and the M7 comparison star (Bottom panel, 4.19). Together, these comparisons strongly imply an age for HD 54236B (and therefore of the HD 54236 system) that is older than the Pleiades ( $\sim 130$  Myr) and younger than M7 ( $\sim 300$  Myr).

#### 4.3.5.3 Isochrone fitting

Ancillary age estimates for HD 54236 B are fitted using photometry and MIST stellar evolutionary models by `MINESweeper` (for extensive details on the fitting procedure, including priors used in the inference, see Cargile et al., 2019). Using a Bayesian approach, `MINESweeper` estimates stellar parameters from MIST stellar evolutionary models (Choi et al., 2016).

`MINESweeper` employs multi-nested ellipsoid sampling (due to its efficiency in sampling multimodal likelihood surfaces like stellar isochrones; Feroz et al., 2019) and utilizes optimized interpolation following Dotter (2016). Fitting *Gaia* DR2, 2MASS, and UNWISE photometry for HD 54236B, `MINESweeper` and the latest MIST stellar evolutionary models yield an age estimate of  $149^{+173}_{-77}$ -Myr for HD54236 B, in agreement with our other age estimators outlined above. Being that HD 54236B is a single star, binarity is not an added complication to fitting and, having lower mass than its EB companion is also less evolved than the HD 54236A EB, therefore, HD 54236B's position on in HR diagram space is more sensitive to the system's age.

#### 4.3.5.4 Summary of Age Estimates

Our observation of the Ca II H&K mission in the HD 54236B K-dwarf star implies an age for HD 54236B (and therefore of the entire HD 54236 system) that is clearly older than the Pleiades



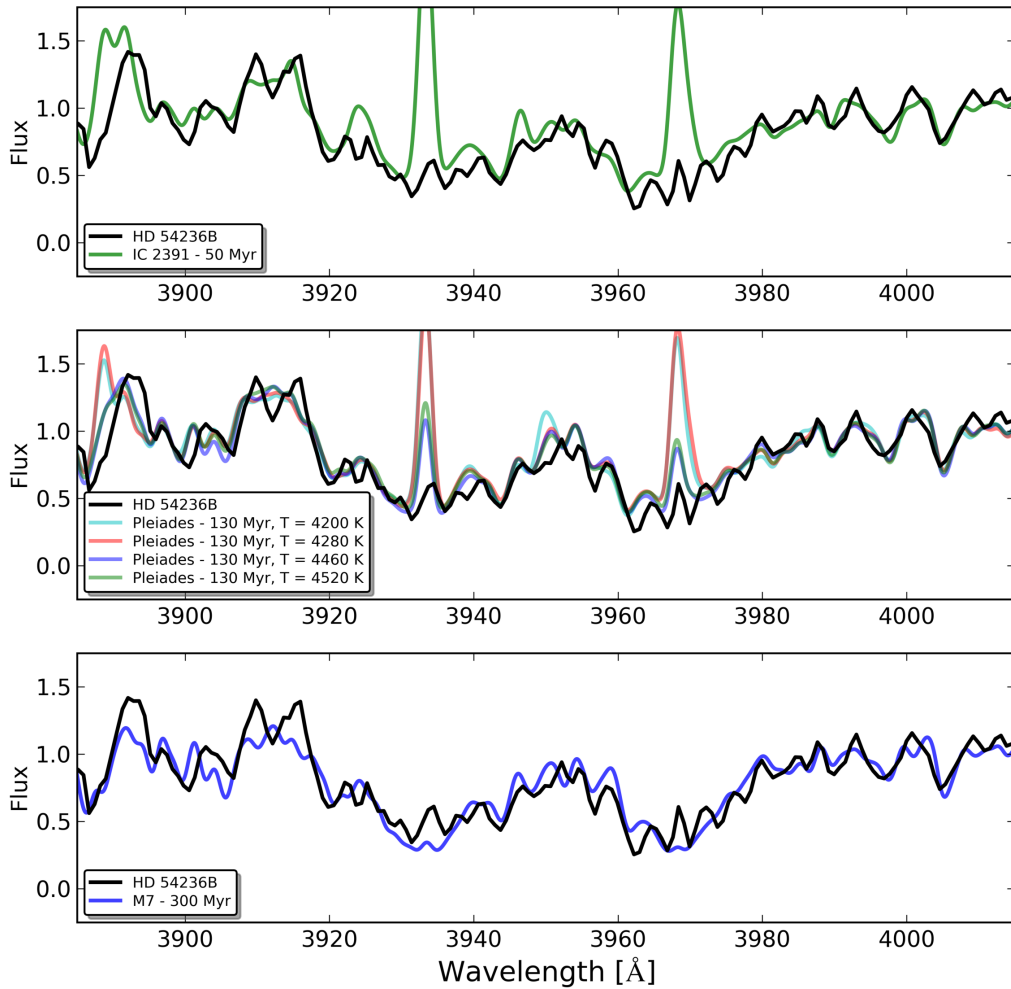


Figure 4.19: Ca II H&K analysis of the WiFeS spectrum for HD 54236B against stars with similar  $T_{\text{eff}}$  from three different open clusters spanning the range of ages estimated from the Li abundances in §4.3.5.1. Against the Ca II H&K analysis for HD 54236B (black line). *Top:* comparison with IC 2391 (age  $\sim 50$  Myr). *Middle:* comparison with Pleiades (age  $\sim 130$  Myr with a range of  $T_{\text{eff}}$  from 4200 K - 5420 K). *Bottom:* Comparison with M7 (age  $\sim 300$  Myr). The open cluster spectra were taken from Keck HIRES and VLT UVES public archives and convolved to match the resolution of the WiFeS observation of HD 54236B. Taken together, these comparisons strongly imply an age of HD 54236B older than the Pleiades ( $\sim 130$  Myr) and clearly younger than M7 ( $\sim 300$  Myr).

( $\sim 130$  Myr) and clearly younger than M7 ( $\sim 300$  Myr). This result is in excellent accord with that inferred from the Li abundances of all three stars in the HD 542436 system, for which we obtained a most likely age of 200–300 Myr. As the Li results more clearly rule out an age as young as 130 Myr and the Ca II H&K results more clearly rule out an age as old as 300 Myr, we adopt a most likely system age of  $225 \pm 50$  Myr on the basis jointly of the Li abundances of all three

stars and the Ca II H&K emission of the HD 54236B component. This adopted most likely system age of  $225 \pm 50$  Myr is also in agreement with the latest MIST models projected age estimate of  $225 \pm 50$  Myr.

## 4.4 Discussion: Membership, Stellar Strings, and AB Dor

*Gaia* DR2 parallax estimates (Bailer-Jones et al., 2018) of HD 54236A puts it at a distance of 133 pc. The galactic space velocity is calculated using the *Gaia* distance, proper motion and radial velocity estimates following Johnson & Soderblom (1987). The *UVW* velocities for the HD 54236 system are calculated using astrolibR Chakraborty & Feigelson (1995) and are listed in Table 4.4.

Table 4.4: Galactic Motions of HD 54236A

Parallax	$U$	$V$	$W$
$7.56 \pm 0.024$	$9.07 \pm 0.61 \text{ km s}^{-1}$	$9.54 \pm 0.36 \text{ km s}^{-1}$	$-4.97 \pm 0.23 \text{ CPM km s}^{-1}$

No membership to any population has been established HD 54236 to date. Indeed, the BANYAN  $\Sigma$  Multivariate Bayesian Algorithm (Gagné et al., 2018) reports 0% probability of this source being associated with any of the 27 nearby moving groups that the algorithm considers, based on its *Gaia* DR2 distance and proper motion estimates (Gaia Collaboration et al., 2018; Bailer-Jones et al., 2018).

Nonetheless as the number of known co-moving groups has grown significantly in the recent years, we search for other possible candidate populations from which HD 54236A may have originated. In particular, we perform a cross-match against Kounkel & Covey (2019); Kounkel et al. (2020) catalog, searching for the nearest moving group of which this source may be the most likely member. Examining the sources located closer than  $\pi > 6$  mas, with position within 10 degrees, and having proper motions  $8 \text{ mas yr}^{-1}$  of the source, only one group appears to be close, Theia 301, making it the most likely progenitor.

Examining the full phase space correlation between the source and the population as a whole, HD 54236A has good agreement with the 3-dimensional spatial distribution of Theia 301, as well as with  $\mu_\alpha$  (Figure 4.20). Greater discrepancy is found in  $\mu_\delta$ , where the source is offset by almost  $\sim 10 \text{ mas yr}^{-1}$  ( $6 \text{ km s}^{-1}$ ). Such an offset could be due to multiplicity of HD 54236A affecting the astrometric solution, or due to a dynamical evolution of the population over time, gaining sufficient speed over the initial conditions to no longer be recoverable in phase-space clustering. Recent kinematic analyses have led to new associations being made for co-moving groups of Ursa Major (e.g., Gagné et al., 2020) and 32 Ori (e.g., Stauffer et al., 2020). Similarly, we find

### Phase Space Correlation Between HD-54236A and Stellar Stream Theia 301

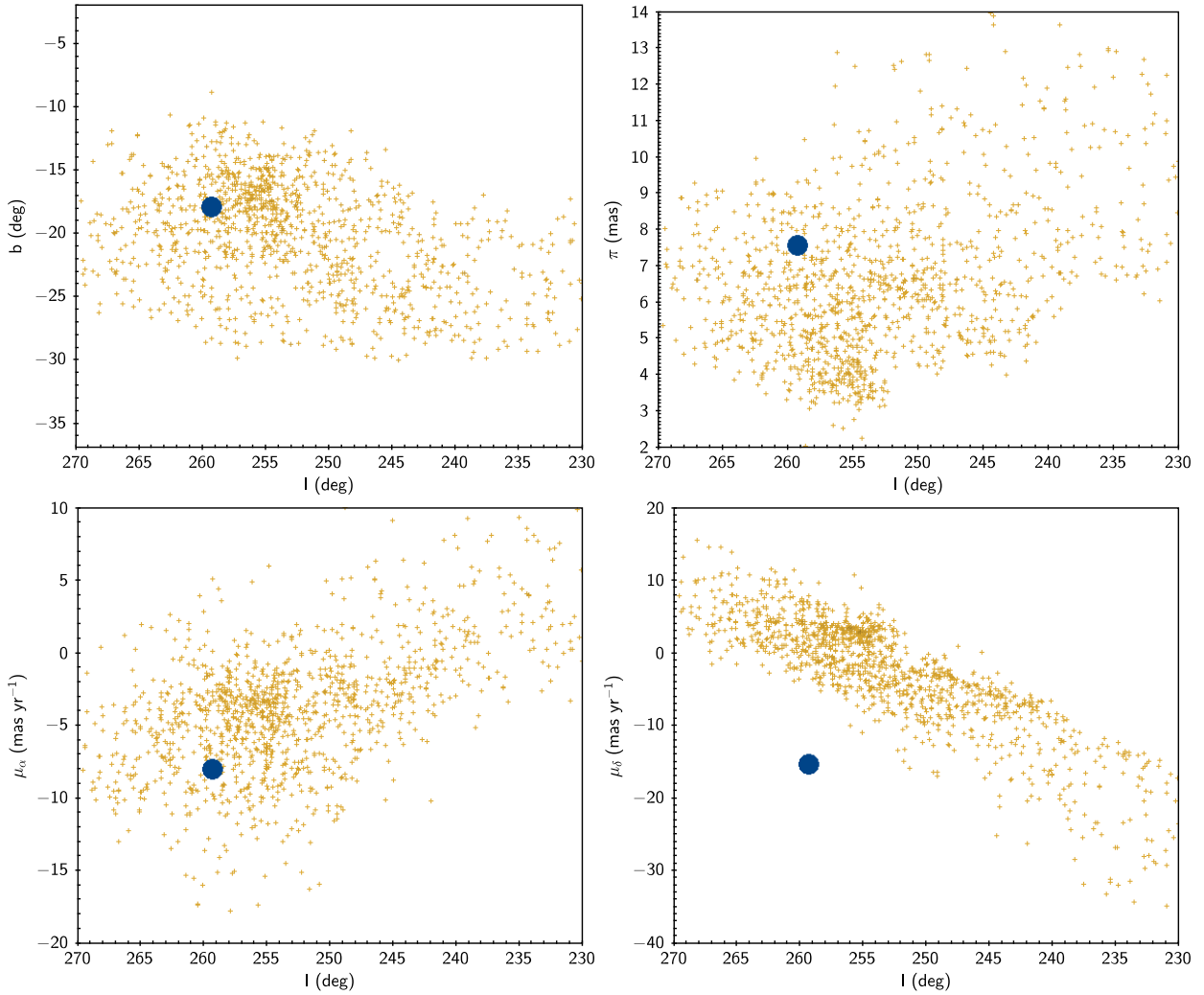


Figure 4.20: Phase space of HD 54236A relative to the phase space of Theia 301.

that a possible ancestral link exists between the AB Dor moving group and Theia 301. Six listed members of the AB Dor association also have membership to Theia 301 (Messina et al., 2010). Connection between the stellar censuses of Theia-301 and AB Dor are tenuous as so few members of AB Dor are known at distances farther than 80 pc and clustering from Kounkel & Covey (2019) struggles to identify members of moving groups within 100 pc. The observational knowledge gaps in established AB-Dor members beyond 80 pc and clustering within 100 pc converge where we would expect to find shared stellar members between these associations. Even so, there have been 6 stars from Messina et al. (2010) that are listed as members of AB Dor are also members of Theia 301, serving as a bridge between the two populations. The two populations are independently estimated to have roughly the same ages. The age of Theia 301 obtained from the population isochrone fitting is  $8.29 \pm 0.16$  dex, i.e, 134–280 Myr. The age of AB Dor mov-

ing group is estimated at 130–200 Myr (Bell et al., 2015). Both are consistent with the age of HD 54236 derived through Li I (§4.3.5.1) and Ca II (§4.3.5.2) abundances.

The age of the AB Dor association’s namesake, AB Dor, has been a subject of debate since the findings of Close et al. (2005) estimated the age of the lowest-mass component of the system, AB Dor C, to be only  $\sim 50$  Myr.

That same year, Luhman et al. (2005) reported a conservative age range of AB Dor C as 75–150 Myr. When the Close et al. (2005) more youthful age estimate of  $\sim 50$  Myr is used, the luminosity of AB Dor C appears highly discrepant with stellar evolution models predictions. However, when an older age like those suggested by Luhman et al. (2005) and Barenfeld et al. (2013) is used, much of the luminosity discrepancy disappears. Assuming that HD 54236 is indeed a member of Theia 301, and further that Theia 301 is linked to the AB Dor association, our robust age estimates of HD 54236 through lithium abundances (see §4.3.5.1) and Ca II H&K (§4.3.5.2) would in turn imply an age for AB Dor that agrees with older age estimates. Our age estimate of  $\sim 225$  Myr being applied to AB Dor C mitigates its luminosity problem.

## 4.5 Summary and Conclusions

We have shown that HD 54236 is a hierarchical triple system comprising HD 54236A as a previously unknown EB with stellar masses of  $1.18 M_{\odot}$  and  $1.07 M_{\odot}$ , and the late-K type star HD 54236B as a wide CPM tertiary, with estimated mass  $0.5\text{--}0.6 M_{\odot}$ . We have furthermore shown that the system is young, with a most likely system age of  $225 \pm 50$  Myr from joint consideration of the lithium abundances measured in the three stars and the strength of the Ca II H&K chromospheric activity index. The system age is determined independently from the lithium abundances and Ca II H&K activity to be  $225 \pm 50$  Myr. Using a number of photometric observations for tertiary member HD54236 B, `MINESweeper` and the latest MIST stellar evolutionary models, yield an age estimate of  $149_{-77}^{+173}$  Myr for HD 54236B providing additional credence to our reported age estimate. At this age, the solar-mass eclipsing component stars (HD 54236A) are very nearly zero-age main sequence stars, and the wide low-mass tertiary companion (HD 54236B) is near the end of its PMS evolution. All solutions from our analysis are collected in 4.5.

The HD 54236 system is also interesting from the standpoint of its dynamics, by virtue of representing a tight EB with orbital period of 2.4 d, with a wide tertiary companion that remains unaffected by the “fountain of youth” which may exist in EBs close enough to enhance their stellar rotation. The wide tertiary companion also represents a statistically valuable object in stellar multiplicity, and the evolution of three-body tidal effects. For example Tokovinin et al. (2006) finds that, among close binary star systems with orbital periods less than 3 d, the fraction

Table 4.5: HD 54236 System Solutions

$T_{\text{eff},1}$	$6480 \pm 103 \text{ K}$
$T_{\text{eff},2}$	$6155 \pm 155 \text{ K}$
$R_1$	$1.128 \pm 0.044 R_{\odot}$
$R_2$	$1.021 \pm 0.044 R_{\odot}$
$M_1$	$1.179 \pm 0.029 M_{\odot}$
$M_2$	$1.074 \pm 0.027 M_{\odot}$
$i$	$79.4 \pm 0.2^{\circ}$
$q$	$0.9132 \pm 0.012$
$e$	$0.009 \pm 0.008$
$v_{\gamma}$	$-10.0 \pm 0.5 \text{ km s}^{-1}$
$a \sin i$	$9.810 \pm 0.080 R_{\odot}$
<b>Parallax</b>	$7.56 \pm 0.024 \text{ mas}$
$U$	$9.07 \pm 0.61 \text{ km s}^{-1}$
$V$	$9.07 \pm 0.61 \text{ km s}^{-1}$
$W$	$-4.97 \pm 0.23 \text{ km s}^{-1}$

with wide tertiaries is 96%. This promotes three-body dynamics as the primary mechanism for hardening short-period binaries, such as the short period EB HD 54236A and its tertiary member, HD 54236B. Indeed, there may be indications of previous and ongoing dynamics in the HD 54236 system. In particular, our observation of out-of-eclipse variations on a period very similar to but slightly shorter than the EB orbital period indicates that at least one component of the eclipsing binary HD 54236A is not rotationally synchronized with the binary orbit, and therefore should still be experiencing tidal effects. Later observations of the EB HD 54236A would be expected to have an out-of-eclipse variation closer to the period as rotational-orbital synchronization is achieved.

The HD 54236 system previously had no known stellar association to which it might belong. When using the BANYAN  $\Sigma$  Multivariate Bayesian Algorithm (Gagné et al., 2018) with the *Gaia* DR2 distance estimates and proper motion information (Bailer-Jones et al., 2018), HD 54236 was found to have 99% probability of being a field star. That is, every known (as of 2018) stellar association within 150 pc has a nearly 0% probability of having HD 54236A among its members. Additionally, its *Gaia* radial velocity estimates were not similar to radial velocity estimates of the systems considered by BANYAN  $\Sigma$ . However, the Kounkel & Covey (2019); Kounkel et al. (2020) catalog presented newly discovered stellar associations, including “stellar strings”, and found a likely membership to the stellar string Theia 301, which has an estimated kinematic age that is also in very good agreement with our independent age estimate for HD 54236.

Finally, the AB Dor association (and thus AB Dor itself) appears to be linked both kinematically and through a number of shared stellar members to this newly discovered “stellar string”

Theia 301. Therefore, the age of  $\sim 225$  Myr that we have found for HD 54236 (and Theia 301) would imply that the AB Dor system also shares this age. Indeed, applying our age estimate to AB Dor itself alleviates reported tension between observation and theory that arises for the luminosity of AB Dor C, when younger age estimates ( $\sim 50$  Myr) are used.

e thank the reviewer for a constructive report and helpful feedback. J=MC<sup>2</sup> would like to thank Erika McIntire, Nicole Megetarian & S. J. Clark for their continued empowerment of a mother in STEM. K.G.S. acknowledges NSF grant AST-1009810. We thank A. Aarnio for independently checking our calculation of the *UVW* space motion of the system. We also gratefully acknowledge Jaci Cloete and Piet Fourie for their technical assistance in the operation of the KELT-South telescope at the South African Astronomical Observatory. This research has made use of the SIMBAD database, operated at CDS, Strasbourg, France.

# CHAPTER 5

## Evaluation of APOGEE-identified Spectroscopic Binaries Using TESS Photometry

Abstract<sup>1</sup>

The *SDSS-APOGEE* field includes 19,635 binary candidates with multiple high resolution spectroscopic observations. Of these, 1,023 targets, dubbed the *Gold Sample* (Price-Whelan et al., 2020), are confirmed multiple systems complete with orbital solutions. *TESS* has observed the majority of *APOGEE*'s set of binary candidates including most of those in the *Gold Sample*, resulting in 2-minute cadence data for select targets and 30-minute full frame images for the remainder. Spectroscopic Eclipsing Binaries (SEBs) fill a critical role in astrophysics as the extraction of their fundamental stellar and orbital properties is possible to a high degree of precision. In the era of big data and missions like *Kepler*, *TESS*, *APOGEE* and *Gaia* observational overlaps exist whose synergy can further constrain stellar and orbital parameters. Methodology is presented for the simultaneous analysis of high precision *TESS* light curves and high-resolution, near infrared spectra from *APOGEE* to arrive at orbital solutions, age estimates, and evolutionary histories for a subset of SEBs within the *Gold Sample/TESS* overlap. This overlap contains  $\sim 150$  targets that have photometric 2-minute cadence data while the remainder have *TESS* full frame images. This subset's photometric data undergoes periodicity analysis with Box Least Squares methodology. The subsequent modeling of the *TESS-SPOC* light curves reveals ten binaries with eclipsing events: ten of which both primary and secondary eclipses visible in their *TESS* light curves. A number of targets have photometric orbital periods from these eclipsing events that are in general agreement with *APOGEE* radial velocity derived periods. Photometric observations and *APOGEE* RV estimates are folded onto these periods to increase the precision of the *Gold Sample/TESS* targets period estimates. Period solutions directly effect resultant stellar and orbital parameter solutions, being effectively the cornerstone of Keplerian solutions. In increasing precision in a systems orbital period, we also increase confidence in stellar parameters like mass and radius. Additionally, three of the binaries within the *Gold Sample/TESS* overlap are well-suited for the Broadening Function method of radial velocity extraction (Clark Cunningham et al., 2019). Unlike the cross correlation

---

<sup>1</sup>Expected Submission April 10: The Astronomical Journal

function currently used in the *APOGEE* pipeline (Nidever et al., 2015), the broadening function is immune to broadening effects like peak pulling and pushing and effectively disentangles primary and secondary star’s radial velocity components and determine stellar properties for both stars in the binary. With these refined orbital and stellar parameters, age estimates, evolutionary histories, degree of coevality, and stellar association membership are evaluated.

## 5.1 Introduction

The Transiting Exoplanet Survey Satellite (*TESS*) mission’s main objective is the discovery of exoplanets orbiting the brightest dwarf stars in the solar neighborhood (Ricker et al., 2015). Expected to find roughly 20,000 exoplanets during its mission (Barclay et al., 2018), *TESS* is well on its way with over 24 sectors having been explored as of this writing. The *Kepler* mission discovered thousands of eclipsing binaries with high resolution imaging in the same manner. *TESS* has been assigned nearly  $2 \times 10^5$  target stars, of these an expected  $1103 \pm 33$  will be eclipsing binary systems (Sullivan et al., 2015; Teske et al., 2018). Using the same method of transit detection, *TESS* is projected to observe thousands of eclipsing binaries (EBs), (Teske et al., 2018); resulting in high precision light curves whose eclipse depths can be analyzed to report an orbital period and a system ephemeris. Eclipsing Binaries (EBs) serve as benchmarks for testing theoretical stellar evolution models, are used in studies of exoplanet properties, (Stassun et al., 2017) and in the assessment of trigonometric parallaxes (Stassun et al., 2018).

When available, dual spectroscopic-photometric analysis allows for the direct measurement of mass and radius for both the primary and secondary stellar components in a binary system. The Apache Point Observatory Galactic Evolution Experiment (*APOGEE*) provides high definition spectra for 150,000 stars, many of which are EBs with photometric observations from *TESS* or its progenitor, *Kepler*. *APOGEE* is an ongoing member of the Sloan Digital Sky Survey IV (SDSS) collaboration, DR16 is their first data release to contain high resolution ( $R \approx 22,500$ ) *H*-band spectroscopy for *both* the northern and southern hemisphere. *APOGEE* DR16 contains nearly 3 times the sources of the previous DR14 data release. *APOGEE* uses multi-epoch observing, resulting in multiple  $A_p$ Visit spectra. Clark Cunningham et al. (2019) explored this observational overlap for a subset of SEBs in the *APOGEE/Kepler* overlap. *TESS* typically observes stars 30-100 times brighter than the targets observed by *Kepler* and will survey an area 400 times larger than *Kepler* did.

Spectroscopic Eclipsing Binaries (SEBs) can be used to confirm binary or higher order systems by detecting previously unseen secondary and tertiary companions. The cultivation of accuracy in the stellar multiplicity (binary) fraction which may effect the most fundamental galactic evolution processes, like the Initial Mass Fraction (IMF) (Stanway et al., 2020), which is the amount of ma-



terial available in an molecular cloud used for stellar formation. Recently, Price-Whelan et al. (2020) cataloged 20,000 binary star systems in *APOGEE* DR16. Having multiple  $\text{ApV}_{\text{visit}}$  spectra serves in providing a high S/N for fainter targets in terms of flux over time, and also aids in the identification of binary systems. The  $\text{ApV}_{\text{visit}}$  spectra are combined and pseudo-continuum normalized to remove interstellar reddening and atmospheric absorption effects before reaching the *APOGEE* data reduction pipeline (Nidever et al., 2015; Pérez et al., 2016). The *APOGEE* Stellar Parameter and Chemical Abundance Pipeline (ASPCAP) serves to accomplish a main objective of the *APOGEE* survey, extracting the chemical abundances of several elements for the entirety of its observed sample.

The sheer size *APOGEE* field provides vast overlap between current and future photometric missions. While many studies have used photometric and spectroscopic data together, including the *APOKASC* catalog (Pinsonneault et al., 2014, 2018) which combined *Kepler* astroseismology with *APOGEE* stellar parameters, such works do not consider stellar multiplicity. There still exist binary and higher order systems in both the *Kepler/APOGEE* and *TESS/APOGEE* overlaps - untapped astrophysical caches, ripe with highly accessible binaries just beginning to be fully characterized.

In this work we identify 3 SEB IIs in the overlap between the *TESS* and *APOGEE* missions and refine orbital period estimates for all eleven EBs within our subset. In §5.2 we outline our selection criteria for our subset and detail our analysis flow and modeling methodology. Here we also illustrate the Broadening Function (BF) method of RV extraction as superior method to extract velocity components from the  $\text{ApV}_{\text{visit}}$  spectra. Then, in §5, I discuss the Gold Sample RV-photometric eclipsing event derived orbital period discrepancy, overview the most accessible and interesting targets in the subset and present their orbital solutions. Finally, §6 explores each star’s evolutionary history in the HR diagram and evaluates age estimates and coevality for our SEBs. To close, I will investigate the relationship between our orbital solutions and the presence of (previously unknown) tertiary companions.

## 5.2 Data and Methods

To identify promising SEBs within the *APOGEE**TESS* we begin with the catalog of close binaries found in *APOGEE* DR16 compiled by ? (referred to as the *Gold Sample*) and cross referenced it to *TESS* sectors after implementing an *H* band luminosity limit ( $H < 14$ ). These targets are then cross referenced using the *AstroQuery* package, and in cases where more than one positional match (RA, Dec) were found, targets were confirmed by matching *H* magnitudes. Once *TESS* targets within the *Gold sample* were identified using the *MAST* archive a *TESS* magnitude limit of  $T < 14$  was also applied.

### 5.3 Sample Selection

The *Gold Sample*, (Price-Whelan et al., 2020) is composed of a number of binary targets whom pass a number of stringent quality cuts and have converged unimodal or bimodal posterior samplings. This list is a subset of the catalog Price-Whelan et al. (2020) used to complete binary population studies. The *Gold Sample* is defined as sources within the Price-Whelan et al. (2020) catalog that pass a number of quality cuts:

- *Gold Sample* Sources must have a match to a *Gaia* source within 2'' of the source's reported 2MASS position,
- Each source has a stellar mass estimate in the STARHORSE (Queiroz et al., 2020) catalog,
- No *Gaia* targets can be within 2'' of the source with *G* band magnitude differences  $\Delta G > -5$ , this removes stellar neighbors that would lie within the same *APOGEE* fiber as the source, and could therefore contaminate its spectrum,
- There must be no additional *Gaia* sources within 10 arcsec that have a *G* band magnitude difference  $\Delta G > 2.5$ , this excludes sources with bright neighboring stars,
- To reflect reasonable stellar parameters,  $-0.5 < \log g < 5.5$ ,
- An effective temperature range of  $3500 < T_{\text{eff}} < 8000$  K,
- $-2.5 < [M/H] < 0.5$  metallicity range,
- $s_{\text{MAP}} < 0.5 \frac{\text{km}}{\text{s}}$  which excludes sources with large inferred excess variances,
- Each source must have more than 5 visit spectra,  $n_{\text{ApVisit}} > 5$ .

The total census of *Gold Sample* members includes 1032 systems with unimodal samplings, and 492 that have bimodal samplings (Price-Whelan et al., 2020). The samples examined here, and those in Price-Whelan et al. (2020) are *close* binaries, which have binary periods from days to years, and semi major axes less than a few AU. These types of systems represent 20 - 40% of the closest bound binary star systems. It is important to note that as of this time, the binary star population extends from the close systems described here to those with  $a > 20000 \text{AU}$  and binary periods  $\sim \log 250$  yr.

A number of studies have utilized *APOGEE* targets with high numbers of  $n_{\text{ApVisit}}$  spectra: Troup et al. (2016) who used *APOGEE-1* data to catalog binary targets. Price-Whelan et al. (2017) used *APOGEE-DR13* (Holtzman et al., 2015) to demonstrate the reliability of The

Joker, a Monte Carlo Sampler for binary star and exoplanet radial velocity data. The obstacle facing implementing spectroscopic dependent methodology to the current *APOGEE-DR16* is that the majority of *APOGEE* sources in DR16 do not have the time resolution or the number of *ApVisit* spectra required for fully determining orbital properties (Price-Whelan et al., 2020).

## 5.4 TESS Photometry

Binaries that have been spectroscopically studied by *SDSS-APOGEE* and photometrically observed by *TESS* or its predecessors like *Kepler* offer valuable constraints in solving for orbital and stellar parameters. This is especially true in binaries that have eclipsing events, and even more pronounced in those with both a primary and secondary eclipsing event in their light curves. These Spectroscopic Eclipsing Binary systems (SEBs) can be so well scrutinized that they can serve as benchmarks for testing stellar evolution theory and fundamental stellar relationships. In Clark Cunningham et al. (2019), the simultaneous modeling of *APOGEE* RVs (extracted from *ApVisit* spectra using the broadening function (Rucinski, 2002)) and *Kepler* photometry yields orbital solutions and mass solutions for both primary and secondary binary components of the system for a subset of SEBs.

The Transiting Exoplanet Survey Satellite (*TESS*) provides detailed photometric data for nearly every target listed in the *APOGEE Gold Sample*. The *TESS* Science Processing Center *SPOC* (Jenkins et al., 2016) generates calibrated pixels and light curves similar to the Kepler Science Processing Pipeline (Jenkins et al., 2010). Targets within the the *Gold Sample/TESS* overlap with *SPOC* generated light curves are selected for this analysis. This methodology can be revisited as more *TESS-SPOC* light curves become available, or with the analysis of raw *TESS* photometric data. The *APOGEE Gold Sample/TESS* overlap contains  $\sim 130$  targets with *SPOC* 2m or 30m light curves, these are hereafter referred to as *Gold Sample/TESS-SPOC* targets.

The *SPOC* processed photometric data is retrieved through the MAST archive.<sup>2</sup> Some targets within our *Gold Sample/TESS-SPOC* overlap had processed light curves from the MIT Quick Look Pipeline (Huang et al., 2020a,b; Kunimoto et al., 2021) which are similarly acquired through the MAST archive.

*TESS* photometric orbital periods are effectively restricted to an upper limit of  $\sim 27$  days. This is due to *TESS* observing in sectors spanning  $24^\circ \times 96^\circ$  each being observed for two *TESS* orbits, or roughly 27 days. This limit is congruent with the bounds of close binary systems best suited for the analysis outlined in this work.

The *Gold Sample/TESS-SPOC* Pre Search Data Conditioning Simple Aperture Photometry (PD-CSAP) and Simple Aperture Photometry (SAP) are normalized before undergoing periodicity

---

<sup>2</sup><https://dx.doi.org/10.17909/T9RP4V>

analysis using the Box Least Squares (BLS) methodology from `Astropy` (Sipocz et al., 2016), those with eclipsing events having the advantage of period confirmation by eye in the modeling of their light curve. Once an orbital period is derived from each targets’ photometric data, they are compared to their respective spectroscopically derived RV orbital period solution, reported in the Gold Sample (Price-Whelan et al., 2020).

Next, light curves for each *Gold Sample/TESS-SPOC* binary are folded onto our photometric orbital period, and separately folded onto their *APOGEE* Radial Velocity (RV) derived orbital period. These phase folded light curves are compared to indicate which orbital period (*APOGEE-RV* or *TESS-SPOC*) is closer to the system’s true orbital period based on the clarity of eclipsing events. These results are listed in §5.6.

## 5.5 *APOGEE* Spectroscopy

*SDSS-APOGEE* has the primary mission of surveying over 100,000 red giant stars across the galactic bulge, disk and halo. *APOGEE* attains radial velocity estimates and chemical abundances from spectroscopic observations, to provide insight to the formation and evolution of our galaxy. This high definition ( $R \sim 20,000$ ) H band spectroscopy targets predominantly red-giant stars, although *DR16* contains many main sequence targets. While *APOGEE* is not designed explicitly for binary star characterization, the combination of its reach in our galaxy, its coverage on the color-magnitude diagram, and multi-epoch observations embody accessible and comprehensive surveys that can be effectively used to this end. A common need exists to constrain the multiplicity (or binary) fraction, across a wide range of temperature and mass ratios, stellar type, chemistry, and dynamical environment. Multi-epoch spectroscopic data from *APOGEE* surveys can be used as a step toward large scale population inference (Price-Whelan et al., 2020).

The *APOGEE* survey most commonly observes targets multiple times over separate ‘visits’, called `ApVisit` spectra, which provide time-domain velocity information. The `ApVisit` spectra for each target are combined before the *APOGEE* data reduction pipeline (Nidever et al., 2015) determines the target’s stellar parameters and chemical abundances. The number of `ApVisit` spectra available for a target (cadences and time-baselines) are determined through signal-to-noise thresholds for the faintest objects in the observed field (Majewski et al., 2017). The ideal case for effective identification and characterization of binary stars is a large number of velocity samples over a long time baseline. To meet the goal of observing  $\sim 10^5$  stars across the Milky Way, the baseline *APOGEE* visit would include roughly an hour of integration (plus overhead) divided into no less than three visits (Majewski et al., 2017). Five *APOGEE* fields were reserved for multiplicity studies, being designed specifically for companion studies, have `ApVisit`  $> 10$  spaced to potentially allow for binary system characterization (Price-Whelan

et al., 2020).

The *APOGEE-RV* estimates are folded onto our photometric orbital period (described in §5.4), and separately folded onto their *APOGEE* Radial Velocity (RV) derived orbital period. The subsequent phase versus radial velocity plots are compared to determine which orbital period (*APOGEE-RV* or *TESS-SPOC*) is closer to the system’s true orbital period. Both the phase folded *TESS* light curves and the phase folded *APOGEE* RV curves are plotted for each target in our subset with eclipsing events (see §5.2) to evaluate phase agreement between them.

*ASPCAP* then matches the *ApStar* spectrum to a synthetic single star spectrum (Zamora et al., 2015). *ASPCAP* then resolves quantities like orbital period, effective temperature ( $T_{eff}$ ), and  $\log g$ . By comparing a binary star (*ApStar*) spectrum to single star’s synthetic spectrum, the *ASPCAP* pipeline causes a systematic underestimation in effective temperature of roughly 300K (El-Badry et al., 2017). The secondary star’s spectral lines being present in the *ApStar* spectrum analyzed by *ASPCAP* causes it to fit by a synthetic spectrum with an effective temperature that does not match the binary target. Multiplicity in *APOGEE* targets introduces systematic biases in the inferred stellar parameters, this is most pronounced at the mass ratio:  $q \sim 0.7$  (El-Badry et al., 2017).

Troup et al. (2016) outlined the dependencies of *APOGEE* RV precision on (the primary component’s) stellar parameters  $T_{eff}$ ,  $\log g$ , [Fe/H] and signal to noise ratio (S/N) for each *ApVisit* spectra. Figure 2 in Troup et al. (2016) illustrates the two stronger effects on *APOGEE* RV precision: [Fe/H] and S/N for each *ApVisit* spectra. The right panel of this figure shows the less pronounced effects of the stellar parameters of  $T_{eff}$  and  $\log g$ . Spectroscopically, these effects are caused the presence, and number of absorption lines in the *ApVisit* spectra.

Of the ten *Gold Sample/TESS-SPOC* binary targets that have both primary and secondary eclipsing events in their light curves, six binary systems showed the presence of the secondary stellar component in their spectra. As *ASPCAP* only has single star spectroscopic models to compare against, when the secondary contributes a significant amount of light to the spectrum (as is the case with eclipsing binaries) its presence will affect how the system is fitted. While there is no specific *APOGEE* data flag for this situation, many of these situations are indicated by the `SUSPECT RV CONTAMINATION` flag in the `STARFLAG` bitmask. These flags are incorporated into sample selection for our *Gold Sample/TESS-SPOC* as a flag for SEB2 behavior, and of coarse warning for *APOGEE* RV contamination. This flag also serves to identify binary targets for which the Broadening Function (BF) methodology is best suited as it also indicates a spectroscopic presence indicative of a spectroscopic binary. Additionally, the presence of the secondary star’s spectrum causes *ASPCAP* to fit the system with a cooler template, resulting in an underestimate of the system’s effective temperature (El-Badry et al., 2017).

### 5.5.1 Radial Velocities from *APOGEE* Spectroscopy

In the *APOGEE* pipeline (Nidever et al., 2015) RVs are measured using the Cross Correlation Function (CCF); which involves a template spectrum and the binary target spectra being cross correlated, which then yields the RV of the target relative to the template. The target spectra is collected over a series of visits on different days, usually spanning the standard *APOGEE* exposure time of three hours combined into a spectrum per target, called an `ApStar` spectrum. These RVs are modeled in §5. In this analysis, following Clark Cunningham et al. (2019) we instead use `ApVisit` individual visit spectra retrieved from the SDSS Science Archive Server Search Tool. Each `ApVisit` spectrum is normalized to the continuum and has erroneous telluric features removed. Removing these spectrum tellurics begins with identifying outliers above or below the continuum, by 0.7 or 3 times the standard deviation. The lower continuum factor is larger to avoid unintentionally removing real absorption line features. Around each outlier spike, a  $\pm 6$  Å window is also flagged for removal. The python scripts used to retrieve, continuum normalize, and de-spike `apVisit` spectra are heavily based on Rawls et al. (2016) on GitHub<sup>3</sup> and `apogee` python package on GitHub described in Bovy (2016).

Once `ApVisit` spectra have been continuum normalized, and telluric features removed, the Broadening Function is used to determine the spectroscopic presence of a secondary star, and in applicable cases solve for the secondary RV component. In extracting BFs from targets, a modified version of the BF software suite from Rawls et al. (2016); Clark Cunningham et al. (2019) which is based on the method first introduced by Rucinski (1992). A PHOENIX BT-Settl model atmosphere spectrum (Husser et al., 2013) is selected to match the target’s approximate spectral parameters as reported by *APOGEE*. As the majority of binary systems are not composed of identical stars, a model atmosphere spectrum is never an exact match; especially contouring the finite sampling of stellar parameters in the model grid. Indeed, Lu et al. (2001) found a mismatch in spectral type between the template and the target may cause the BF to change in its intensity scale and quality - but amplitudes of the RV components remains unchanged.

The BF peaks were examined by eye to determine their approximate locations in RV space. Three targets within the *Gold Sample/TESS-SPOC* have discernible primary and secondary BF peaks which are fitted with Gaussians using a least-square fitting procedure. Each Gaussian’s mean represents the RV component of its respective stellar component, which are then corrected with barycentric velocities provided in each targets `ApStar` spectrum. Uncertainties in the RV arise from errors in the Gaussian fit of the RV peaks. In the same way as the CCF extraction done in the *APOGEE* pipeline (Nidever et al., 2015), the uncertainty in the measurement of the BF peak is semi-dependent on the semi-arbitrary width of peak determines the RV uncertainty. In

---

<sup>3</sup><https://github.com/mrawls/apVisitproc>

this way, the uncertainty of a RV measurement is systematically underestimated. Following Clark Cunningham et al. (2019), peaks for *APOGEE* double lined SEBs are extracted using the BF, instead of CCF methodology where applicable. This clearer separation and definition allows for a more robust measurement of the RVs for each each component. The superior resolution of the BF method is attributed to the BF function being effectively immune to 'peak pulling' and 'peak pushing' by virtue of being a true linear de-convolution (Rucinski, 2003). The measured RVs and BF for the three BF suitable systems in the *Gold Sample/TESS-SPOC* overlap are found in §5.6. Additionally, Bayless & Orosz (2006) and Stassun et al. (2007) found that the ratio of the BF peak areas is directly proportional to the flux ratio of the binary in the *APOGEE H* band. These flux ratios and other variables for RV extraction are discussed in §5.2.

## 5.6 Results

This section contains the results of the analysis outlined above for the ten EBs present in our defined subset. Within this subset, three targets are confirmed as SEB II systems, and two of those are conducive to thorough modeling and extraction of stellar and orbital parameters including estimates of the secondary stellar component of mass and radii. These two systems most conducive to the analysis methodology described in this work had their primary and secondary RV components extracted using the BF. A similar methodology was followed in Clark Cunningham et al. (2019) in which a subset of SEB IIs were studied within the *APOGEE/Kepler* observational overlap. An enlightening comparison between the clarity of the BF peaks compared to the CCF peaks is included there for two of the *APOGEE/Kepler* SEB IIs, shown in Figures 3.1 and 3.2. In these specific systems, the BF is less effected by the peak pulling and pushing effects than the CCF, and therefore less prone to the cancellation of RV information from the secondary stellar component. Figure ?? shows the specific case in which the BF was able to identify a tertiary component that the CCF did not identify. That flavor of thorough extraction was possible in two of our ten EB systems within the *AuAPOGEE/TESS* overlap (the SEB II systems: TIC 053478754 and TIC 171517465, both of which have readily disentangled contributions in their spectroscopic analysis. TIC 099763308, while being a likely SEB II with a high number of  $A_{pVisit}$  spectra (25) and a high signal to noise ratio, remains difficult to disentangle in terms of its stellar components. TIC 099763308 persists as a viable target, especially in the realm of simultaneous photometric and spectroscopic analysis, but that is not completed in this work.

## 5.6.1 TIC 053478754

TIC 05347854 (2M10474905+48151660) has a photometrically estimated orbital period of 12.8886 d and is a confirmed SEB II, containing both a primary and secondary eclipsing event in its *TESS* LC, and prominent primary and secondary peaks visible in each of its six *ApVisit* spectra. It was observed by *TESS* with long (30 min) cadence in Sector 21. The *AuPOGEE* sample stated a spectroscopic radial velocity determined orbital period of 12.9005 d. The percent difference between this period and the orbital period derived via the *TESS-SPOC* photometric eclipsing events and BLS analysis is  $\sim 0.0930625\%$ . The unfolded LC and RVs are shown in the top row of Figure:5.1, photometric data being modeled on the left, and spectroscopic on the right. The middle row illustrates the LC and the RV curves folded onto the *APOGEE* determined orbital period, while the bottom illustrates the LC and RV curves folded onto the orbital period determined with the *TESS* photometric eclipsing events. While the difference between the RV and LC period estimates is effectively less than one percent, the difference has a dramatic effect on the clarity of the primary and secondary eclipsing events (Shown in Figure 5.2). The SIMBAD astronomical database identifies it as a high proper-motion star.

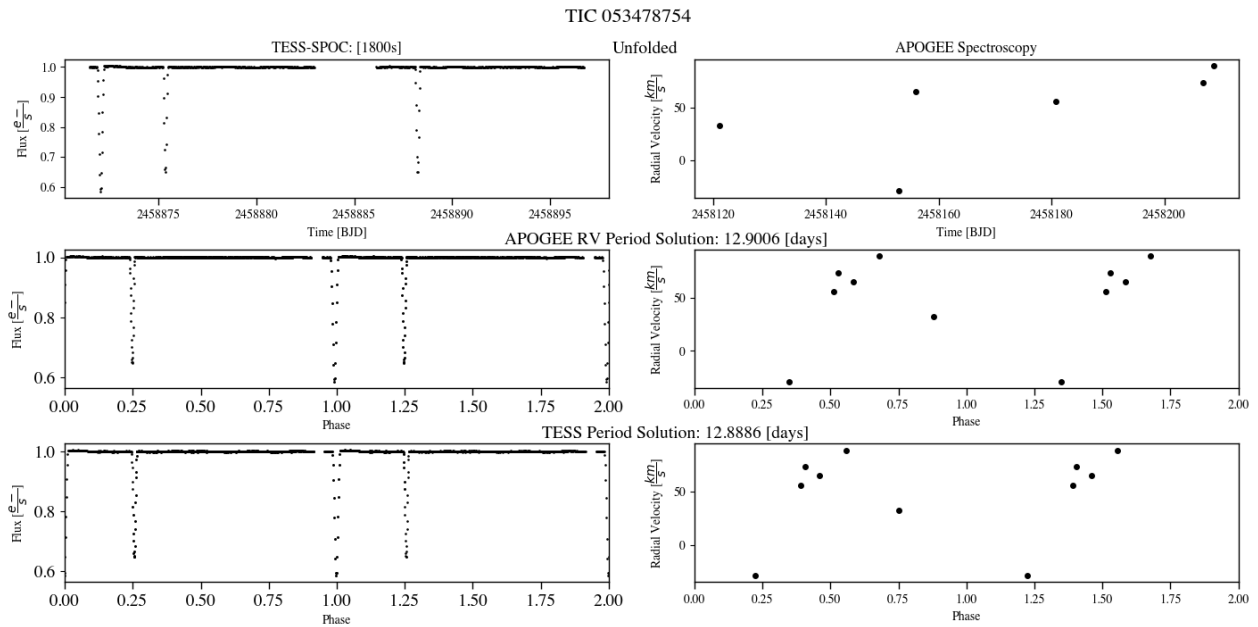


Figure 5.1: TIC 053478754 Spectroscopic and Photometric analysis: **Top-Left:** Unfolded *TESS-SPOC* LC. **Top-Right:** Unfolded *APOGEE* RV curve. **Middle-Left:** *TESS-SPOC* LC folded onto the *APOGEE Gold Sample* period solution. **Middle-Right:** *APOGEE* RV curve folded onto the *APOGEE Gold Sample* period solution. **Bottom-Left:** *TESS-SPOC* LC folded onto our *TESS* BLS periodicity estimate. **Bottom-Right:** *APOGEE* RV curve folded onto our *TESS* BLS periodicity estimate.

In refining the period estimate within our study, the period the LC was folded on was iterated



based on clarity of the LC eclipsing event(s). Step size of the iteration began in sizes of 0.1, and once best yield of clarity established, iteration moved onto the hundredth, then thousandths and ultimately hundred thousandth in scale. Every iteration size was monitored by eye to ensure visual clarity, with finest refinements and iteration checks occurring in the smallest of step sizes. Both primary and secondary eclipsing events were considered for clarity and decorum simultaneously, whilst impediments like a low signal to noise ratio, the number of `ApVisits` and mass ratios far from unity were also accessed. The results of the BF RV extraction and the CCF RV estimates from the *APOGEE* are provided in the following table:

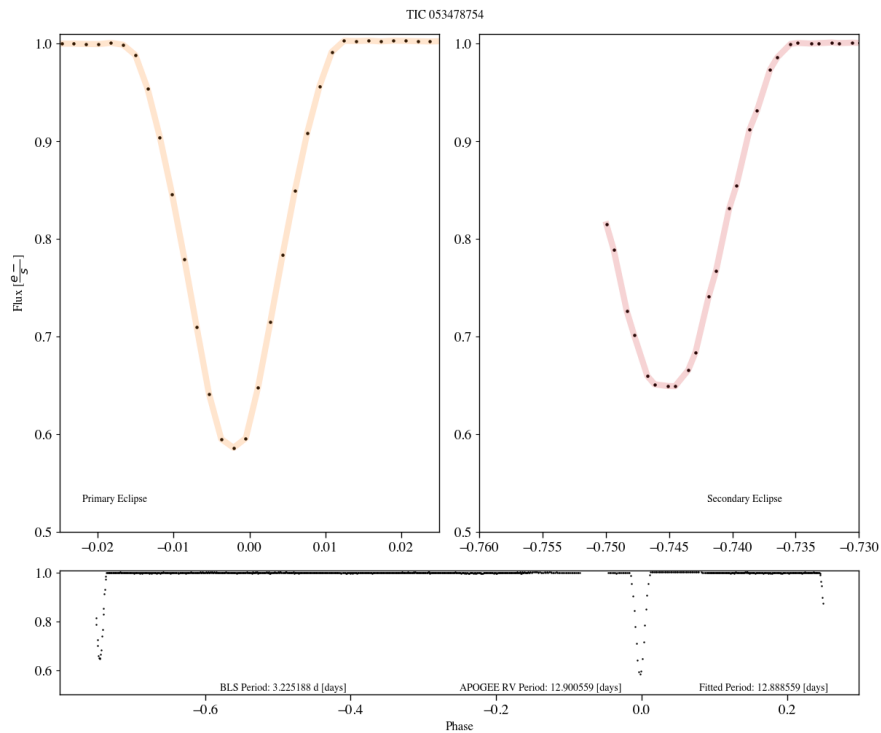


Figure 5.2: TIC 053478754 Primary and Secondary eclipsing events. These eclipsing events are derived through folding the *TESS-SPOC* photometry onto the results of its BLS periodicity analysis. From the depths of the eclipses, we know that the system has a mass ratio around  $q \sim 0.85$ . Unfortunately in this target, the entirety of the secondary eclipsing event was not captured by the *TESS* observations, however, assuming a symmetric eclipse, we are still able to solve for stellar parameters from these eclipses.

## 5.6.2 TIC 171517465

TIC 171517465 has no distinctive object flags in the *SIMBAD* database, *TESS* observed this object with 30 min cadence in sector 20. As was done in the previous section for TIC 053478754, the LC and *APOGEE* reported relative radial velocity curves are shown unfolded, folded to the *APOGEE* RV derived period from the *Gold Sample* (Price-Whelan et al., 2020) and the *TESS*

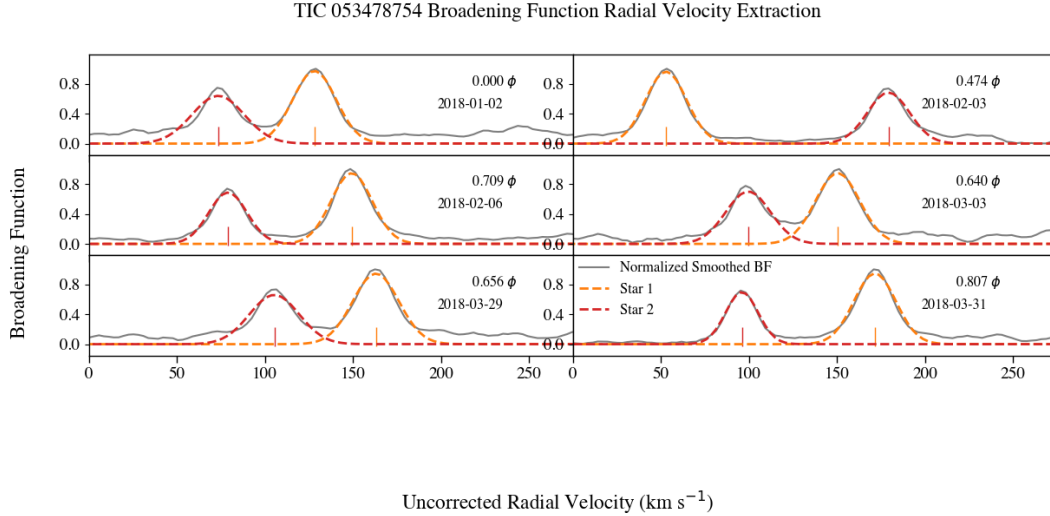


Figure 5.3: Broadening function extraction of radial velocities for TIC 053478754. The primary stellar component is modeled in yellow, and the secondary in red. The extraction of the Radial Velocities occurs at the peak amplitude’s radial velocity component. Orbital phase and the dates of the observations are provided on each subplot.

BLS periodicity period estimates, and compared for clarity and decorum (i.e., expected LC curve or RC behavior). These are shown in the Figure 5.4 for this target, the percent difference between the spectroscopic and photometrically derived orbital periods being 0.0359%.

As was done with the previous target, both primary and secondary eclipsing events were considered for clarity and decorum simultaneously, whilst impediments like a low signal to noise ratio, limited number of  $\text{ApV}_{\text{visits}}$  and mass ratios far from unity were considered.

### 5.6.3 TIC 099763308

TIC 099763308 is identified as a SEB II though the spectroscopic contributions found from both the primary and secondary stellar component in the binary. TIC 099763308 has 25  $\text{ApV}_{\text{visit}}$  spectra with a large S/N ratio ( $\sim 1335$ ). However, in this particular target the disentanglement of the secondary spectroscopic contribution is difficult. The primary BF peak here is especially prominent while the secondary BF peak becomes especially inconspicuous. Only one  $\text{ApV}_{\text{visit}}$  spectrum resulted in a fit for the system’s secondary BF peak while all  $\text{ApV}_{\text{visit}}$  primary BF peaks were successfully fitted.

The TIC 099763308 system has the longest orbital period of all of the systems within our subset. For this system, the *APOGEE* RV period estimate is 32.0309 d, and the *TESS* BLS estimate is 32.035 d with a percent difference between them of 0.0128%. The period estimates are greater than the effective period limit established by the *TESS* mission’s observing period of 27 d.

Beyond having the longest orbital period amongst our subset, TIC 099763308 is also interesting

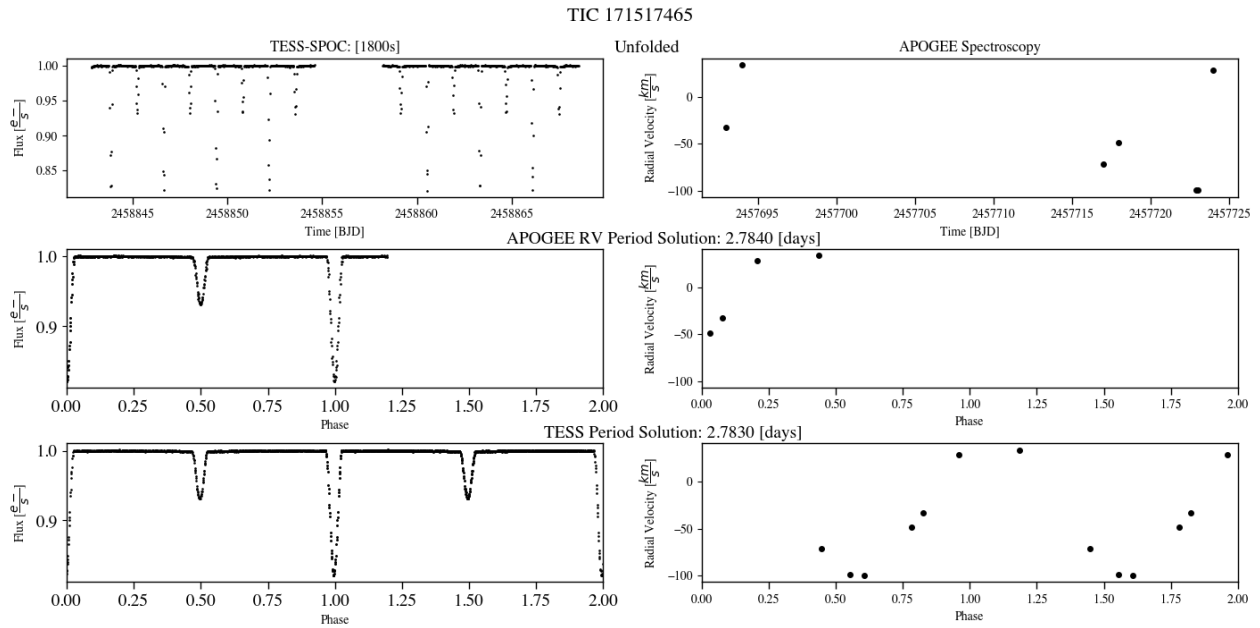


Figure 5.4: TIC 171517465 Spectroscopic and Photometric analysis: **Top-Left:** Unfolded *TESS-SPOC* LC. **Top-Right:** Unfolded *APOGEE* RV curve. **Middle-Left:** *TESS-SPOC* LC folded onto the *APOGEE Gold Sample* period solution. **Middle-Right:** *APOGEE* RV curve folded onto the *APOGEE Gold Sample* period solution. **Bottom-Left:** *TESS-SPOC* LC folded onto our *TESS* BLS periodicity estimate. **Bottom-Right:** *APOGEE* RV curve folded onto our *TESS* BLS periodicity estimate.

by virtue of the shape of its eclipsing events. In Fig. 5.7 close ups of the eclipsing events found the the *TESS* photometry folded onto the BLS result after being iterated for clarity. Both primary and secondary eclipsing events are fairly wide, and especially in the secondary eclipsing event, a flat bottom shape to the eclipse is visible. This indicates a near totally eclipsing system.

#### 5.6.4 TIC 416593638

TIC 416593638 has a total of eleven  $\text{ApVisit}$  spectra, and was observed with *TESS* 30 min exposure in sectors 15, 16, and 22. The *APOGEE Gold Sample* RV period result for this target was 3.6665 d, while our BLS periodicity analysis on the *TESS* LCs yielded an orbital period estimate of 3.6676 d. The percent difference in this case is 0.03%. In the case of TIC 416593638 to focus of the primary and secondary eclipse definition during the iterative period fitting modeling was especially crucial.

In this cases, persistent noise in the  $\text{ApVisit}$  spectrum (even after completing the deapsiking and normalization) caused only one observation that could be fitted to the primary BF peak with confidence. Secondary RV features may be present in one or more of these visits, but they are not readily discernible amongst the persistent noise. Both photometric and spectroscopic observa-

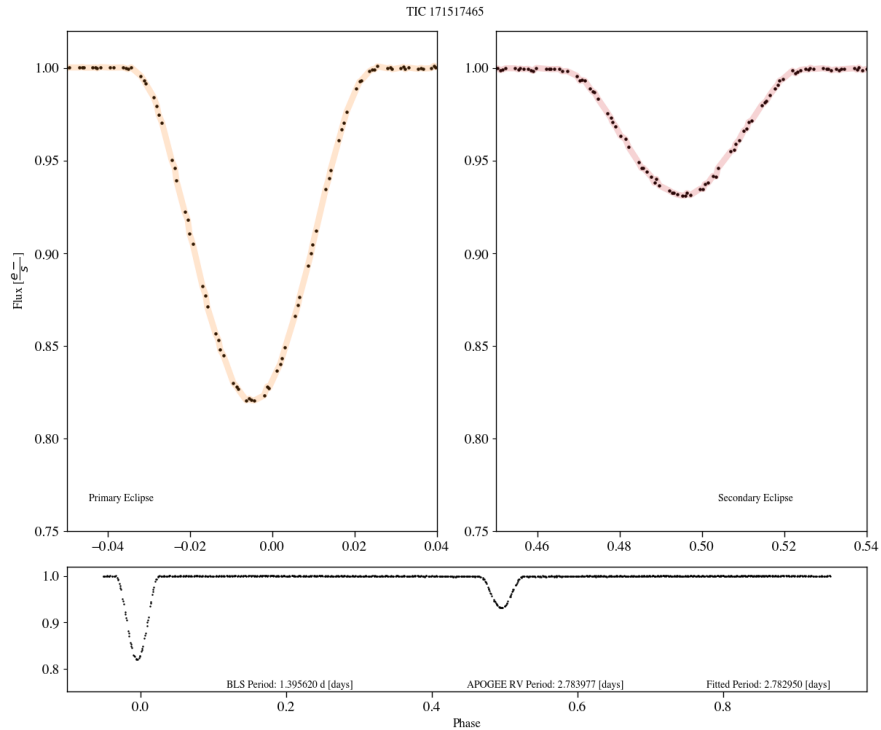


Figure 5.5: TIC 171517465 Primary and Secondary eclipsing events. These eclipsing events are derived through folding the *TESS-SPOC* photometry onto the results of its BLS periodicity analysis. From the depths of the eclipses, we know that the system has a mass ratio around  $q \sim 0.85$ . Unfortunately in this target, the entirety of the secondary eclipsing event was not captured by the *TESS* observations, however, assuming a symmetric eclipse, we are still able to solve for stellar parameters from these eclipses.

tions for this particular system have low signal to noise ratios.

In addition to the low signal to noise ratio in this system, and pronounced difference in eclipse depths, areas, and therefore contributed flux, the components are extremely difficult to disentangle with confidence.

### 5.6.5 TIC 284597233

*TESS* observed TIC 284597233 with long cadence in sectors 15, 21, and 22. And has been observed by *APOGEE* on six occasions. An *APOGEE*[STARFLAG] indicates a possible contaminant from a bright stellar neighbor. The *APOGEE* RV period solution from the *Gold Sample* for this system was 3.9405 d, while the *TESS* BLS periodicity analysis estimate was 3.9296 d resulting in a 0.27% difference between them. Interestingly, this is the only target in our subset who had an *APOGEE* orbital period that was seemingly a slight overestimate if our periodicity results are correct. The other targets within our subset had orbital period estimates that were underestimates compared to our results. Also, TIC 284597233 also has one of the highest differences

TIC 171517465 Broadening Function Radial Velocity Extraction

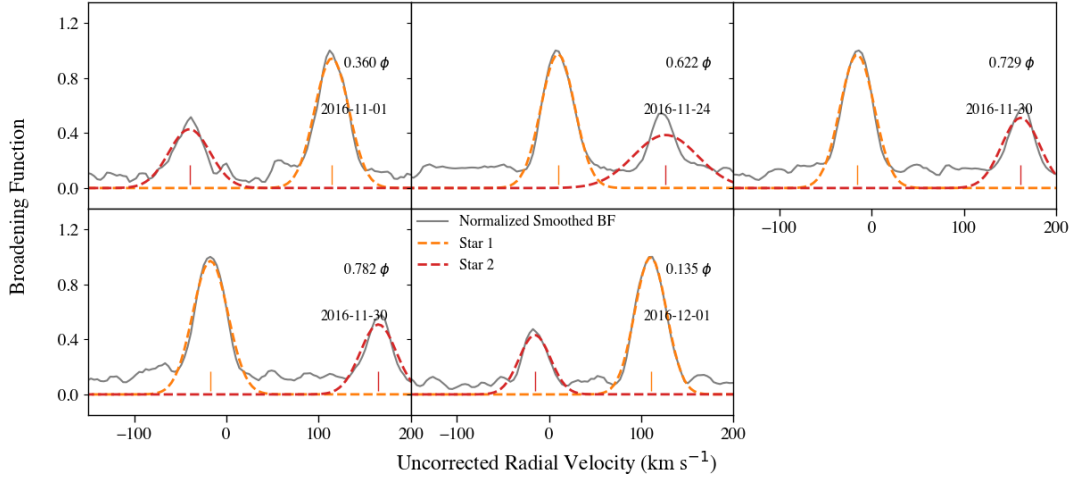


Figure 5.6: Broadening function extraction of radial velocities for TIC 171517465. The primary stellar component is modeled in yellow, and the secondary in red. The extraction of the Radial Velocities occurs at the peak amplitude’s radial velocity component. Orbital phase and the dates of the observations are provided on each subplot.

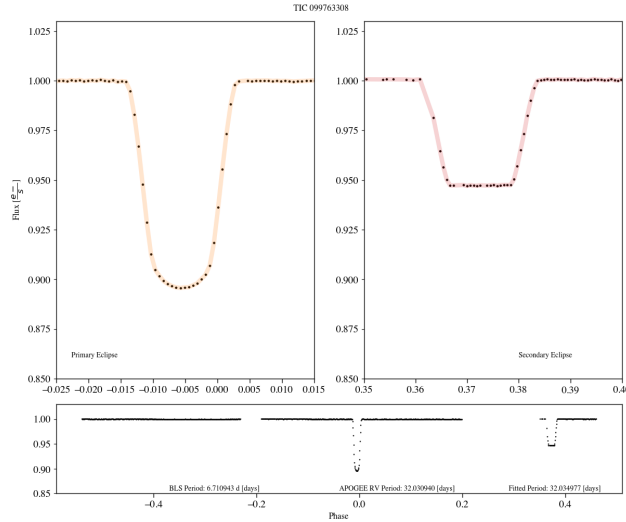


Figure 5.7: TIC 099763308 Primary and Secondary eclipsing events. These eclipsing events are derived through folding the *TESS-SPOC* photometry onto the results of its BLS periodicity analysis. From the depths of the eclipses, we know that the system has a mass ratio around  $q \sim 0.85$ . Unfortunately in this target, the entirety of the secondary eclipsing event was not captured by the *TESS* observations, however, assuming a symmetric eclipse, we are still able to solve for stellar parameters from these eclipses.

between the two estimates.

Unfortunately, the TIC 284597233 system does not appear to be conducive to the Broadening Function (BF) of RV extraction. After following our normalization and despiking routines, the

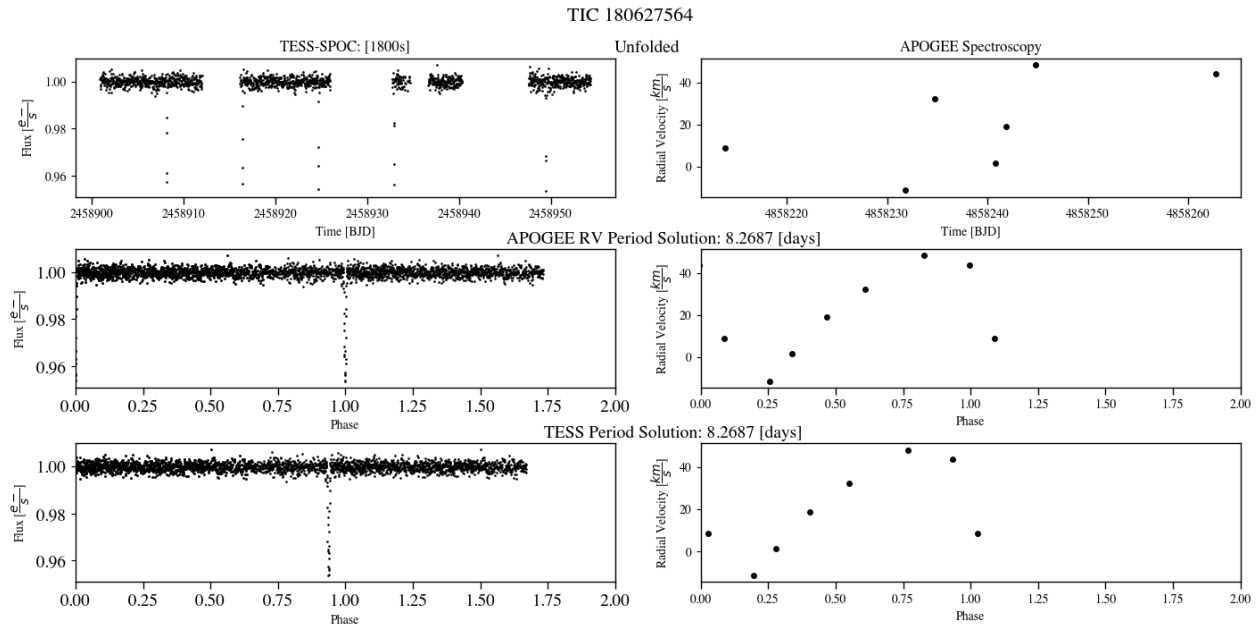


Figure 5.8: TIC 180627564 Spectroscopic and Photometric analysis: **Top-Left:** Unfolded *TESS-SPOC* LC. **Top-Right:** Unfolded *APOGEE* RV curve. **Middle-Left:** *TESS-SPOC* LC folded onto the *APOGEE Gold Sample* period solution. **Middle-Right:** *APOGEE* RV curve folded onto the *APOGEE Gold Sample* period solution. **Bottom-Left:** *TESS-SPOC* LC folded onto our *TESS* BLS periodicity estimate. **Bottom-Right:** *APOGEE* RV curve folded onto our *TESS* BLS periodicity estimate.

secondary component of the RV was remained difficult to disentangle with certainty. This could be partially due to the pronounced difference in the depth and area of the primary and secondary eclipsing events, and potentially due to contaminant light from a neighboring star. The *TESS* photometry for this system also had enduring noise after normalization and smoothing were completed. This lends credence to the possibility that the neighboring bright neighbour contaminant could be the cause.

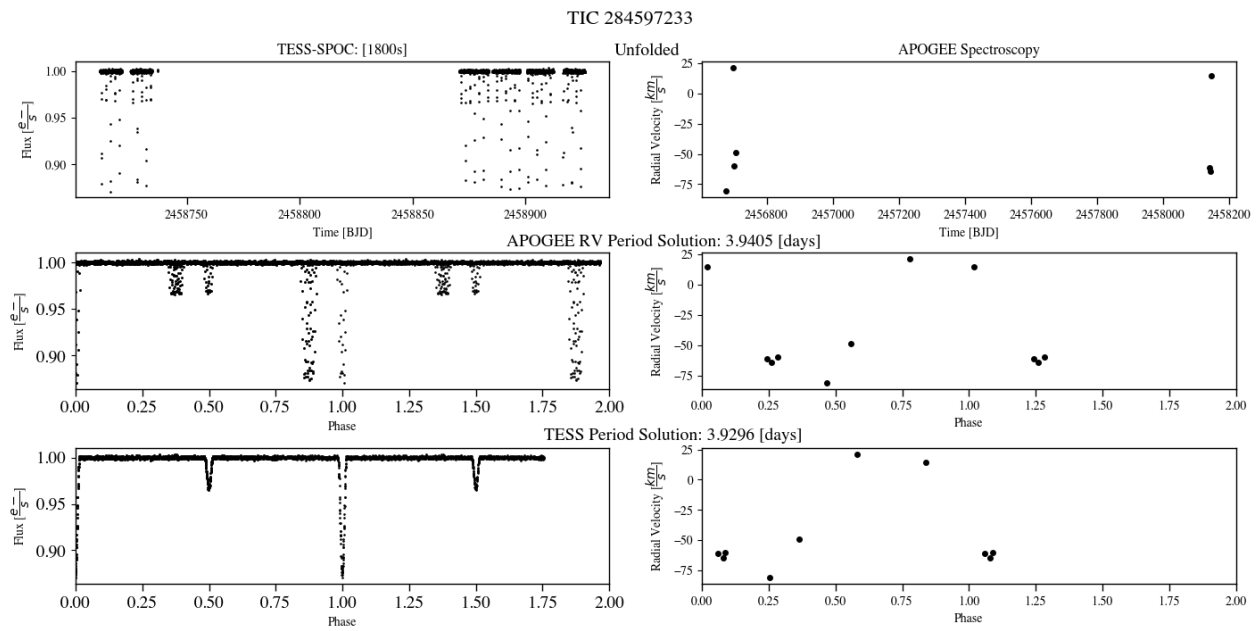


Figure 5.9: TIC 284597233 Spectroscopic and Photometric analysis: **Top-Left:** Unfolded *TESS-SPOC* LC. **Top-Right:** Unfolded *APOGEE* RV curve. **Middle-Left:** *TESS-SPOC* LC folded onto the *APOGEE Gold Sample* period solution. **Middle-Right:** *APOGEE* RV curve folded onto the *APOGEE Gold Sample* period solution. **Bottom-Left:** *TESS-SPOC* LC folded onto our *TESS* BLS periodicity estimate. **Bottom-Right:** *APOGEE* RV curve folded onto our *TESS* BLS periodicity estimate.

# CHAPTER 6

## Discussion

The overarching theme in this work and the projects contained within it is the utilization of observational overlaps to thoroughly analyze EBs and SEBs through the extraction of stellar and orbital parameters. The combination of stellar and orbital parameters from highly accessible SEBs yields increased precision in orbital solutions, but also the extraction of secondary stellar parameters in certain cases. In the specific instance of SEB II systems the Broadening Function method of RV extraction is preferred in solving for primary and secondary RV components. A general discussion of Clark Cunningham et al. (2019) - which studied SEBs in the *APOGEE/Kepler* overlap follows in ???. This is followed by the study of young eclipsing binary tertiary system, HD 54236 4 which utilized spectroscopy and photometry from a number of missions. Then, a description of the EBs in the *APOGEE Gold Sample/TESS* overlap can be found in 5.

Outlined in 3 is the thorough characterization of seven SEBs within the *APOGEE/Kepler* overlap from Clark Cunningham et al. (2019). These targets were first selected by limiting targets within the *Kepler* EB catalog to those with both primary and secondary eclipsing events, high inclination and multiple  $\text{ApVisit}$  spectra. In each of these targets, the BF method of RV extraction was completed and RV components for both primary and secondary stellar components were found. In each case, the superiority of the BF RV extraction compared to the CCF RV extraction currently used in the reduction pipeline.

The radial velocity components for each system were extracted from  $\text{ApVisit}$  spectra. *Kepler* light curves are normalized, de-weighted and modeled using *KEBLAT* (Windemuth et al., 2018) both photometric and spectroscopic solutions are arrived at individually, and then computed simultaneously for greater constraint. The resulting stellar parameters were then used in the estimation of the effective temperature (for primary and secondary stars) and to arrive at an age estimate for each system. These age estimates for the stars in each binary serve as a coevality tests for each system. The systems in 3 (Clark Cunningham et al., 2019) are all broadly consistent with coevality - affirming the assumption that star formation in multiplicity systems occurs at roughly the same time.

The *APOGEE/Kepler* overlap also empowered the discovery of higher order systems, Clark



Cunningham et al. (2019) identified three candidate triple systems: KIC 6131659, KIC 6781535, and KIC 6449358. Both KIC 6131659 and KIC 6781535 had clear third BF component peaks in nearly all of their  $ApVisit$  spectra. These third peaks were fitted with Gaussians as were the primary and secondary BF peaks, and in both targets, these third BF components do not have variations in their RV estimates above the noise. The stationary nature of these third BF peaks indicates that these third members are either line-of-sight contamination or indeed, gravitationally bound in hierarchical triples with periods much greater than those reported for the SEB target. KIC 6449358 has spectroscopic and photometric evidence of a third member being present, a third BF component is visible in a few of its  $ApVisit$  spectra and the mid times of eclipses in the *Kepler* LC exhibits sinusoidal variations in time. The ETVs in the *Kepler* LC indicate that the tertiary star has a period of  $\gtrsim 1450$  days.

The analysis completed using the *APOGEE/Kepler* overlap found that our binary subset are all roughly coeval with ages ranging from 1 to 3 Gyr, assuming a normal Milky Way metallicity ( $-0.5 < [M/H] < 0$ ). KIC 6781535 being an exception as it lies closer to a slightly metal poor ( $[M/H] \sim -1.0$ ) isochrone of 3 Gyr. The *APOGEE/Kepler* subset of SEBs being broadly consistent with coevality calibrates stellar evolution modeling by confirming the assumption that members of binary and higher order systems form at the same time.

Utilizing the observational overlap between large scale surveys like *APOGEE* and *Kepler* with tools like the Broadening Function method of RV extraction, and *KEBLAT* simultaneous LC RV modeling it is possible to thoroughly analyze SEB IIs with high-quality, well constrained results over a wide range of properties.

In 4, HD 54236, a young, wide, common-proper motion visual pair is discovered to contain an EB comprising of two solar mass stars in a 2.4 day orbit. HD 54236 had been previously identified as a PMS star because of its strong X-ray emission and lithium absorption (Clark Cunningham et al., 2020). Its primary (HD 54236A) being an unresolved EB, HD 54236B being a wide common proper motion tertiary companion, and the systems youthful age estimate represented a critical opportunity to expand the number of benchmark-grade EBs at young stellar ages. Spectroscopic observations of the HD 54236 system from the Wide Field Spectrograph (WiFeS), echelle spectrograph on the ANU 2.3-m telescope from the Australian National University<sup>1</sup>, and, the Goodman High Throughput Spectrograph (Clemens et al., 2004), installed on the f/16.6 Nasmyth platform of the 4.1 m Southern Astrophysical Research (SOAR) telescope. For further information on these instruments and the analysis of their spectroscopic observations, see 3.

Photometric observations for the HD 54236 system were attained from three sources: TESS, PEST, and the Kilodegree Extremely Little Telescope-South (*KELT* South). The modeling of these observations and the details of their analysis are found in 4.3. *PHoEBE* was used to fit these

---

<sup>1</sup><http://rsaa.anu.edu.au/observatories/siding-spring-observatory>

data-sets and solve for orbital and stellar solutions of the EB.

Two common stellar chronometers: Li abundance and the strength of chromospheric activity in the Ca II H&K lines are deployed to estimate an age for the HD 54236 system. Due to the short orbital period of the eclipsing pair in HD 54236A, and it's likely enhanced rotation, the tertiary HD 54236B is utilized to get a clean estimate of the Ca II H&K activity age for the system. The Ca II H&K spectral features of HD 54236B were compared against the spectral features of three different open clusters spanning the range of age estimates from the Li abundance chronometer at similar effective temperatures. All three stellar components were modeled in the effective temperature radius plane of the HR diagram and compared to the Yonsei-Yale stellar evolutionary tracks (Yi et al., 2001) and to the PMS evolutionary models of Baraffe et al. (1998) for the spectroscopically determined  $[Fe/H]$  of  $-0.5$ . All of these chronometers suggested an age for the system near the ZAMS or slightly younger (Clark Cunningham et al., 2019). Auxiliary age estimates for the wide tertiary member HD 54236B were acquired using photometry and `MINESweeper` which uses a Bayesian approach to estimate stellar parameters from MIST stellar evolutionary models (Choi et al., 2016). With photometry for HD 54236B from *Gaia* DR2, 2MASS, and UNWISE, `MINESweeper` yielded an age estimate of  $149_{-77}^{+173}$ -Myr for the tertiary, in agreement with the other age estimates outlined above. Having less mass than its EB companion, and having a wide separation makes HD 54236B's position in HR diagram space more sensitive to the system's age estimate. See 4.3.5.4 for figures and further discussion from Clark Cunningham et al. (2020).

At the time of this work (Clark Cunningham et al., 2020), the HD 54236 system did not have any established membership to a stellar population. However, a cross-match against newly discovered moving group candidate populations from the Kounkel & Covey (2019); Kounkel et al. (2020) catalog, established a most likely progenitor Theia-301. Interestingly, in this work a possible ancestral link between the Ab Dor moving group and Theia 301 is identified by virtue of six mutual stellar members serving as a bridge between the two populations. Additionally, Theia 301 and AB Dor have independent age estimates of roughly the same ages. Through isochrone fitting of the population, Theia 301 is estimated to have an age of 134–280 Myr. The age of AB Dor moving group is estimated at 130–200 Myr (Bell et al., 2015). These independent age estimates are consistent with the age of HD 54236 derived through Li I and Ca II H&K abundances.

5 explores the overlap between the *APOGEE Gold Sample* and *TESS* photometry. This sub-sample includes three systems whose geometry was conducive to the BF modeling, but in all cases of the *TESS* photometric evaluation of *APOGEE* identified binary systems, increased precision in period estimates was possible. Additionally, the establishment of **[ALL THING YOU CAN SOLVE FOR WITH PHOEBE]** estimates, which have not been previously estimated. Additionally, for all systems within our overlap, age estimates are more refined with disentangled primary and secondary stellar parameters from the *TESS* photometry alone.

Eclipsing binaries represent critical sites for the direct measurement of stellar and orbital parameters. Especially in the cases where spectroscopic observations are also available, SEBs whose solutions can be even better constrained. Extracted stellar and orbital parameters function as tests of stellar evolutionary theory. The methodology applicable to each system varies depending on factors like inclination: systems with inclinations  $\sim 90^\circ$  are more likely to have primary and secondary eclipsing events in their photometric observations. In binary systems with a mass ratio far from unity, the less luminous, smaller secondary is less likely to have an appreciable presence in spectroscopic observations. Similarly, if a secondary spectroscopic signature is present, it can be difficult to disentangle from an overbearing primary spectral signature. As discussed in 3 and 5, only SEB II systems are approachable with the BF RV extraction methodology. Therefore, as in 4 with HD 54236A, the CCF method of RV extraction is most applicable.

As was shown in 3 (Clark Cunningham et al., 2019), extracted parameters from the *APOGEE/Kepler* SEBs which were plotted in HR-diagram space with stellar evolutionary tracks. This serves to not only validate stellar evolution theory, but also to confirm the coevality assumption, as members of each binary system had effectively the same age as their companion. Age estimates of the young EB tertiary system HD 54236 (4.3.5.4) were instrumental in establishing the connection to the stellar stream of its ancestry: Theia 301.

EBs and SEBs embody Astrophysical laboratories where we can measure the fundamental properties of stars to an increasing amount of certainty *and* accessibility. As missions like *APOGEE* and *TESS* produce new data releases, and finer analysis tools are developed the number of well constrained, benchmark-grade EBs and SEBs will increase. Additional stellar evolution calibrations and tests can be completed over an increasingly diverse population. The establishment of membership to stellar streams and associations (as was the case in 4) lends insight to star systems origin through the identification of progenitors. This in turn infers how the migration of stellar streams and association through the galaxy occurs, which is a foundational part of galactic evolution.

Beyond the intricacy of their orbits, formation, and evolution, every binary star, every multiplicity system that is confirmed - helps to refine the binary fraction. The IMF is not normally corrected for the effect that many, if not most stars reside in (unresolved) binary systems (Malkov & Zinnecker, 2001). Further, Kroupa & Jerabkova (2018) found that the effect on the IMF is not uniform across stellar masses; at the high mass end of binary mass ratios, the shape of the IMF is not much effected by unresolved binary companions. At the lower mass end of binary ratios, the IMF does appear to be effected by unresolved binary companions.

Every binary star system from which we are able to extract stellar and orbital parameters in another point of knowledge in astrophysical evolution: from the large scale of galaxies, down the the smallest scales of stars and planets.

## **Acknowledgements**

I, Joni Marie Clark Cunningham (J = MC<sup>2</sup>) would like to firstly extend my profound gratitude to David Weintraub as my primary advisor and chair. I would also like to thank the remainder of my committee, Kelly Holly-Bockelmann, Stephen Taylor, Eric Agol, and Joshua Pepper. My dearest gratitude is given to the Fisk-Vanderbilt Masters to PhD bridge program, and to Keivan Stassun.

I would also like to extend my thanks to Meredith Rawls, Adrian Price-Whelan, Paul Mason, and Nick Troupe for their helpful advice and recommendations during various stages of these projects. Dina Stroud, Lauren Campbell, and Alyce Dobbins are appreciated for their guidance and helpful insight in my first generation navigation of graduate school.

The mentors that guided me through the chaos of graduate school during a global health crisis with a young son: Kelly Holley-Bockelmann, Stephen Taylor, Lauren Campbell, Dina Stroud, Keivan Stassun, and to the countless friends I've made through the experience, I am so very grateful for your presence.

My family deserves the utmost celebration in their continued support and encouragement. My son Victor who joined me in Nashville for the first two years of his life, and encouraged and motivated me before he could speak, and before I myself could believe in my own capacity. To my dearest mom, Sherrie Clark, and my husband Michael Cunningham who continued to care for my son as I completed this dissertation. Thanks go as well to Nancy Floyd and her son Matthew for keeping a roof over my head, cheering me on, and being sure I remembered to eat while I was completing the final stages of my lifelong dream.

# Bibliography

- Aarnio, A.-N., Weinberger, A.-J., Stassun, K.-G., Mamajek, E.-E., & James, D.-J. 2008, *AJ*, 136:6, 2483 , doi: 10.1088/0004-6256/136/6/2483
- Alard, C. 2000, *Astronomy and Astrophysics Supplement*, 144, 363 , doi: 10.1051/aas:2000214
- Alard, C., & Lupton, R.-H. 1998, *ApJ*, 503:1, 325 , doi: 10.1086/305984
- Anderson, L., & Shu, F. H. 1979, *ApJS*, 40, 667, doi: 10.1086/190601
- Bailer-Jones, C. A. L., Rybizki, J., Fouesneau, M., Mantelet, G., & Andrae, R. 2018, *AJ*, 156, 58, doi: 10.3847/1538-3881/aacb21
- Baraffe, I., Chabrier, G., Allard, F., & Hauschildt, P. H. 1998, *A&A*, 337, 403. <https://arxiv.org/abs/astro-ph/9805009>
- Barclay, T., Pepper, J., & Quintana, E. V. 2018, 239, 2, doi: 10.3847/1538-4365/aae3e9
- Barenfeld, S.-A., Bubar, E.-J., Mamajek, E.-E., & Young, P.-A. 2013, *ApJ*, 766:6, 7, doi: 10.1088/0004-637X/766/1/6
- Bate, M. R. 2009, *MNRAS*, 392, 590, doi: 10.1111/j.1365-2966.2008.14106.x
- Bayless, A. J., & Orosz, J. A. 2006, *The Astrophysical Journal*, 651, 1155, doi: 10.1086/507981
- Bayliss, D., Zhou, G., Penev, K., et al. 2013, *AJ*, 146:113, 11, doi: 10.1088/0004-6256/146/5/113
- Beatty, T.-G., Pepper, J., Siverd, R.-J., et al. 2012, *The Astrophysical Journal Letters*, 756:L39, 6, doi: 10.1088/2041-8205/756/2/L39
- Bell, C.-P.-M., Mamajek, E.-E., & Naylor, T. 2015, *MNRAS*, 454, 593 , doi: 10.1093/mnras/stv1981
- Bertin, E., & Arnouts, S. 1996, *Astronomy and Astrophysics Supplemental Series*, 117, 393 , doi: 10.1051/aas:1996164
- Bessell, M.-S. 1999, *Publications of the Astronomical Society of the Pacific*, 111:765, 1426, doi: 10.1086/316454

- Borkovits, T., Hajdu, T., Sztakovics, J., et al. 2016, MNRAS, 455, 4136, doi: 10.1093/mnras/stv2530
- Borucki, W. J., Koch, D., Basri, G., et al. 2010, Science, 327, 977
- Bovy, J. 2016, The Astrophysical Journal, 817, 49, doi: 10.3847/0004-637x/817/1/49
- Cargile, P., Stassun, K. G., & Mathieu, R. 2006, A Spectroscopic Study of A Newly Discovered Pre-Main-Sequence Eclipsing Binary Star System in Orion, NOAO Proposal
- Cargile, P. A., Conroy, C., Johnson, B. D., et al. 2019, arXiv e-prints, arXiv:1907.07690. <https://arxiv.org/abs/1907.07690>
- Carlsson, M., & Stein, R.-F. 1994, ApJ, 440:L29, 4, doi: 10.1086/187753
- Casali, G., Spina, L., Magrini, L., et al. 2020, A&A, 639, A127, doi: 10.1051/0004-6361/202038055
- Chakraborty, A., & Feigelson, E.-D. 1995, Astronomy Users Library: Package astrolibR
- Chambers, J. E. 2010, ApJ, 724, 92, doi: 10.1088/0004-637X/724/1/92
- Choi, J., Dotter, A., Conroy, C., et al. 2016, ApJ, 823, 102, doi: 10.3847/0004-637X/823/2/102
- Clark Cunningham, J.-M., Pepper, J., & Weintraub, D. 2022
- Clark Cunningham, J. M., Rawls, M. L., Windemuth, D., et al. 2019, AJ, 158, 106, doi: 10.3847/1538-3881/ab2d2b
- Clark Cunningham, J.-M., Felix, D. L., Dixon, D. M., et al. 2020, arXiv e-prints, arXiv:2009.03872. <https://arxiv.org/abs/2009.03872>
- Clemens, C.-J., Crain, A. J., & Anderson, R. 2004, Ground-based instrumentation for Astronomy, Proceedings, 5492, doi: 10.1117/12.550069
- Close, L. M., Lenzen, R., Guirado, J. C., et al. 2005, Nature, 433, 286, doi: 10.1038/nature03225
- Cohen, M., Wheaton, W. A., & Megeath, S. T. 2003, AJ, 126, 1090, doi: 10.1086/376474
- Collins, K. A., Eastman, J. D., Beatty, T. G., et al. 2014, AJ, 142:2, 18, doi: 10.1088/0004-6256/147/2/39
- Conroy, K. E., Prša, A., Stassun, K. G., et al. 2014, AJ, 147, 45, doi: 10.1088/0004-6256/147/2/45
- Dantona, F., & Mazzitelli, I. 1984, A&A, 138, 431
- Dopita, M., Hart, J., McGregor, P., et al. 2007, Ap&SS, 310, 255, doi: 10.1007/s10509-007-9510-z

- Dotter, A. 2016, *ApJS*, 222, 8, doi: 10.3847/0067-0049/222/1/8
- Dotter, A., Chaboyer, B., Jevremović, D., et al. 2008, *ApJS*, 178, 89, doi: 10.1086/589654
- Duchêne, G., & Kraus, A. 2013, *ARA&A*, 51, 269, doi: 10.1146/annurev-astro-081710-102602
- Dunham, M. M., & Vorobyov, E. I. 2012, *ApJ*, 747, 52, doi: 10.1088/0004-637X/747/1/52
- El-Badry, K., Rix, H.-W., Ting, Y.-S., et al. 2017, *MNRAS*, 473, 5043, doi: 10.1093/mnras/stx2758
- Evans, N. R. 2011, *Bulletin de la Societe Royale des Sciences de Liege*, 80, 663. <https://arxiv.org/abs/1102.5316>
- Federrath, C., Sur, S., Schleicher, D. R. G., Banerjee, R., & Klessen, R. S. 2011, *ApJ*, 731, 62, doi: 10.1088/0004-637X/731/1/62
- Feroz, F., Hobson, M. P., Cameron, E., & Pettitt, A. N. 2019, *The Open Journal of Astrophysics*, 2, 10, doi: 10.21105/astro.1306.2144
- Fleming, S. W., Mahadevan, S., Deshpande, R., et al. 2015, *The Astronomical Journal*, 149, 143, doi: 10.1088/0004-6256/149/4/143
- Foreman-Mackey, D., Hogg, D. W., Lang, D., & Goodman, J. 2013, *PASP*, 125, 306, doi: 10.1086/670067
- Gagné, J., Faherty, J. K., & Popinchalk, M. 2020, *Research Notes of the American Astronomical Society*, 4, 92, doi: 10.3847/2515-5172/ab9e79
- Gagné, J., Mamajek, E. E., Malo, L., et al. 2018, *ApJ*, 856, 23, doi: 10.3847/1538-4357/aaae09
- Gaia Collaboration, Brown, A. G. A., Vallenari, A., et al. 2018, *A&A*, 616, A1, doi: 10.1051/0004-6361/201833051
- Gaulme, P., McKeever, J., Jackiewicz, J., et al. 2016, *The Astrophysical Journal*, 832, 121, doi: 10.3847/0004-637x/832/2/121
- Gómez Maqueo Chew, Y., Stassun, K. G., Vaz, L. P., Mathieu, R., & Valenti, J. 2006, in *Revista Mexicana de Astronomia y Astrofisica Conference Series*, Vol. 26, *Revista Mexicana de Astronomia y Astrofisica Conference Series*, 170
- Guillot, T., Ida, S., & Ormel, C. W. 2014, *A&A*, 572, A72, doi: 10.1051/0004-6361/201323021
- Hamuy, M., Suntzeff, N. B., Heathcote, S. R., et al. 1994, *PASP*, 106, 566, doi: 10.1086/133417

- Hartman, J. D., & Bakos, G. Á. 2016, *Astronomy and Computing*, 17, 1, doi: 10.1016/j.ascom.2016.05.006
- Hartmann, D. H., Grindlay, J., Band, D., et al. 2004, *NewAR*, 48, 237, doi: 10.1016/j.newar.2003.11.055
- Hartmann, L., Cassen, P., & Kenyon, S. J. 1997, *ApJ*, 475, 770, doi: 10.1086/303547
- Hayashi, C. 1961, *PASJ*, 13, 450
- Hillenbrand, L. A. 2009, 258, 81, doi: 10.1017/S1743921309031731
- Hills, S., von Hippel, T., Courteau, S., & Geller, A. M. 2015, *AJ*, 149, 94, doi: 10.1088/0004-6256/149/3/94
- Hipke, M., David, T. J., Mulders, G. D., & Heller, R. 2019, *AJ*, 158, 143, doi: 10.3847/1538-3881/ab3984
- Holtzman, J. A., Shetrone, M., Johnson, J. A., et al. 2015, *AJ*, 150, 148, doi: 10.1088/0004-6256/150/5/148
- Huang, C. X., Vanderburg, A., Pál, A., et al. 2020a, *Research Notes of the American Astronomical Society*, 4, 204, doi: 10.3847/2515-5172/abca2e
- . 2020b, *Research Notes of the American Astronomical Society*, 4, 204, doi: 10.3847/2515-5172/abca2e
- Husser, T.-O., von Berg, S. W., Dreizler, S., et al. 2013, *Astronomy & Astrophysics*, 553, A6, doi: 10.1051/0004-6361/201219058
- Jeans, J. H. 1929, *MNRAS*, 85, 394, doi: 10.1093/mnras/85.5.394
- Jenkins, J. M., Caldwell, D. A., Chandrasekaran, H., et al. 2010, *ApJL*, 713, L87, doi: 10.1088/2041-8205/713/2/L87
- Jenkins, J. M., Twicken, J. D., McCauliff, S., et al. 2016, in *Society of Photo-Optical Instrumentation Engineers (SPIE) Conference Series*, Vol. 9913, *Software and Cyberinfrastructure for Astronomy IV*, ed. G. Chiozzi & J. C. Guzman, 99133E, doi: 10.1117/12.2233418
- Johnson, D. R. H., & Soderblom, D. R. 1987, *AJ*, 93, 864, doi: 10.1086/114370
- Jørgensen, B. R., & Lindegren, L. 2005, *A&A*, 436, 127, doi: 10.1051/0004-6361:20042185
- Kipping, D. M. 2010, *Monthly Notices of the Royal Astronomical Society*, 408, 1758, doi: 10.1111/j.1365-2966.2010.17242.x
- Kipping, D. M. 2013, *Astronomy and Astrophysics*, 154, 216, doi: 10.3847/1538-3881/aa8fd6
- Kirk, B., Conroy, K., Prsa, A., et al. 2016, *The Astronomical Journal*, 151, 68



- Kounkel, M., & Covey, K. 2019, *AJ*, 158, 122, doi: 10.3847/1538-3881/ab339a
- Kounkel, M., Covey, K., & G., S. K. 2020, arXiv e-prints. <https://arxiv.org/abs/2004.07261>
- Kozai, Y. 1962, *The Astronomical Journal*, 67, 591
- Kroupa, P., & Jerabkova, T. 2018, arXiv e-prints, arXiv:1806.10605. <https://arxiv.org/abs/1806.10605>
- Kuiper, G. P. 1935, *Publications of the Astronomical Society of the Pacific*, 47, 121. <http://www.jstor.org/stable/40669334>
- Kunimoto, M., Huang, C., Tey, E., et al. 2021, *Research Notes of the American Astronomical Society*, 5, 234, doi: 10.3847/2515-5172/ac2ef0
- Kunitomo, M., Guillot, T., Takeuchi, T., & Ida, S. 2017, *A&A*, 599, A49, doi: 10.1051/0004-6361/201628260
- Lachaume, R., Dominik, C., Lanz, T., & Habing, H. J. 1999, *A&A*, 348, 897
- Larson, R. B. 1969, *MNRAS*, 145, 271, doi: 10.1093/mnras/145.3.271
- . 1972, *MNRAS*, 156, 437, doi: 10.1093/mnras/156.4.437
- . 1973, *MNRAS*, 161, 133, doi: 10.1093/mnras/161.2.133
- . 2003, *Reports on Progress in Physics*, 66, 1651, doi: 10.1088/0034-4885/66/10/R03
- Lehmann, H., Zechmeister, M., Dreizler, S., Schuh, S., & Kanzler, R. 2012, *Astronomy and Astrophysics*, 541, A105
- Lightkurve Collaboration, Cardoso, J. V. d. M., Hedges, C., et al. 2018, *Lightkurve: Kepler and TESS time series analysis in Python*, *Astrophysics Source Code Library*. <http://ascl.net/1812.013>
- Lu, W., Rucinski, S. M., & OgŁoza, W. 2001, *The Astronomical Journal*, 122, 402, doi: 10.1086/321131
- Luhman, K.-L., Stauffer, J.-R., & Mamajek, E.-E. 2005, *ApJ*, 628, L69, doi: 10.1086/432617
- MacDonald, J., & Mullan, D. J. 2017, *ApJ*, 834, 67, doi: 10.3847/1538-4357/834/1/67
- Machida, M. N., ichiro Inutsuka, S., & Matsumoto, T. 2007, *The Astrophysical Journal*, 670, 1198, doi: 10.1086/521779
- Machida, M. N., Tomisaka, K., & Matsumoto, T. 2004, *MNRAS*, 348, L1, doi: 10.1111/j.1365-2966.2004.07402.x
- Machida, M. N., Tomisaka, K., Matsumoto, T., & Inutsuka, S.-i. 2008, *ApJ*, 677, 327, doi: 10.1086/529133

- Majewski, S. R., Schiavon, R. P., Frinchaboy, P. M., et al. 2015, arXiv.org
- Majewski, S. R., Schiavon, R. P., Frinchaboy, P. M., et al. 2017, *AJ*, 154, 94, doi: 10.3847/1538-3881/aa784d
- Malkov, O., & Zinnecker, H. 2001, *MNRAS*, 149, doi: 10.1046/j.1365-8711.2001.04015.x
- Mamajek, E. E. 2008, *Astronomische Nachrichten*, 329, 10, doi: 10.1002/asna.200710827
- Mandel, K., & Agol, E. 2002, *The Astrophysical Journal*, 580, L171, doi: 10.1086/345520
- Marois, C., Macintosh, B., Song, I., & Barman, T. 2005, arXiv e-prints, astro. <https://arxiv.org/abs/astro-ph/0502382>
- Mason, B. D., Wycoff, G. L., Hartkopf, W. I., Douglass, G. G., & Worley, C. E. 2001, *AJ*, 122, 3466, doi: 10.1086/323920
- Matson, R. A., Gies, D. R., Guo, Z., & Williams, S. J. 2017, *The Astronomical Journal*, 154, 216
- Mengel, J. G., Sweigart, A. V., Demarque, P., & Gross, P. G. 1979, *ApJS*, 40, 733, doi: 10.1086/190603
- Mercer-Smith, J. A., Cameron, A. G. W., & Epstein, R. I. 1984, *ApJ*, 279, 363, doi: 10.1086/161897
- Messina, S., Desidera, S., Turatto, M., Lanzafame, A. C., & Guinan, E. F. 2010, *A&A*, 520, A15, doi: 10.1051/0004-6361/200913644
- Metcalf, T. S. 1999, *AJ*, 117, 2503, doi: 10.1086/300833
- Moe, M., & Di Stefano, R. 2017, *ApJS*, 230, 15, doi: 10.3847/1538-4365/aa6fb6
- Morton, T. D., Bryson, S. T., Coughlin, J. L., et al. 2016, *ApJ*, 822, 86, doi: 10.3847/0004-637X/822/2/86
- Munari, U., Sordo, R., Castelli, F., & Zwitter, T. 2005, *A&A*, 442, 1127, doi: 10.1051/0004-6361:20042490
- Nelson, L. A., Rappaport, S., & Chiang, E. 1993, *ApJ*, 413, 364, doi: 10.1086/173004
- Newville, M., Stensitzki, T., Allen, D. B., et al. 2016, *Astrophysics Source Code Library*, ascl:1606.014
- Nidever, D. L., Holtzman, J. A., Prieto, C. A., et al. 2015, *The Astronomical Journal*, 150, 173, doi: 10.1088/0004-6256/150/6/173
- Oelkers, R. J., & Stassun, K. G. 2018, *AJ*, 156, 132, doi: 10.3847/1538-3881/aad68e
- Oh, S., Price-Whelan, A.-M., Hogg, D.-W., Morton, T.-D., & Spergel, D.-N. 2017, *AJ*, 153, 257, doi: 10.3847/1538-3881/aa6ffd

- Palla, F., & Stahler, S. W. 1992, *ApJ*, 392, 667, doi: 10.1086/171468
- Penev, K., Bakos, G. Á., Bayliss, D., et al. 2013, *AJ*, 145, 5. <https://arxiv.org/abs/1206.1524>
- Pepper, J., Kuhn, R. B., Siverd, R., James, D., & Stassun, K. 2012, *PASP*, 124, 230, doi: 10.1086/665044
- Pepper, J., Stanek, K. Z., Pogge, R. W., et al. 2008, *AJ*, 135, 907, doi: 10.1088/0004-6256/135/3/907
- Pepper, J., Pogge, R. W., DePoy, D. L., et al. 2007, *PASP*, 119, 923, doi: 10.1086/521836
- Pérez, A. E. G., Prieto, C. A., Holtzman, J. A., et al. 2016, *The Astronomical Journal*, 151, 144, doi: 10.3847/0004-6256/151/6/144
- Pinsonneault, M. H., Elsworth, Y., Epstein, C., et al. 2014, *ApJS*, 215, 19, doi: 10.1088/0067-0049/215/2/19
- Pinsonneault, M. H., Elsworth, Y. P., Tayar, J., et al. 2018, *ArXiv e-prints*, arXiv:1804.09983. <https://arxiv.org/abs/1804.09983>
- Price-Whelan, A. M., & Goodman, J. 2018, *The Astrophysical Journal*, 867, 5, doi: 10.3847/1538-4357/aae264
- Price-Whelan, A. M., Hogg, D. W., Foreman-Mackey, D., & Rix, H.-W. 2017, *ApJ*, 837, 20, doi: 10.3847/1538-4357/aa5e50
- Price-Whelan, A. M., Hogg, D. W., Rix, H.-W., et al. 2020, *ApJ*, 895, 2, doi: 10.3847/1538-4357/ab8acc
- Prsa, A., Matijevic, G., Latkovic, O., Vilardell, F., & Wils, P. 2011, *PHOEBE: PHysics Of Eclipsing BinariEs*. <http://ascl.net/1106.002>
- Prša, A., Batalha, N., Slawson, R. W., et al. 2011, *AJ*, 141, 83, doi: 10.1088/0004-6256/141/3/83
- Prša, A., Conroy, K. E., Horvat, M., et al. 2016, *ApJS*, 227, 29, doi: 10.3847/1538-4365/227/2/29
- Prša, A., Kochoska, A., Conroy, K. E., et al. 2022, *ApJS*, 258, 16, doi: 10.3847/1538-4365/ac324a
- Queiroz, A. B. A., Anders, F., Chiappini, C., et al. 2020, *A&A*, 638, A76, doi: 10.1051/0004-6361/201937364
- Ramírez, I., Meléndez, J., & Asplund, M. 2009, *A&A*, 508, L17, doi: 10.1051/0004-6361/200913038
- Ramírez, I., Meléndez, J., Cornejo, D., Roederer, I. U., & Fish, J. R. 2011, *ApJ*, 740, 76, doi: 10.1088/0004-637X/740/2/76

- Rappaport, S., Deck, K., Levine, A., et al. 2013, *ApJ*, 768, 33, doi: 10.1088/0004-637X/768/1/33
- Rawls, M. L., Gaulme, P., McKeever, J., et al. 2016, *The Astrophysical Journal*, 818, 108, doi: 10.3847/0004-637x/818/2/108
- Reipurth, B., Clarke, C. J., Boss, A. P., et al. 2014, in *Protostars and Planets VI*, ed. H. Beuther, R. S. Klessen, C. P. Dullemond, & T. Henning, 267, doi: 10.2458/azu\_uapress\_9780816531240-ch012
- Ricker, G. R., Winn, J. N., Vanderspek, R., et al. 2015, *Journal of Astronomical Telescopes, Instruments, and Systems*, 1, 014003, doi: 10.1117/1.JATIS.1.1.014003
- Rucinski, S. M. 1992, *The Astronomical Journal*, 104, 1968, doi: 10.1086/116372
- . 1999, *International Astronomical Union Colloquium*, 170, 82, doi: 10.1017/s0252921100048405
- . 2002, *The Astronomical Journal*, 124, 1746, doi: 10.1086/342342
- Rucinski, S. M. 2003, *Stellar Rotation, Proceedings of IAU Symposium No. 215*
- Rucinski, S. M. 2004, in *Stellar Rotation*, ed. A. Maeder & P. Eenens, Vol. 215, 17
- Rucinski, S. M., Lu, W. X., & Shi, J. 1993, *AJ*, 106, 1174, doi: 10.1086/116716
- Sestito, P., & Randich, S. 2005, *A&A*, 442, 615, doi: 10.1051/0004-6361:20053482
- Siess, L., Forestini, M., & Bertout, C. 1997, *A&A*, 326, 1001
- Sipocz, B., Robitaille, T., & Tollerud, E. 2016, in *Python in Astronomy 2016*, ed. T. Jenness, T. Robitaille, E. Tollerud, S. Mumford, & K. Cruz, 2, doi: 10.5281/zenodo.56799
- Sivard, R. J., Beatty, T. G., Pepper, J., et al. 2012, *ApJ*, 761, 123, doi: 10.1088/0004-637X/761/2/123
- Skrutskie, M. F., Cutri, R. M., Stiening, R., et al. 2006, *AJ*, 131, 1163, doi: 10.1086/498708
- Soderblom, D. R., Jones, B. F., Balachandran, S., et al. 1993, *AJ*, 106, 1059, doi: 10.1086/116704
- Soderblom, D. R., King, J. R., Siess, L., Jones, B. F., & Fischer, D. 1999, *AJ*, 118, 1301, doi: 10.1086/301016
- Stahler, S. W., Shu, F. H., & Taam, R. E. 1980, *ApJ*, 241, 637, doi: 10.1086/158377
- Stanway, E. R., Chrimes, A. A., Eldridge, J. J., & Stevance, H. F. 2020, *MNRAS*, 495, 4605, doi: 10.1093/mnras/staa1166
- Stassun, K. 2011, 11

- Stassun, K. G., Collins, K. A., & Gaudi, B. S. 2017, *AJ*, 153, 136, doi: 10.3847/1538-3881/aa5df3
- Stassun, K. G., Feiden, G. A., & Torres, G. 2014, *NewAR*, 60, 1, doi: 10.1016/j.newar.2014.06.001
- Stassun, K. G., Mathieu, R. D., & Valenti, J. A. 2007, *The Astrophysical Journal*, 664, 1154, doi: 10.1086/519231
- Stassun, K. G., Mathieu, R. D., Vaz, L. P. R., Stroud, N., & Vrba, F. J. 2004, *ApJS*, 151, 357, doi: 10.1086/382353
- Stassun, K. G., Oelkers, R. J., Pepper, J., et al. 2018, *AJ*, 156, 102, doi: 10.3847/1538-3881/aad050
- Stassun, K. G., Oelkers, R. J., Paegert, M., et al. 2019, *AJ*, 158, 138, doi: 10.3847/1538-3881/ab3467
- Stauffer, J., Barrado, D., David, T., et al. 2020, *AJ*, 160, 30, doi: 10.3847/1538-3881/ab93c9
- Stetson, P. B. 1987, *PASP*, 99, 191, doi: 10.1086/131977
- . 1990, *PASP*, 102, 932, doi: 10.1086/132719
- Sullivan, P. W., Winn, J. N., Berta-Thompson, Z. K., et al. 2015, *ApJ*, 809, 77, doi: 10.1088/0004-637X/809/1/77
- Teske, J. K., Ciardi, D. R., Howell, S. B., Hirsch, L. A., & Johnson, R. A. 2018, *AJ*, 156, 292, doi: 10.3847/1538-3881/aaed2d
- Thompson, S. E., Everett, M., Mullally, F., et al. 2012, *ApJ*, 753, 86, doi: 10.1088/0004-637X/753/1/86
- Tokovinin, A. 2008, *MNRAS*, 389, 925, doi: 10.1111/j.1365-2966.2008.13613.x
- . 2014, *AJ*, 147, 86, doi: 10.1088/0004-6256/147/4/86
- Tokovinin, A., Thomas, S., Sterzik, M., & Udry, S. 2006, *A&A*, 450, 681, doi: 10.1051/0004-6361:20054427
- Tokovinin, A. A. 1997, *Astronomy Letters*, 23, 727
- Tomisaka, K. 1998, *ApJL*, 502, L163, doi: 10.1086/311504
- Toonen, S., Hamers, A., & Portegies Zwart, S. 2016, *Computational Astrophysics and Cosmology*, 3, 6, doi: 10.1186/s40668-016-0019-0
- Torres, C. A. O., Quast, G. R., da Silva, L., et al. 2006, *A&A*, 460, 695, doi: 10.1051/0004-6361:20065602

- Torres, G., Clausen, J. V., Bruntt, H., et al. 2012, *A&A*, 537, A117, doi: 10.1051/0004-6361/201117795
- Torres, G., Curtis, J. L., Vanderburg, A., Kraus, A. L., & Rizzuto, A. 2018, arXiv.org, arXiv:1808.07482
- Torres, G., Lacy, C. H. S., Pavlovski, K., et al. 2015, in *Astronomical Society of the Pacific Conference Series*, Vol. 496, *Living Together: Planets, Host Stars and Binaries*, ed. S. M. Rucinski, G. Torres, & M. Zejda, 169. <https://arxiv.org/abs/1503.06310>
- Troup, N. W., Nidever, D. L., De Lee, N., et al. 2016, *AJ*, 151, 85, doi: 10.3847/0004-6256/151/3/85
- Valls-Gabaud, D. 2014, in *EAS Publications Series*, Vol. 65, *EAS Publications Series*, 225–265, doi: 10.1051/eas/1465006
- Wilson, R. E., & Devinney, E. J. 1971, *ApJ*, 166, 605, doi: 10.1086/150986
- Windemuth, D., Agol, E., Ali, A., & Kiefer, F. 2018, *MNRAS*
- Wright, N.-J., Drake, J.-J., Mamajek, E.-E., & Henry, G.-W. 2011, *ApJ*, 743, 48, doi: 10.1088/0004-637x/743/1/48
- Yi, S., Demarque, P., Kim, Y.-C., et al. 2001, *ApJS*, 136, 417, doi: 10.1086/321795
- Zamora, O., García-Hernández, D. A., Allende Prieto, C., et al. 2015, *AJ*, 149, 181, doi: 10.1088/0004-6256/149/6/181
- Zhou, G., Bayliss, D., Penev, K., et al. 2014, *AJ*, 147, 144, doi: 10.1088/0004-6256/147/6/144